

CMS Draft Analysis Note

The content of this note is intended for CMS internal use and distribution only

2013/08/23

Head Id: 200735

Archive Id: 203869

Archive Date: 2013/08/05

Archive Tag: trunk

Search for a BSM resonance decaying to Z vector bosons in the semileptonic final state

C. Bernardes⁵, A. Bonato¹, A. Hinzmann¹, Q. Li³, S. Liu³, M. Mozer², P. Mercadante⁵, S. Novaes⁴, M. Pierini¹, F. Santanastasio¹, A. Spiezia⁶, and T. Tomei⁴

¹ CERN

² KIT

³ Peking National University

⁴ SPRACE-UNESP

⁵ SPRACE-UFABC

⁶ Università di Perugia

Abstract

A search for new particles decaying to two Z bosons with subsequent decay to a final state containing two leptons and two quarks, $X \rightarrow ZZ \rightarrow q\bar{q}\ell^-\ell^+$, is presented. Results are based on data corresponding to an integrated luminosity of 19.5 fb^{-1} of proton-proton collisions at $\sqrt{s} = 8 \text{ TeV}$ and collected with the CMS detector at the CERN LHC. Jet sub-structure techniques are exploited for separating the signal from the SM background when the boost of the Z causes the two quarks to merge into the same jet reconstructed in the detector. Limits on a narrow bulk RS graviton benchmark model are set after further optimizing the selections.

This box is only visible in draft mode. Please make sure the values below make sense.

PDFAuthor: EXO-VV analysis team

PDFTitle: Search for a BSM resonance decaying to vector bosons in the semileptonic final state Xto ZZto "(l-l+)"(qbarq")

PDFSubject: CMS

PDFKeywords: CMS, physics, exotica, graviton, boosted jets

Please also verify that the abstract does not use any user defined symbols

1 Log of changes with respect to AN-2013/040_v6

- 2 This current version builds on top of the version *v6* of this same note, accessible at the URL
3 http://cms.cern.ch/iCMS/jsp/openfile.jsp?tp=draft&files=AN2013_040_v6.pdf
4
- 5 The following list summarizes the main changes in the analysis and the text with respect to v6:
- 6 • add in Sect 4.2 a plot with the dependence of the pruned mass vs the number of vertices
7 • Editorial plots after suggestions received at the approval talk
8 • Fix details of the explanation of procedure for V-tagging efficiency in Sect 6.2

A large, faint watermark-style text "DRAFT" is printed diagonally across the page. The letters are outlined in light gray and slanted upwards from the bottom-left towards the top-right.

9 **Contents**

10	1	Introduction	3
11	2	Monte Carlo Samples and Data Sets	5
12	2.1	Signal MC	5
13	2.2	Background MC and cross-sections	5
14	2.3	Data samples	6
15	3	Event Reconstruction and Selection	11
16	3.1	Events cleanup	12
17	3.2	Trigger and skim requirements	14
18	3.3	Lepton requirements	15
19	3.4	Jet requirements	19
20	4	Reconstruction of the bosons	20
21	4.1	Leptonic Z reconstruction	20
22	4.2	Hadronic Z – single jet interpretation	20
23	4.3	Hadronic Z – double jet interpretation	24
24	5	Data-MC comparison	26
25	5.1	Kinematic distributions related to individual physics objects	26
26	5.2	Kinematic distributions related to the Z bosons	30
27	6	Resonance Reconstruction and Final Event Selection	37
28	6.1	Optimization Procedure and Selection Requirements	37
29	6.2	Efficiency of V-tagging from $t\bar{t}$ control region	41
30	6.3	Reconstruction of the heavy resonance and multiple event candidates in an event	41
31	6.4	Summary of the final event selection	43
32	7	Modeling of Signal and Background	44
33	7.1	Parametrization of the signal shape	44
34	7.2	Background estimation from the $M_{J(J)}$ sidebands	51
35	8	Systematic Uncertainties	59
36	8.1	Lepton energy scale, resolution, selection, and trigger	59
37	8.2	Jet Energy Scale and Resolution	60
38	8.3	Pile-up	64
39	8.4	V-tagging and jet substructure	64
40	8.5	Production mechanism	64
41	8.6	Luminosity uncertainty	64
42	9	Statistical Interpretation of Results	65
43	9.1	Comparison between data and background prediction in the signal region	65
44	9.2	Extraction of the upper limit	65
45	10	Summary and Conclusions	72
46	A	Study of trigger and reconstruction efficiencies for muons	73
47	A.1	Samples	73
48	A.2	Tracking, ID and Isolation Efficiencies	73
49	A.3	HLT Trigger Efficiencies	76
50	B	Quality of the background fits and parametrization studies	80
51	C	Bias Studies	83
52	D	Alternative Approach to the Limit-setting Procedure	85
53	E	Extension of the background fit to higher masses	88
54	F	Event Displays	91

55 1 Introduction

56 The Standard Model (SM) of particle physics has been very successful in describing high-energy physics
 57 phenomena investigated so far [1]. The discovery of the Higgs has completed the Standard Model (SM)
 58 as we know it [2, 3]. On the other hand, the SM is expected to be just an effective theory valid at energy
 59 scales up to ~ 1 TeV. The light Higgs mass leaves open the questions about the naturalness of the
 60 SM and leaves the door open to the presence of new physics to stabilize the Higgs vacuum. For larger
 61 scales, the theory predictions violate unitarity unless the constants of the SM are extremely fine tuned.
 62 This problem can be reformulated in terms of the large difference between the mass of the Higgs boson
 63 ($M_H \lesssim 1$ TeV/c²) and the Planck scale, M_{Pl} , where the gravitational force is expected to be of the same
 64 size of the other fundamental forces ($M_{Pl} \sim 10^{16}$ TeV/c²). This is usually called the *hierarchy problem*.

65 A particularly interesting example of physics Beyond the SM (BSM) predicts the presence of Extra-
 66 Dimensions (ED) beyond the 3 + 1 dimensions experienced in our everyday life [4, 5]. The space-time
 67 would then consist of $4 + N$ dimensions, where N is the number of additional ED. The boson carrier of
 68 the gravitational force, the *graviton*, can propagate also in the ED, effectively "diluting" the gravitational
 69 force. The actual scale where gravity becomes strong, $M_{Pl(4+N)}$, would then be much lower than the
 70 one effectively experienced in the 4D brane

$$M_{Pl(4+N)} = \frac{1}{2\pi R} (2\pi R M_{Pl})^{\frac{2}{N+2}} \quad (1)$$

71 Randall and Sundrum proposed a model where there is only one warped ED [6, 7]. Two 4D branes
 72 (the Planck brane and the TeV brane) are separated by the fifth ED with size r_c . If the metric of the
 73 5-th dimension is exponentially warped with a curvature k , the intensity of the coupling between the
 74 graviton and the SM particles will be dumped exponentially with an exponential factor kr_c , explaining
 75 the weakness of the gravitational interaction. The relationship between the M_{pl} and the actual value on
 76 the Planck brane, M_5 is [6]

$$M_{Pl} = (1 - e^{-2kr_c}) \frac{M_5^3}{k} \quad (2)$$

77 This model, known as RS1, has two fundamental parameters: the mass of the first mode of the KK
 78 graviton, M_1 , and the dimensionless coupling strength $\tilde{k} = \sqrt{8\pi} k / M_{Pl}$. The RS1 model predicts that
 79 the graviton couples preferentially to photons and SM fermions. Several searches for such signatures of
 80 the RS1 scenario have been pursued at the TeVatron [8–10] and at the LHC [11–18].

81 Different models with warped ED allow the SM fields to propagate in the 5-th dimension [19–21]. These
 82 models, generally defined as "*Bulk graviton*" models, can deal with the electroweak precision tests and
 83 the current limits on flavor changing neutral currents better than the RS1 model. Furthermore they can
 84 give an explanation to the mass hierarchy in the SM: lighter fermions are those allowed to propagate
 85 farther in the ED, thus having weaker couplings to the Higgs boson localized near the TeV brane. These
 86 models are characterized by different couplings of the graviton to the SM fields, with a large branching
 87 ratio to SM vector boson pairs that can become dominant according to the parameters of the model.
 88 Therefore, the search for gravitons in the vector boson final state (V=W,Z) can be the "golden mode"
 89 for detecting evidences of this type of BSM physics due the large decay rate and the clean experimental
 90 signature [19].

91 Despite of the appeal of the specific Bulk graviton model, the interest for new physics manifesting itself
 92 in vector bosons covers a much broader spectrum of scenarios. Many other BSM models propose the
 93 existence of new resonances coupling to pairs of vector bosons.

94 Ref. [22] considers a spin-1 particle decaying to ZZ. Hidden valley models admit in principle BSM heavy
 95 particles of any spin state decaying to ZZ [23]. Even if the final state is always composed by two vector
 96 bosons, the underlaying physics and the kinematics of the events can differ a lot between the different
 97 cases. Even in the ED case, the kinematics of the decay products of a RS1 graviton and a bulk graviton
 98 are distinct because of different spin correlations among the final physics objects. These differences
 99 reflect in very different acceptances and signal efficiencies for a given set of event selections. This

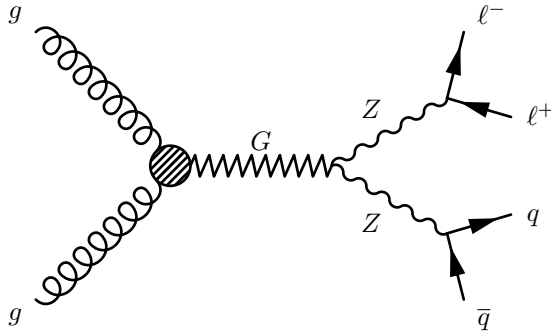


Figure 1: Feynman diagram of the Bulk Graviton production at the LHC, and the decay channel considered in this analysis.

means that a search in this final state must be carried out with a sufficiently generic approach in order not to miss an a-priori open possibility. More targeted selections, exploiting the characteristic kinematics of the signal, can be done tailoring the event selection specifically for some benchmark models judged to be more appealing than others.

The lack of evidence for BSM physics in the searches carried out so far at colliders and electroweak precision tests (EWPT) push the mass of these resonances at the TeV scale, as confirmed by the lack of a signal in the 7 TeV CMS searches [16–18]. In this mass regime, a large fraction of $Z \rightarrow VV$ events are characterized by one boosted V decaying hadronically, reconstructed as a single merged jet.

In this note, a search for TeV resonances going to ZV final states is presented. The focus is not exclusively on spin-2 models, although we use Bulk Graviton samples for studying the signal efficiency. The selections are kept voluntarily loose in order not to depend too much on the nature of the BSM resonance. We reconstruct the Z candidates as $\ell\ell$ ($\ell = e, \mu$) pairs with an invariant mass compatible with the Z mass. We consider two kinds of hadronic V decays: merged jet topology, where a single jet is identified as coming from the V according to a V -tagging procedure (based on jet mass and substructure); the dijet topology, identifying the V with a system of two jets whose invariant mass compatible to the Z mass.

This note is organized as follows. In Sect. 2.1 and 2.2 the MC samples used are listed for the signal and background, respectively. In Sect. 2.3 the datasets analyzed are presented. The triggers used, the identification and selection of the leptons and jets are described in Sect. 3. The reconstruction of the Z bosons and of the heavy resonance tagging of the jets is described in Sect. 4. The final selection, including its optimization, is presented in Sect. 6 followed in Sect. 7 by the description of the data-driven technique for the background estimation. Sect. 8 addresses the estimation of the systematic uncertainties of the measurement. Finally, the statistical interpretation of the results is presented in Sect. 9.

123 2 Monte Carlo Samples and Data Sets

124 2.1 Signal MC

125 As signal hypothesis, the RS graviton [6, 7] and Bulk graviton [19] were considered using a representative set of couplings and masses. A set of simulated samples were privately produced using the full
 126 machinery available in CMSSW, following the conditions used for the official Summer12 campaign.
 127 For the Bulk graviton model, parton-level process files were generated in the LHE format with the
 128 JHU generator version 2.0.2 [24, 25], while showering and hadronization were performed with PYTHIA
 129 version 6.426 [26], with the tune Z2star configuration, while the cross-sections were calculated with
 130 the CALCHEP generator [27], version 3.4. The cross-sections for the $pp \rightarrow G_{bulk} \rightarrow ZZ(WW) \rightarrow$
 131 $\ell\ell(\ell\nu) + qq$ process are shown in Fig. 2. For the RS graviton model, the generation was fully performed
 132 with PYTHIA. GEN-SIM files were produced with CMSSW version 5.2.6, which uses GEANT4 version
 133 9.4.p03-cms for the full simulation of the CMS detector. The DIGI-RAW and RECO steps were pro-
 134 duced with CMSSW version 5.3.2-patch4. These steps include an approximate description of pileup
 135 effects through the mixing of simulated minimum bias at the DIGI level. The simulated minimum
 136 bias samples used are those from the dataset /MinBias.TuneZ2star.8TeV-pythia6/Summer12-
 137 START50_V13-v3/GEN-SIM, and the distribution of the number of pileup events superimposed to the
 138 signal event was done according to the 2012_Summer_50ns_PoissonOOTPU configuration. The gener-
 139 ated samples are summarized in Table 1 and 2.

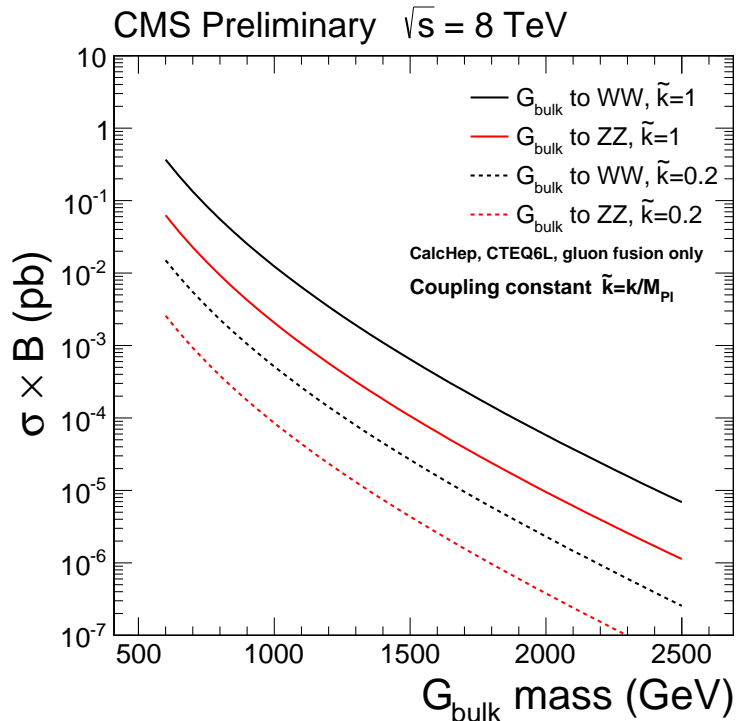


Figure 2: The cross-sections for the $pp \rightarrow G_{bulk} \rightarrow ZZ(WW) \rightarrow \ell\ell(\ell\nu) + qq$ process at a centre-of-mass energy of 8 TeV, as calculated by CALCHEP.

141 In order to validate the private production, we performed a comparison in between the sample /RSGravitonToZZ
 142 _kMp101_M_2000/tomei-RSGravitonToZZ_kMp101_M_2000_STEP3-c8f8ed334db8a7d6f56c6226
 143 6b1dfa5b/USER produced privately, and the corresponding sample /RSGravitonToZZ_kMp101_M_2000
 144 _TuneZ2star_8TeV-pythia6/Summer12_DR53X-PU_S10_START53_V7A-v1/AODSIM, produced in
 145 the scope of the official Summer12 campaign. The comparison is shown in Figs. 3 and 4.

146 2.2 Background MC and cross-sections

147 The dominant background in the $G \rightarrow ZZ \rightarrow 2\ell 2q$ analysis is the inclusive Z production with jets, that
 148 is Z+jets background. Other backgrounds considered are inclusive $t\bar{t}$ production and standard model

Table 1: RS1 graviton signal samples used in the analysis. The cross-sections quoted are for the full decay chain $pp \rightarrow X \rightarrow ZZ \rightarrow 2\ell 2q$, with $\ell = e, \mu$. The \tilde{k} parameter is shorthand for k/M_{Pl} .

Sample	N	$\sigma [\text{pb}]$	\tilde{k}	$M_G [\text{TeV}]$
RS graviton				
/RSGraviton_ZZlljj_kMpl005_M-1000_TuneZ2star_8TeV-MG/				
qili-RSZZ_1000_005_AODSIM-c8f8ed334db8a7d6f56c62266b1dfa5b/USER	38022	5.071E-03	0.05	1
/RSGraviton_ZZlljj_kMpl02_M-1000_TuneZ2star_8TeV-MG/				
qili-RSZZ_1000_02_AODSIM-c8f8ed334db8a7d6f56c62266b1dfa5b/USER	37410	7.854E-02	0.2	1
/RSGraviton_ZZlljj_kMpl02_M-1500_TuneZ2star_8TeV-MG/				
qili-RSZZ_1500_02_AODSIM-c8f8ed334db8a7d6f56c62266b1dfa5b/USER	24966	6.078E-03	0.2	1.5

149 diboson production (WW , WZ and ZZ). All the background samples considered were produced in
 150 the frame of the Summer12 production. The $Z+jets$ sample that we use has been produced with Mad-
 151 Graph. The $t\bar{t}+jets$ sample has been produced with POWHEG. The diboson samples were produced
 152 with Pythia6. A full list of the samples is found in Table 3.

153 2.3 Data samples

154 We use 19.8 fb^{-1} of data collected in 2012 and re-reconstructed with CMSSW_5_3_X in the so-called
 155 “Jan22nd” campaign. The data samples are listed in Table 4. We use only lumisections that have been
 156 declared good for analysis by the central certification team, listed in the following official JSON file:

- 157 • Cert_190456-208686_8TeV_22Jan2013ReReco_Collisions12_JSON.txt

158 for all data-taking eras considered (Run2012A, Run2012B, Run2012C, Run2012D).

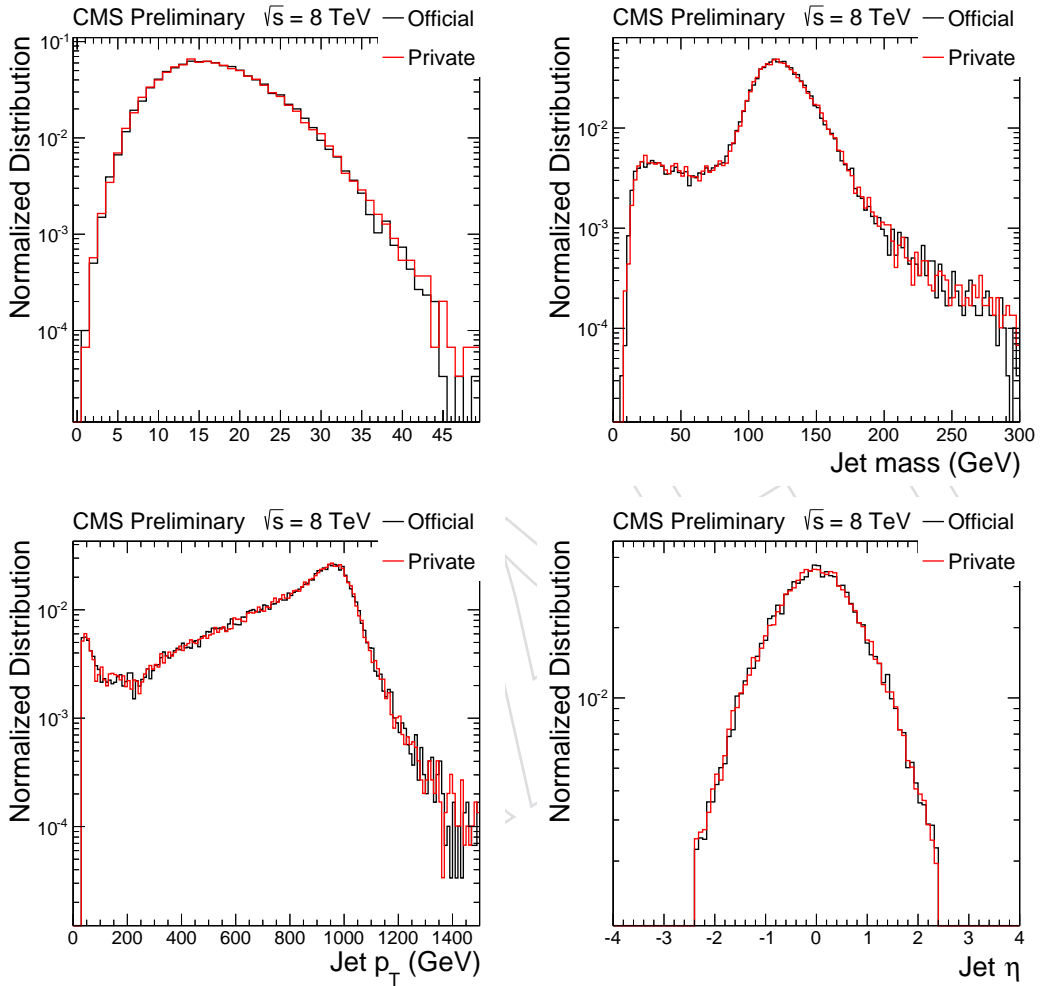


Figure 3: Comparison in between the official sample of RS graviton and a privately produced sample for the same model and same parameters, at RECO level. Top left: number of reconstructed vertices. Top right: leading jet mass. Bottom left: leading jet p_T . Bottom right: leading jet η .

Table 2: Bulk graviton samples used in the analysis. The cross-sections quoted are for the full decay chain $pp \rightarrow X \rightarrow ZZ \rightarrow 2\ell 2q$, with $\ell = e, \mu$. The \tilde{k} parameter is shorthand for k/M_{Pl} .

Sample	N	σ [pb]	\tilde{k}	M_G [TeV]
Bulk graviton				
/JHU_Bulk600_ZZ_c1_v2/tomei-JHU_Bulk600_ZZ_c1_STEP3-c8f8ed334db8a7d6f56c62266b1dfa5b/USER	41965	6.27E-02	1.0	0.6
/JHU_Bulk1000_ZZ_c1_v2/tomei-JHU_Bulk1000_ZZ_c1_STEP3-c8f8ed334db8a7d6f56c62266b1dfa5b/USER	40964	2.06E-03	1.0	1
/JHU_Bulk1500_ZZ_c1_v2/tomei-JHU_Bulk1500_ZZ_c1_STEP3-c8f8ed334db8a7d6f56c62266b1dfa5b/USER	40938	1.06E-04	1.0	1.5
/JHU_Bulk600_ZZ_c02_v2/tomei-JHU_Bulk600_ZZ_c02_STEP3-c8f8ed334db8a7d6f56c62266b1dfa5b/USER	40789	2.58E-03	0.2	0.6
/BulkG_ZZ_lljj_c0p2_M700-JHU/tomei-BulkG_ZZ_lljj_c0p2_M700-JHU-c8f8ed334db8a7d6f56c62266b1dfa5b/USER	10709	9.27E-04	0.2	0.7
/BulkG_ZZ_lljj_c0p2_M800-JHU/tomei-BulkG_ZZ_lljj_c0p2_M800-JHU-c8f8ed334db8a7d6f56c62266b1dfa5b/USER	9359	3.84E-04	0.2	0.8
/BulkG_ZZ_lljj_c0p2_M900-JHU/tomei-BulkG_ZZ_lljj_c0p2_M900-JHU-c8f8ed334db8a7d6f56c62266b1dfa5b/USER	9707	1.74E-04	0.2	0.9
/JHU_Bulk1000_ZZ_c02_v2/tomei-JHU_Bulk1000_ZZ_c02_STEP3-c8f8ed334db8a7d6f56c62266b1dfa5b/USER	41997	8.51E-05	0.2	1
/BulkG_ZZ_lljj_c0p2_M1100-JHU/tomei-BulkG_ZZ_lljj_c0p2_M1100-JHU-c8f8ed334db8a7d6f56c62266b1dfa5b/USER	9358	4.40E-05	0.2	1.1
/BulkG_ZZ_lljj_c0p2_M1200-JHU/tomei-BulkG_ZZ_lljj_c0p2_M1200-JHU-c8f8ed334db8a7d6f56c62266b1dfa5b/USER	40040	2.35E-05	0.2	1.2
/BulkG_ZZ_lljj_c0p2_M1300-JHU/tomei-BulkG_ZZ_lljj_c0p2_M1300-JHU-c8f8ed334db8a7d6f56c62266b1dfa5b/USER	8360	1.31E-05	0.2	1.3
/BulkG_ZZ_lljj_c0p2_M1400-JHU/tomei-BulkG_ZZ_lljj_c0p2_M1400-JHU-c8f8ed334db8a7d6f56c62266b1dfa5b/USER	10709	7.43E-06	0.2	1.4
/BulkG_ZZ_lljj_c0p2_M1500-JHU/tomei-BulkG_ZZ_lljj_c0p2_M1500-JHU-c8f8ed334db8a7d6f56c62266b1dfa5b/USER	9356	4.35E-06	0.2	1.5
/BulkG_ZZ_lljj_c0p2_M1600-JHU/tomei-BulkG_ZZ_lljj_c0p2_M1600-JHU-c8f8ed334db8a7d6f56c62266b1dfa5b/USER	40040	2.59E-06	0.2	1.6
/BulkG_ZZ_lljj_c0p2_M1700-JHU/tomei-BulkG_ZZ_lljj_c0p2_M1700-JHU-c8f8ed334db8a7d6f56c62266b1dfa5b/USER	8009	1.57E-06	0.2	1.7
/BulkG_ZZ_lljj_c0p2_M1800-JHU/tomei-BulkG_ZZ_lljj_c0p2_M1800-JHU-c8f8ed334db8a7d6f56c62266b1dfa5b/USER	9358	9.65E-07	0.2	1.8
/BulkG_ZZ_lljj_c0p2_M1900-JHU/tomei-BulkG_ZZ_lljj_c0p2_M1900-JHU-c8f8ed334db8a7d6f56c62266b1dfa5b/USER	9355	6.03E-07	0.2	1.9
/BulkG_ZZ_lljj_c0p2_M2000-JHU/tomei-BulkG_ZZ_lljj_c0p2_M2000-JHU-c8f8ed334db8a7d6f56c62266b1dfa5b/USER	40040	3.79E-07	0.2	2.0
/BulkG_ZZ_lljj_c0p2_M2100-JHU/tomei-BulkG_ZZ_lljj_c0p2_M2100-JHU-8705aa04e82dbe626002fd8a054cb1d/USER	10499	2.40E-07	0.2	2.1
/BulkG_ZZ_lljj_c0p2_M2200-JHU/tomei-BulkG_ZZ_lljj_c0p2_M2200-JHU-8705aa04e82dbe626002fd8a054cb1d/USER/USER	10706	1.54E-07	0.2	2.2
/BulkG_ZZ_lljj_c0p2_M2300-JHU/tomei-BulkG_ZZ_lljj_c0p2_M2300-JHU-8705aa04e82dbe626002fd8a054cb1d/USER/USER	10710	9.89E-08	0.2	2.3
/BulkG_ZZ_lljj_c0p2_M2400-JHU/tomei-BulkG_ZZ_lljj_c0p2_M2400-JHU-8705aa04e82dbe626002fd8a054cb1d/USER/USER	10709	6.42E-08	0.2	2.4
/BulkG_ZZ_lljj_c0p2_M2500-JHU/tomei-BulkG_ZZ_lljj_c0p2_M2500-JHU-8705aa04e82dbe626002fd8a054cb1d/USER/USER	10078	4.20E-08	0.2	2.5

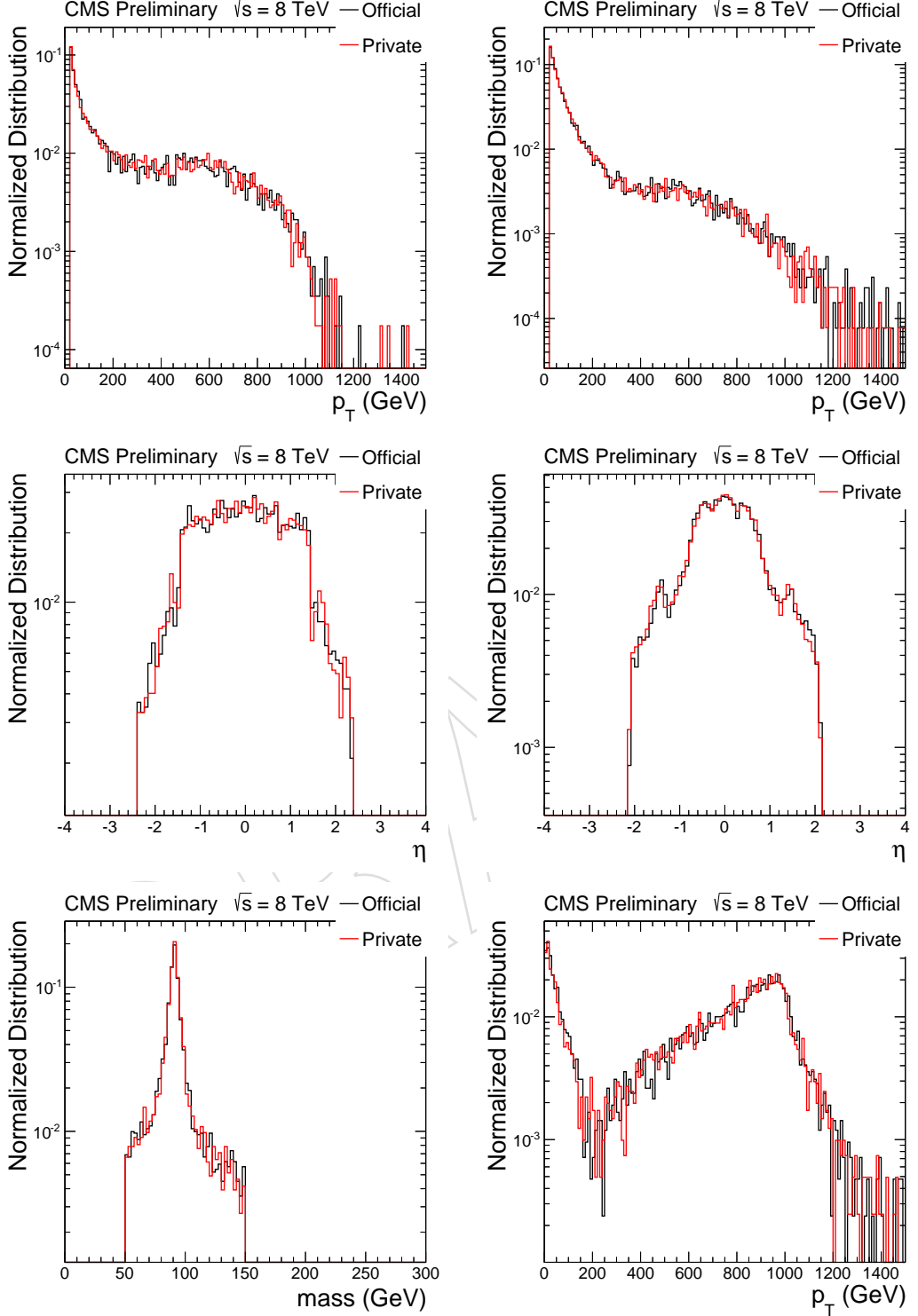


Figure 4: Comparison in between the official sample of RS graviton and a privately produced sample for the same model and same parameters, at RECO level. Top left: leading electron p_T . Top right: leading muon p_T . Middle left: leading electron η . Middle right: leading muon η . Bottom left: Leptonic Z mass. Bottom right: Leptonic Z p_T .

Table 3: Background samples used in the analysis.

Sample	Number of events	σ [fb]
MadGraph samples		
/DYJetsToLL_PtZ-70To100_TuneZ2star_8TeV_ext-madgraph-tarball/	11.76M	5.30E+04
/DYJetsToLL_PtZ-100_TuneZ2star_8TeV_ext-madgraph-tarball/	12.51M	3.92E+04
/TT_CT10_TuneZ2star_8TeV-powheg-tauola/	21.7M	2.3E+05
Pythia samples		
/WW_TuneZ2star_8TeV_pythia6_tauola/	10.0M	5.71E+04
/WZ_TuneZ2star_8TeV_pythia6_tauola/	9.95M	3.32E+04
/ZZ_TuneZ2star_8TeV_pythia6_tauola/	9.80M	8.06E+03

Table 4: Data samples used in the analysis.

Sample	Run Range	\mathcal{L} [pb] $^{-1}$
/DoubleMu/Run2012A-22Jan2013-v1/AOD	190456–193621	889
/DoubleMuParked/Run2012B-22Jan2013-v1/AOD	193833–196531	4426
/DoubleMuParker/Run2012C-22Jan2013-v1/AOD	198022–203746	7114
/DoubleMuParked/Run2012D-22Jan2013-v1/AOD	203768–208686	7318
/Photon/Run2012A-22Jan2013-v1/AOD	190456–193621	889
/DoublePhotonHighPt/Run2012B-22Jan2013-v1/AOD	193833–196531	4429
/DoublePhotonHighPt/Run2012C-22Jan2013-v1/AOD	198022–203746	7152
/DoublePhotonHighPt/Run2012D-22Jan2013-v1/AOD	203768–208686	7318

159 3 Event Reconstruction and Selection

160 Events are processed with PAT in CMSSW_5_3_9 and CMGTools version V5_15_0.

161 The reconstruction and selections applied on the physics objects are described in detail in Section 3.3.1
162 for the muons, Section 3.3.2 for the electrons and Section 3.4.1 for the jets. The general strategy is to keep
163 the pre-selection requirements as loose as possible, in order not to bias the selected sample towards a
164 specific BSM model. For convenience we summarize in Tab. 5 the requirements on the events up until
165 the preselection point, *i.e.*, the requirements described in this section and in Sec. 4. A full set of plots
166 after the pre-selection is presented in Section 5.

DRAFT

167 **3.1 Events cleanup**

168 **3.1.1 Noise Filters**

169 Events are required to pass the following set of standard noise filters:

- 170 • primaryVertexFilterPath
- 171 • noscrapingFilterPath
- 172 • hcalLaserEventFilterPath
- 173 • HBHENoiseFilterPath
- 174 • trackingFailureFilterPath
- 175 • CSCTightHaloFilterPath
- 176 • eeBadScFilterPath
- 177 • EcalDeadCellTriggerPrimitiveFilterPath

178 which remove fake jets from spikes in ECAL and HCAL. The primaryVertexFilterPath filter re-
179 quires the presence of at least one reconstructed vertex, passing the following requirements:

- 180 • obtained from a fit of a suitable set of tracks, i.e., !isFake
- 181 • number of degrees of freedom larger than 4
- 182 • absolute value of the longitudinal coordinate $\text{abs}(z)$ smaller than 24 cm
- 183 • transversal distance to the longitudinal axis ρ smaller than 2 cm.

184 In case more than one suitable primary vertex is found, the vertex with the highest tracks sum- p_T is
185 taken as the primary vertex of the event. This vertex serves as the reference to identify the tracks asso-
186 ciated to the event that fired the trigger and is it used for PU removal in jet clustering.

187 **3.1.2 Pileup removal**

188 The presence of additional interactions with respect to the primary one, known as Pile-up (PU), is ex-
189 pected to affect this analysis in the following ways:

- 190 • additional energy from PU get added to the jets from the main interaction
- 191 • additional low p_T jets fully composed of PU energy get added to the event
- 192 • tracks and calorimetric towers from PU energy deposits get added to the jets from the main
193 interaction thus biasing their angles

194 The amount of PU interaction per event in data and MC is shown in Fig. 5. In the following this dis-
195 tribution in MC has been re-weighted to match the data. In Fig. 6 we show consistency in the number
196 of reconstructed vertexes between data and MC after MC samples have been re-weighted. Since the
197 consistency is good but not perfect in all MC/data plots throughout the note, we reweight the MC to
198 the area of the data for the total normalization. The difference w.r.t. using luminosity weight after pile-
199 up corrections is only $\sim 5\%$. In the procedure of signal extraction we do not anyway rely on the total
200 normalization of the MC.

201 Various algorithms are available to correct for PU effects. The charged particles coming from PU can
202 also be removed before the jet clustering requiring that all the tracks come from the primary vertex with
203 an algorithm called “Charged Hadron Subtraction” (CHS). In this case also the PU effect on jet angles is
204 partially corrected¹. The bias to the jet kinematics coming from neutral hadrons of the PU is corrected
205 with the so-called Fastjet method.

206 In the rest of the analysis the effect of the PU on the jets is corrected using both the CHS and the Fastjet
207 algorithms. Following the recommendations of the MUO and EGM POGs, no attempt is done to correct
208 the high- p_T electrons and muons for PU. The final systematics due to PU on the signal acceptance is

¹Alternatively, only jets with a sizable amount of tracks coming from primary vertex can be considered. This strategy is not used in this analysis.

209 discussed in Section 8.

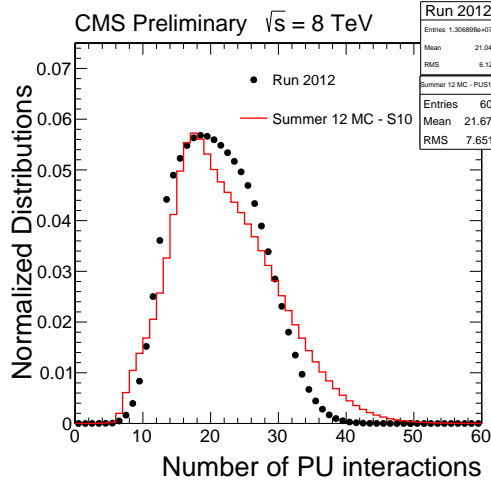


Figure 5: Number of PU interactions in data and MC. In the following the MC sample has been reweighted to match the data.

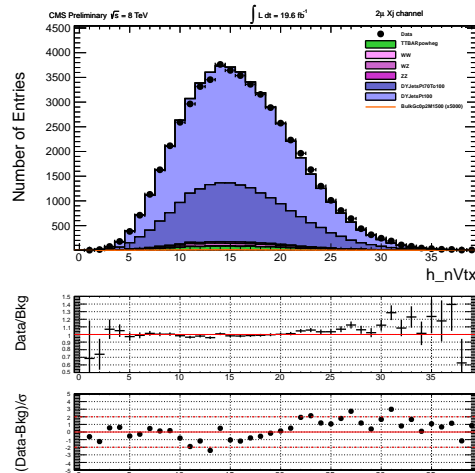


Figure 6: Number of reconstructed vertexes after the reweighting of the MC sample by the pile-up corrections. Points with error bars show data, histograms show contribution of dominant background channels, both after the pre-selection described in Sect. 3.

210 **3.2 Trigger and skim requirements**

211 The results presented in this note are based on the DoubleMu and Photon / DoublePhotonHighPt
212 datasets. Each of these datasets contain at least one un-prescaled trigger with looser requirements than
213 our offline selections. The lowest threshold un-prescaled trigger is used and this trigger changes as
214 instantaneous luminosity rises. These triggers are:

215 • HLT_Mu22_TkMu8_*

216 for the DoubleMu dataset, and

217 • HLT_DoubleEle33_*

218 for the Photon / DoublePhotonHighPt dataset. Those triggers are also chosen for the fact that they
219 are seeded by single-object L1 triggers, which allows us to avoid inefficiencies coming from collimated
220 leptons interfering with each other in the online selection. More details on the definition of the HLT
221 slots are available in the corresponding analysis note [28].

222 The trigger requirement is applied on both the data and the MC. In order to correct for potential mis-
223 modelings of the response of the double muon trigger in the simulation, data/MC scale factors are
224 applied in order to correct the trigger efficiency in the MC. The trigger efficiencies and the scale factors
225 are computed with a Tag-and-Probe technique. The detailed description of the double muon trigger ef-
226 ficiency calculation is presented in Appendix A. For the electrons, the trigger efficiency is 100% in both
227 MC and data thanks to the loose online requirements respect to the offline selection.

DRAFT

²²⁸ **3.3 Lepton requirements**

²²⁹ **3.3.1 Muon Selection**

²³⁰ In the analysis, we use both tracker muons and global muons [29]. In the case of global muons, the
²³¹ momentum assignment is done with the TuneP prescription. The two muons originating from decays
²³² of high- p_T Z are close to each other due to the boost of the boson. In this case, the presence of each
²³³ muon spoils the identification and isolation of the other muon in the pair. There are two issues to be
²³⁴ considered:

- ²³⁵ • Due to the coarser resolution of the muon chambers when compared to the the tracker system,
²³⁶ some of the reconstructed muon hits may be assigned to the wrong muon in the pair. In the
²³⁷ worst case, one of the muons may have no muon hits whatsoever, which will prompt its
²³⁸ failure in many identification criteria. This is referred to as the “greedy muon” problem.
- ²³⁹ • The isolation criteria as defined in the POG don’t make an explicit provision for the presence
²⁴⁰ of the other muon in the pair in the isolation definition. To solve this problem we use a track-
²⁴¹ based isolation relative quantity, explicitly removing from the momentum flow any other
²⁴² muon passing our muon selection.

²⁴³ Figure 7 shows the effect of different identification criteria for the muons. For smaller values of ΔR
²⁴⁴ in between the pair, one sees a drop in efficiency due to the “greedy muon” effect, which is solved by
²⁴⁵ choosing a tracker-based identification criteria for at least one of the muons. Figure 8 shows the effect of
²⁴⁶ the other muon proximity in the isolation variables, on the case where we expect the two muons to be
²⁴⁷ very close (Bulk Graviton sample with $M_G = 1500$ GeV and $\tilde{k} = 1.0$).

²⁴⁸ We select muon candidates with $p_T > 20$ GeV and $|\eta| < 2.4$. At least one of the two muons must have a
²⁴⁹ transverse momentum higher than 40 GeV. The kinematic cuts are the lowest possible compatibly with
²⁵⁰ trigger efficiencies flat in p_T . Furthermore, the muons must pass the high- p_T muon selection:

- ²⁵¹ • muon identified as a GlobalMuon
- ²⁵² • number of muon hits larger than zero
- ²⁵³ • number of matched muon stations larger than one
- ²⁵⁴ • transversal impact parameter d_B smaller than 0.2 cm
- ²⁵⁵ • longitudinal impact parameter d_Z smaller than 0.5 cm
- ²⁵⁶ • number of pixel hits larger than zero
- ²⁵⁷ • number of tracker layer with hits larger than five
- ²⁵⁸ • relative error on the track transverse momentum $\sigma p_T / p_T < 0.3$

²⁵⁹ or the tracker-based muons selection:

- ²⁶⁰ • muon identified as a TrackerMuon
- ²⁶¹ • number of matched muon stations larger than one
- ²⁶² • transversal impact parameter d_B smaller than 0.2 cm
- ²⁶³ • longitudinal impact parameter d_Z smaller than 0.5 cm
- ²⁶⁴ • number of pixel hits larger than zero
- ²⁶⁵ • number of tracker layer with hits larger than eight
- ²⁶⁶ • relative error on the track transverse momentum $\sigma p_T / p_T < 0.3$

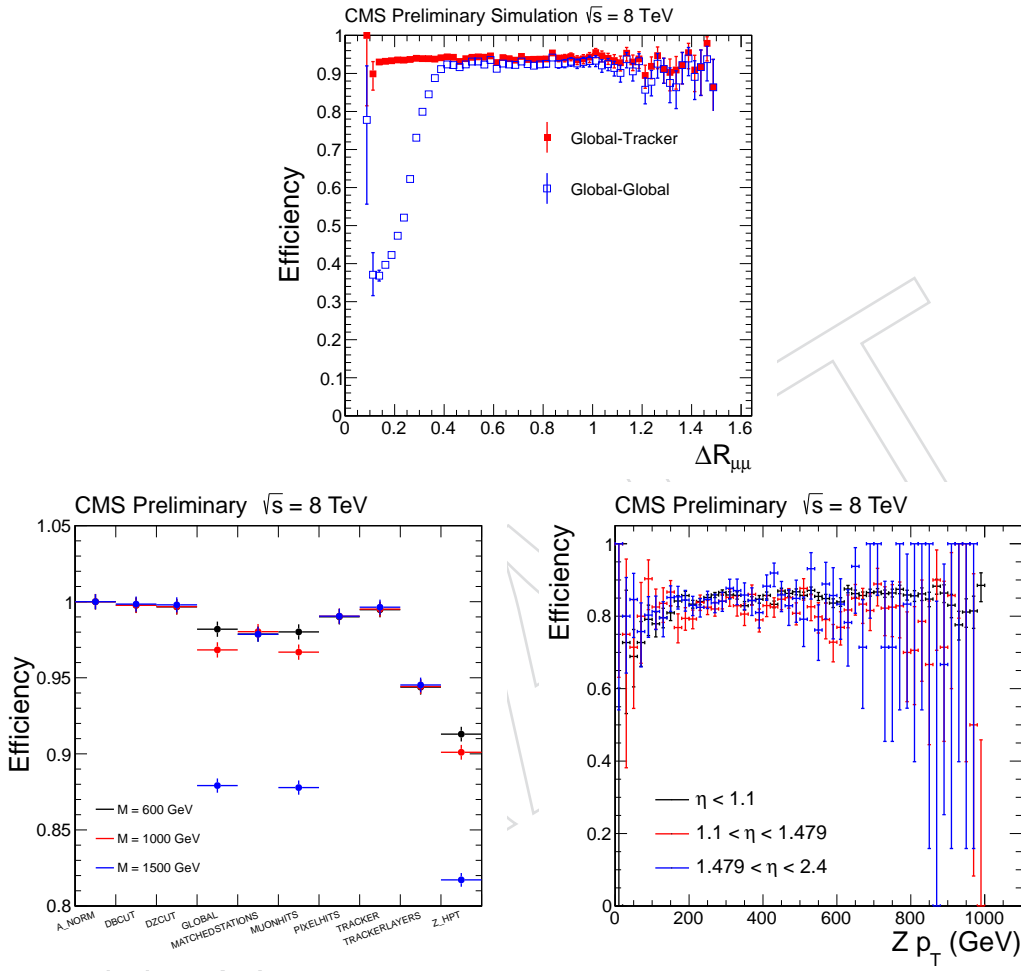


Figure 7: Effects of different identification criteria for the muons. Top: efficiency for requiring two high- p_T or one high- p_T and one tracker-based muon, as function of ΔR . Bottom left: Efficiency for each of the muon requirement criterias, for three different mass points. Bottom right: Efficiency for requiring a high- p_T and a tracker-based muon, as function of η of the leading muon. (CAVEAT: plots in the bottom row done with old HPT muon recipe).

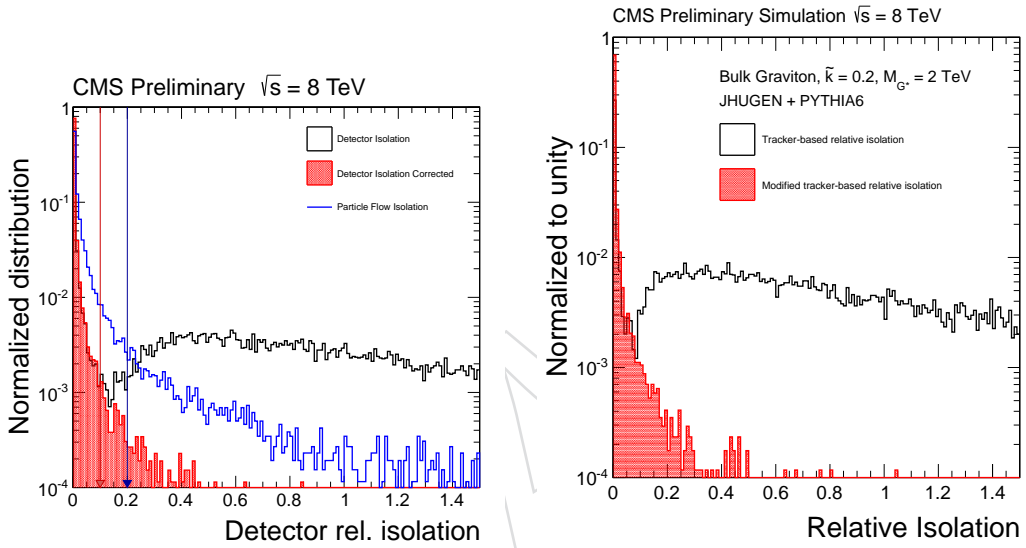


Figure 8: Left: Different isolation choices for the muon identification. White: standard track-based isolation. Blue: Particle Flow isolation. Red: track-based isolation, modified with removal of the other muon. All histograms refer to a signal sample (Bulk Graviton sample with $M_G = 1500 \text{ GeV}$ and $\tilde{\kappa} = 1.0$) where the two muons are expected to be very close. Right: same plot, but for a different signal sample (Bulk Graviton, $M_G = 2000 \text{ GeV}$ and $\tilde{\kappa} = 0.20$) and not showing the Particle Flow isolation.

3.3.2 Electron Selection

We select electron candidates with $p_T > 40$ GeV and $|\eta| < 2.4$. These kinematic requirements are motivated by the thresholds of the HLT trigger slots in use. All electrons must pass the HEEPID identification criterion [30]:

- transversal supercluster energy larger than 35 GeV
- supercluster pseudorapidity (η_{SC}) smaller than 1.442 (for barrel electrons) or in the range 1.56–2.5 (for endcap electrons)
- driven by calorimetric deposits (`isEcalDriven`)
- have $|\Delta\eta_{in}|$ smaller than 0.005 (0.007) for barrel electrons (endcap electrons)
- have $|\Delta\phi_{in}|$ smaller than 0.06 (both for barrel and endcap electrons)
- have the ratio of hadronic to electromagnetic energy smaller than 0.05
- have $\sigma_{i\eta i\eta}$ smaller than 0.03 (for endcap electrons only)
- have either $E_{2\times 5}/E_{5\times 5}$ larger than 0.94 or $E_{1\times 5}/E_{5\times 5}$ larger than 0.83
- have the number of inner layer last hits smaller than 2
- have $|d_{xy}|$ smaller than 0.02 (0.05) for barrel electrons (endcap electrons)

which corresponds to the HEEP standard selection (version 4.1) except for the absence of an isolation requirement. This selection is optimized for close dielectron pairs, as those coming from boosted Z s.

We apply a customized isolation requirement where each electron's footprint is removed from the other electron's isolation cone. Unlike in the muon case, there are three variables that have to be changed for electrons:

- the track isolation variable I_{trk} for an electron is defined as the track scalar p_T sum of the tracks within a $\Delta R = 0.3$ cone around the electron, excluding both i) an inner veto strip of dimensions 0.03×0.3 in (η, ϕ) around the electron in question and ii) an inner veto strip of dimensions 0.03×0.3 in (η, ϕ) around any other electron passing the HEEPID criteria given above.
- the electromagnetic calorimeter isolation variable I_{ECAL} is defined as the scalar sum of E_T of the recHits within a $\Delta R = 0.3$ cone around the electron, excluding both i) an inner veto strip of full-width 3 crystals and/or within a 3-crystal ΔR cone around the electron in question and ii) an inner veto strip of full-width 4 crystals and/or within a 4-crystal ΔR around any other electron passing the HEEPID criteria given above.
- the hadronic calorimeter isolation variable I_{HCAL1} is defined as the scalar sum of E_T of the HCAL caloTowers with centres in a $\Delta R = 0.3$ cone around the electron, excluding those lying within $\Delta R = 0.15$ of any other electron passing the HEEPID criteria given above.

A more detailed description and validation of these variables can be found in [31].

301 **3.4 Jet requirements**

302 **3.4.1 Jet Selection**

303 Jets are reconstructed from the list of Particle Flow (PF) candidates [32] reconstructed in the event.
304 Charged hadrons originating from vertices other than the primary vertex were not used in the jet clustering
305 with the Charged Hadron Subtraction (CHS) procedure. The selected PF candidates are clustered
306 using a Cambridge-Aachen algorithm with distance parameter $R = 0.8$. The jet energy is corrected
307 applying the L₁, L₂, L₃ (L₁, L₂, L₃ and Residual) corrections for MC (data), derived for AK7
308 jets by the JetMET group [33]. This procedure was already validated in other analyses using wide
309 jets [34, 35]. A detailed comparison between CA8 and AK7 jets, both using the AK7 JEC has been
310 recently performed in the context of the validation of the V-tagging algorithms [36, 37]. The study, per-
311 formed on the same 2012 data used in this analysis, showed that the bias on the CA8 jets introduced by
312 the usage of the AK7 JEC is negligible.

313 We select jet candidates with $p_T > 30$ GeV and $|\eta| < 2.4$. In addition, jets are subject to the following
314 loose identification criteria ($> 99\%$ efficiency):

- 315 • muon energy fraction smaller than 0.99
- 316 • photon energy fraction smaller than 0.99
- 317 • charged electromagnetic energy fraction smaller than 0.99
- 318 • neutral hadron energy fraction smaller than 0.99
- 319 • charged hadron energy fraction larger than 0
- 320 • number of constituent particles larger than 1

321 An additional filter on jets in the barrel-endcap transition region of the silicon tracker is applied, follow-
322 ing the studies of Ref.[38]. Jets are rejected if their pseudorapidity falls in the region $1.0 < \eta_J < 1.5$ and
323 the ratio between the multiplicity of charged PF candidates in the jet over neutral PF candidates in the
324 jet, R_{CN} , is larger than 2. The goal of this filter is to remove jets where the tracking software behaves in
325 an anomalous way, and many fake tracks are associated to the jet.

326 4 Reconstruction of the bosons

327 The reconstruction of the Zboson candidate from the physics objects selected as described in Sect.3 is
 328 a crucial step in the exact determination of the event kinematics. While the leptonic Zis treated in the
 329 standard way used at CMS, the hadronic Zrequires special care because of the highly boosted kinematics
 330 and the details of the hadronization process. Plots of the kinematics of the reconstructed Zafter the
 331 preselection cuts are presented in Sect.5.

332 4.1 Leptonic Z reconstruction

333 Z candidates are formed from oppositely charged same-flavor lepton pairs with invariant mass in the
 334 range [70,110] GeV. For resonances with masses $M_X > 600\text{GeV}$, a preselection threshold of 80 GeV on
 335 the p_T of the Zis the highest one that does not introduce any inefficiency. For this reason, we apply a cut
 336 $p_{T,Z} > 80$ GeV.

337 4.2 Hadronic Z – single jet interpretation

338 When the $V \rightarrow qq$ is boosted with high p_T , the majority of events hadronizes into two highly overlapping
 339 sprays of particles. The jet clustering algorithm will reconstruct the V as a single massive jet. The mass
 340 of the jet and its substructure properties are able to discriminate the $V \rightarrow qq$ against standard QCD jets.

341 *Jet grooming* techniques improve the resolution on the jet mass and help in reducing the effect of pile-up
 342 [39]. The goal of jet grooming is to recluster the jet constituents applying additional requirements that
 343 eliminate soft, large-angle QCD radiation coming from sources other than the hard one where the V
 344 boson was created. Different jet grooming algorithms are available at CMS and their performance on
 345 jets in QCD processes has been studied in detail in [39] and [40]. In this analysis, we chose to use the *jet*
 346 *pruning* algorithm because of its good capability in improving the jet mass resolution and because of the
 347 better operational experience, thanks to the many analyses that already used it at CMS [18, 34, 35, 39, 40].

348 The jet pruning algorithm [41] reclusters the jet constituents removing at the same time soft or large
 349 angle recombinations. The jet pruning algorithm that we use is based on the CA clustering algorithm
 350 with distance parameter, $R = 0.8$. In the reclustering procedure, recombinations of jet constituents
 351 characterized by soft energies are vetoed through a cut on the quantity z_{ij}

$$352 z_{ij} = \frac{\min(p_{T,i}, p_{T,j})}{p_{T,(i+j)}} < z_{cut} \quad (3)$$

353 where the indexes i and j refer to the two jet constituents considered in the recombination step and z_{cut}
 354 is a parameter of the pruning set to $z_{cut} = 0.1$. A second requirement is applied on the ΔR ($\Delta R =$
 $\sqrt{\Delta\eta^2 + \Delta\phi^2}$) between the two constituents, ΔR_{ij}

$$355 \Delta R_{i,j} > D_{cut} = \varkappa_{pr} \times \frac{m}{p_T} \quad (4)$$

356 In this case, m and p_T refer to the original ungroomed jet and the parameter $\varkappa_{pr} = 0.5$. If any of the
 357 conditions $z_{ij} < z_{cut}$ or $\Delta R_{i,j} > D_{cut}$, is satisfied, the softest of the two branches in the recombination is
 358 taken out of the list of the jet constituents. Otherwise, the two constituents are recombined according
 to the normal CA procedure.

359 The resulted pruned mass exhibits better resolution and smaller biases with respect to the nominal mass
 360 of the particle which originated it (M_Z in case of V -initiated jets, ~ 0 for QCD jets). Therefore we will
 361 use the pruned mass when applying a selection on the jet mass. For reconstructing the kinematics of the
 362 m_{ZZ} resonance we use still the kinematics of the original jet, however. In this way we still use properly
 363 calibrated jets for reconstructing the kinematics of the event. In Fig 9, we see that the pruned mass is
 364 stable against the presence of pileup in the event.

365 In addition, the distribution of the jet constituents with respect to the jet axis provides a further dis-
 366 crimination against standard jets, allowing to highlight the dipole-like nature of the showering. This

367 feature is quantified by several *jet substructure* quantities proposed in phenomenology studies. We con-
 368 sider here a discrimination based on the *N-subjettiness* [42–44]. The original jet is reclustered with the k_T
 369 algorithm, stopping the reclustering when N subjets are found. The N-subjettiness, τ_N , is then defined
 370 as

$$\tau_N = \frac{1}{d_0} \sum_k p_{T,k} \min((\Delta R_{1,k})^\beta, (\Delta R_{2,k})^\beta \dots (\Delta R_{N,k})^\beta) \quad (5)$$

371 where the index k runs over the jet constituents and the distances $\Delta R_{n,k}$ are calculated with respect to
 372 the axis of the $n - th$ subjet. The normalization factor d_0 is calculated as $d_0 = \sum_k p_{T,k} R_0^\beta$, setting R_0 to
 373 the jet radius of the original jet. In the analysis, the N-subjettiness is calculated from the ungroomed
 374 jets with the parameter $\beta = 1$. In particular, the variable able to best discriminate between V –jets and
 375 QCD jets is the ratio of 2-subjettiness over 1-subjettiness, $\tau_{21} = \tau_2 / \tau_1$. In the context of other analyses
 376 at CMS [35, 45, 46], more variables and combinations of them were considered. The final outcome was
 377 that the gains in using more jet substructure variables at the same time were limited, at the price of a
 378 more complicated procedure, hence favoring the usage of only τ_{21} .

379 Fig. 10 shows the correlation between the pruned mass of the jet, transverse momentum, τ_{21} and the
 380 diboson candidate mass, for all the preselected candidates in the signal events generated with a Bulk
 381 Graviton with $\tilde{k} = 0.2$, $M_1 = 1600$ GeV. Fig. 11 shows the same correlations for the dominant background
 382 ($DY + jets$, with $Z/\gamma^* p_T > 100$ GeV).

383 In order to pass the preselection cuts for the single jet topology, the jet must pass the selections described
 384 in Section 4.2 and must have a pruned mass between 40 GeV and 130 GeV, loosely compatible with
 385 the one of a Zboson. No selections on τ_{21} are applied at the preselection level, while this variable is
 386 important at the stage of the final even selection.

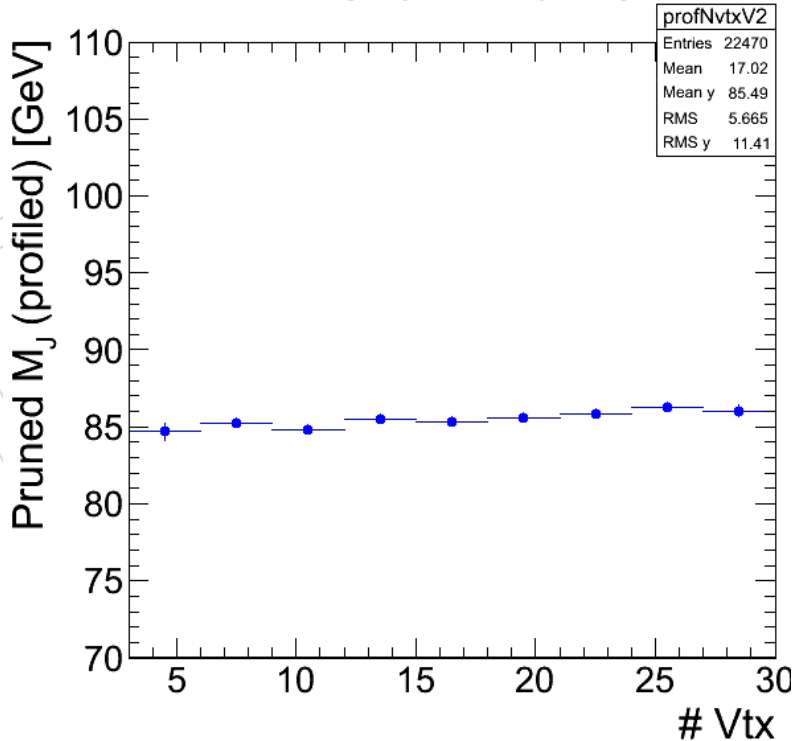


Figure 9: Pruned jet mass as function of the number of reconstructed vertices in the event.

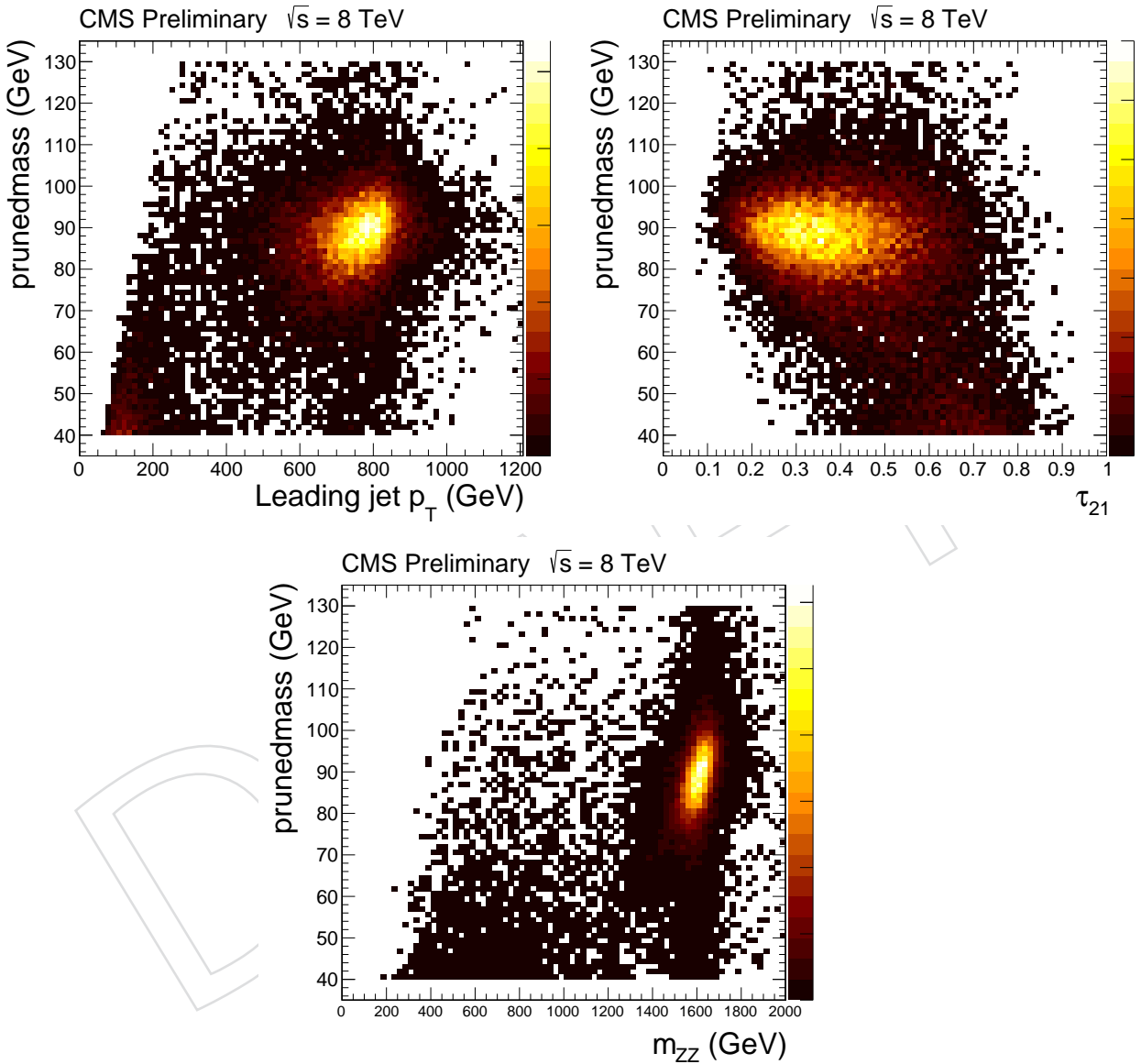


Figure 10: Correlation in between the pruned mass and ungroomed jet p_T (top left), between pruned mass and the N-subjettiness ratio, τ_{21} (top right) and between the pruned mass and the diboson invariant mass m_{ZZ} (bottom), for a Bulk-Graviton sample with $\tilde{k} = 0.2$, $M_1 = 1600 \text{ GeV}$.

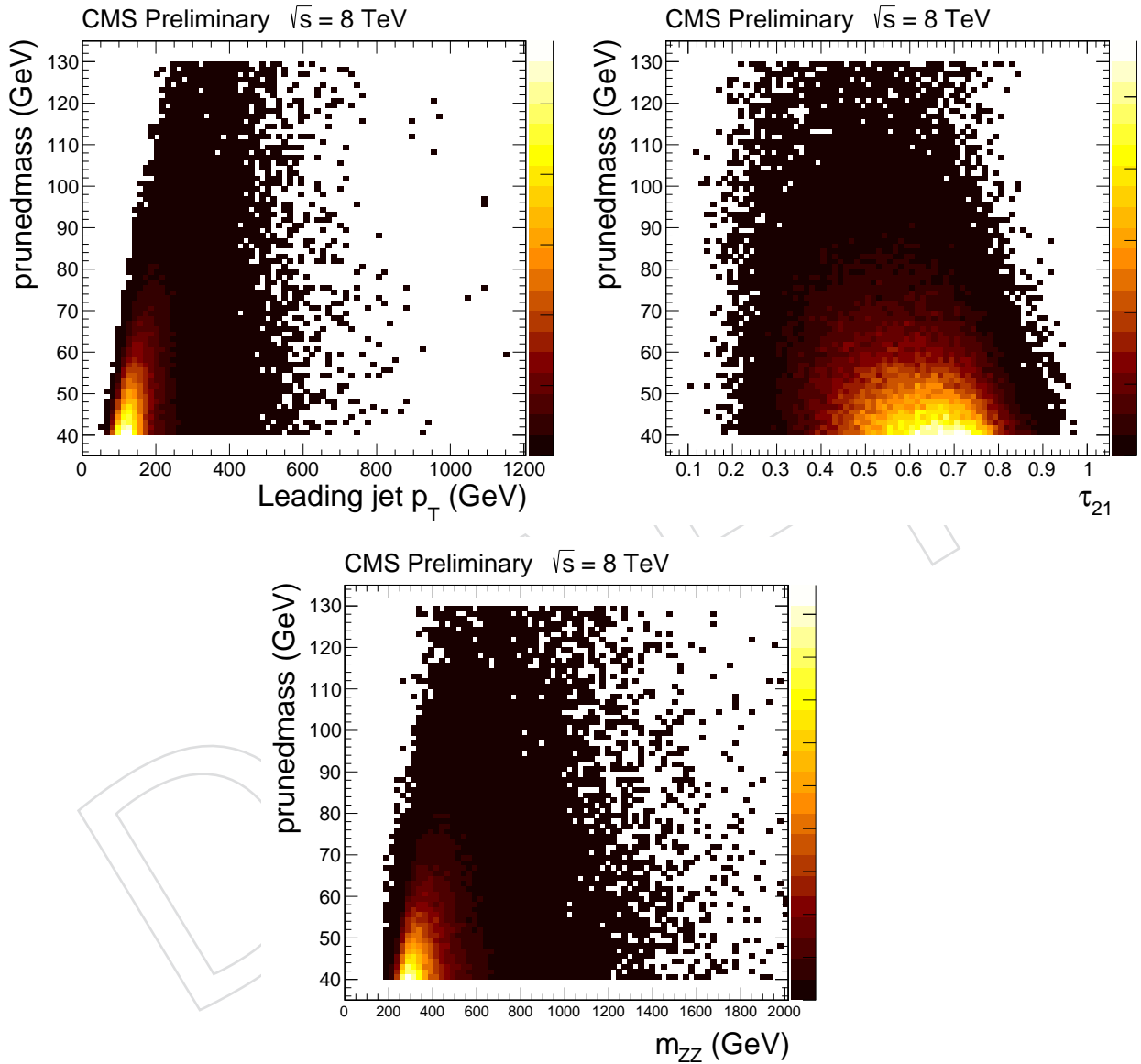


Figure 11: Correlation in between the pruned mass and ungrouped jet p_T (top left), between pruned mass and the N-subjettiness ratio, τ_{21} (top right) and between the pruned mass and the diboson invariant mass m_{ZZ} (bottom), for a DY + jets sample with $Z/\gamma^* p_T > 100 \text{ GeV}$.

387 **4.3 Hadronic Z – double jet interpretation**

388 A number of $V \rightarrow qq$ events, especially those at low $V p_T$, hadronize into a configuration with two
 389 separated, well-defined jets. We form $V \rightarrow qq$ unmerged candidates considering all the pairs of jets
 390 and computing their invariant mass. Dijet candidates with invariant mass inside (outside) the range
 391 [60, 130] GeV are considered as signal (sideband) events. A kinematic fit is applied to the jet pair, impos-
 392 ing a dijet mass value of 91.2 GeV (Z mass hypothesis), the main target of the analysis being a neutral
 393 resonance decaying to ZZ.

394 **4.3.1 Kinematic fit of the dijet system**

395 Finite resolution of the jet energy is the dominant source of uncertainty in both di-jet invariant mass m_{jj}
 396 and di-boson invariant mass m_{ZZ} for Graviton candidates. Therefore, the two variables become highly
 397 correlated, as can be seen in Fig. 12 (left). We account and correct for this effect by applying a kinematic
 398 fit, similar to the best performing option described in [47, 48]. This is effectively exploiting an additional
 399 information in signal events, and is therefore expected to improve the resolution on the Graviton in-
 400 variant mass; as for background, the assumption introduces a constraint which is not correlated to the
 401 underlying physical process, and therefore has the effect of shuffling randomly the events in the final
 402 ZZ invariant mass spectrum.

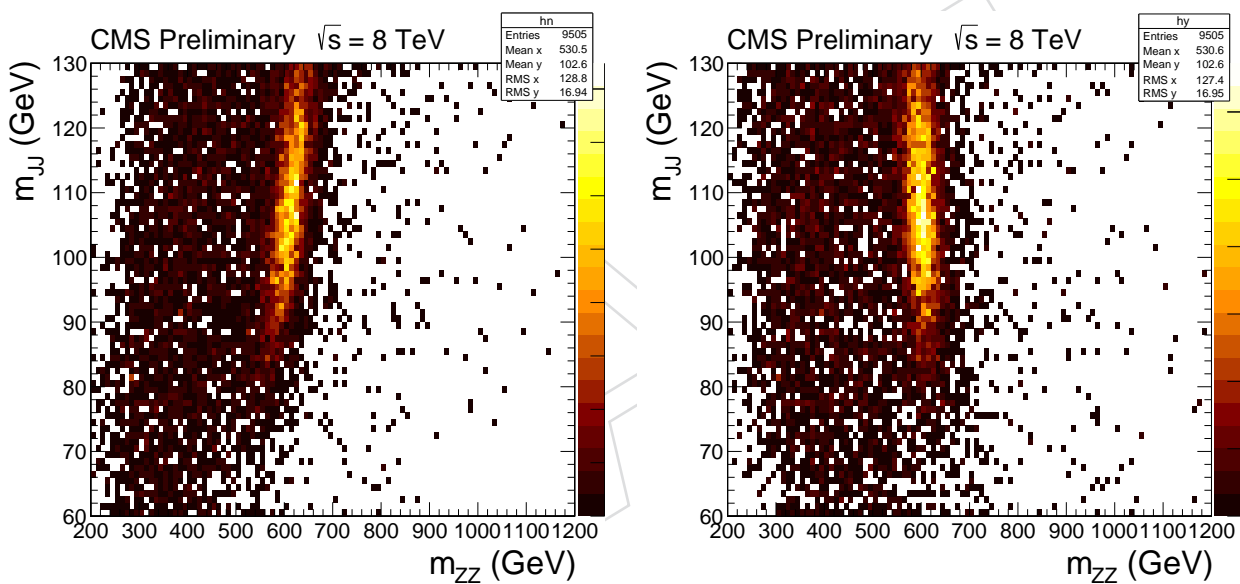


Figure 12: Correlation in between the di-jet invariant mass m_{jj} and di-boson invariant mass m_{ZZ} , for a Bulk-Graviton sample with $\tilde{k} = 0.2$, $M_G = 600$ GeV before (left) and after the usage of the kinematic fit (right).

403 In order to optimally scale the di-jet quadrimomentum to the Z boson mass, we use a kinematic fit to the
 404 two jets. The fit is provided with parametrizations of jet transverse momentum and position resolutions
 405 as functions of transverse momentum and pseudorapidity, and therefore constrains the mass of the di-
 406 jet system to the value of the Z boson mass by modifying the jet quadrimomenta in accordance to their
 407 expected resolutions. This brings an improvement in the resolution on the signal invariant mass, as is
 408 shown by the black curves in Fig. 13 (left).

409 The kinematic fit to the di-jet system also removes the correlation between the di-jet and di-boson in-
 410 variant mass in signal, as can be seen in Fig. 12 (right). This allows a straightforward definition of signal
 411 and sideband regions, through simple rectangular cuts. The same is shown in Fig. 13 for background
 412 (right) and shows how the background shape stays smooth after the kinematic fit.

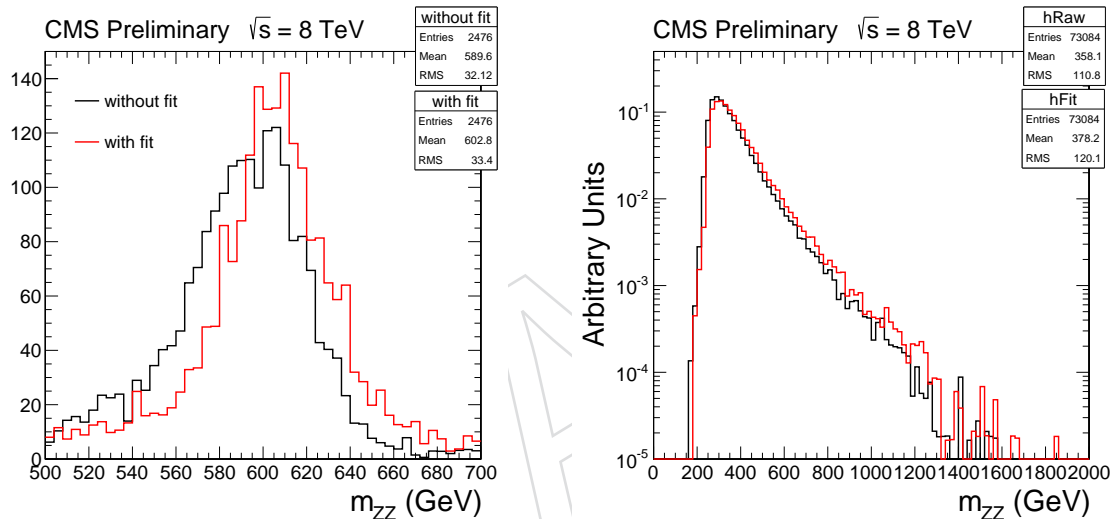


Figure 13: Reconstructed di-boson mass m_{ZZ} for a Bulk-Graviton sample with $\tilde{k} = 0.2$, $M_G = 600 \text{ GeV}$ (left) for the Drell-Yan background sample (right) with (black) and without (red) the usage of the kinematic fit.

413 5 Data-MC comparison

414 In this section we show typical kinematical, ID and event variables for the events passing the pre-
 415 selection requirements described in Sections 3 and 4. Table 5 presents a summary of the same pre-
 416 selection requirements. Such variables are shown here for the data collected in 2012, several background
 417 types and a signal sample at a benchmark mass point.

Table 5: Preselection requirements used in the analysis.

Selection	Value	Comments
Event cleaning		
Primary vertex (PV)	At least one good PV	See Sec. 3.1
Noise filters	Applied	See Sec. 3.1
Pileup removal	CHS and Fastjet algorithms	See Sec. 3.1
Trigger	HLT_Mu22_TkMu8*	DoubleMu Dataset
	HLT_DoubleEle33_*	Photon/DoublePhotonHighPt Dataset
Lepton selections		
Leading lepton p_T	$p_T > 40 \text{ GeV}$	Same for electrons and muons.
Subleading lepton p_T	$p_T > 40 \text{ GeV}$	For electrons.
Subleading lepton p_T	$p_T > 20 \text{ GeV}$	For muons.
Muon η	$ \eta < 2.4$	
Electron η	$ \eta < 2.5$	
Electron fiducial	$ \eta _{\text{SC}}$ out of [1.4442, 1.566] range	Avoid the ECAL gap.
Muon ID	High- p_T Tracker-based < 0.1	See Sec. 3.3.1
Muon Isol. $I_{\text{trkrel}}^{\text{mod}}$	HEEP modified $< 5 \text{ GeV}$ $< 2 \text{ GeV} + 0.03 \cdot E_T$ $< 2.5 \text{ GeV}$ $< 2.5 \text{ GeV} + 0.03 \cdot E_T$	See Sec. 3.3.2
Electron ID		
Ele. Isol. $I_{\text{trk}}^{\text{mod}}$		
Ele. Isol. $I_{\text{ECAL}}^{\text{mod}} + I_{\text{HCAL1}}^{\text{mod}} - 0.28\rho$		EE electrons with $E_T < 50 \text{ GeV}$. EE electrons with $E_T > 50 \text{ GeV}$.
Jet selections		
Jet ID	Loose working point	See Sec 3.4.1
Jet p_T	$p_T > 30 \text{ GeV}$	
Jet η	$ \eta < 2.4$	
Boson selections		
m_{LL}	$70 < m_{LL} < 110 \text{ GeV}$	
m_J (single jet case)	$40 < m_{JJ} < 130 \text{ GeV}$	
m_{JJ} (double jet case)	$60 < m_{JJ} < 130 \text{ GeV}$	
Leptonic Z p_T	$p_T > 80 \text{ GeV}$	
Hadronic Z p_T	$p_T > 80 \text{ GeV}$	

418 5.1 Kinematic distributions related to individual physics objects

419 In Fig. 14, lepton kinematical properties are shown for the muon channel, while in Fig. 15 they are shown
 420 for the electron channel. In Fig. 16 and 17 the modified isolation variables are shown for the leading and
 421 subleading leptons in the electron and the muon channels, respectively. At the preselection level, all
 422 the $X \rightarrow ZZ$ are considered in the event. This means that there can be multiple entries per event in
 423 the distributions. The arbitration between multiple candidates is performed only at the latest stage of
 424 the analysis, as described in Section 6.3. All plots are prepared including candidates from both the jet
 425 multiplicity categories introduced in Section 4.3 (double jet) and 4.2 (single jet).

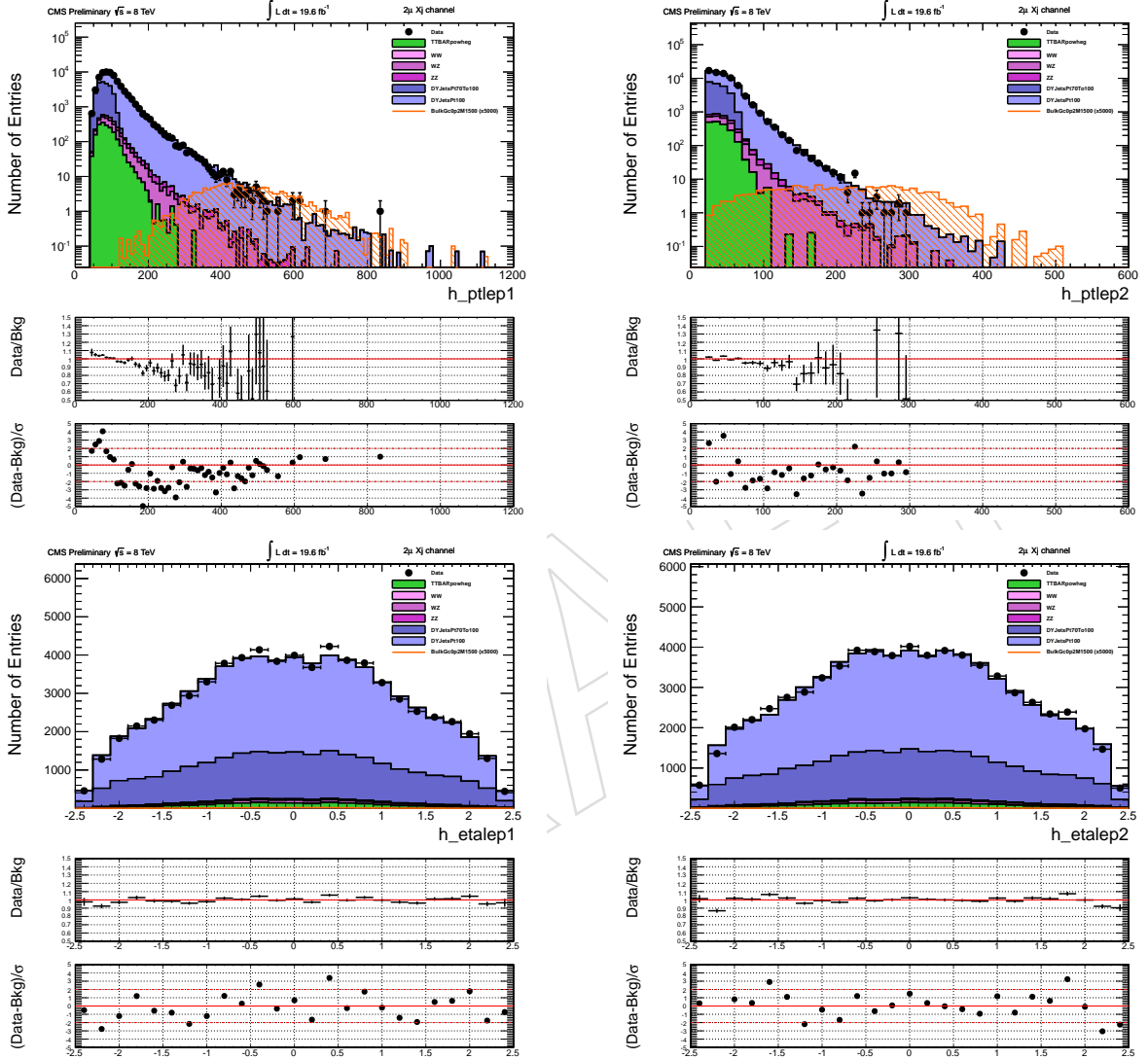


Figure 14: Kinematical distributions for the muons. Top left: p_T of the leading muon. Top right: p_T of the subleading muon. Bottom left:: η of the leading muon. Fourth row: η of the subleading muon.

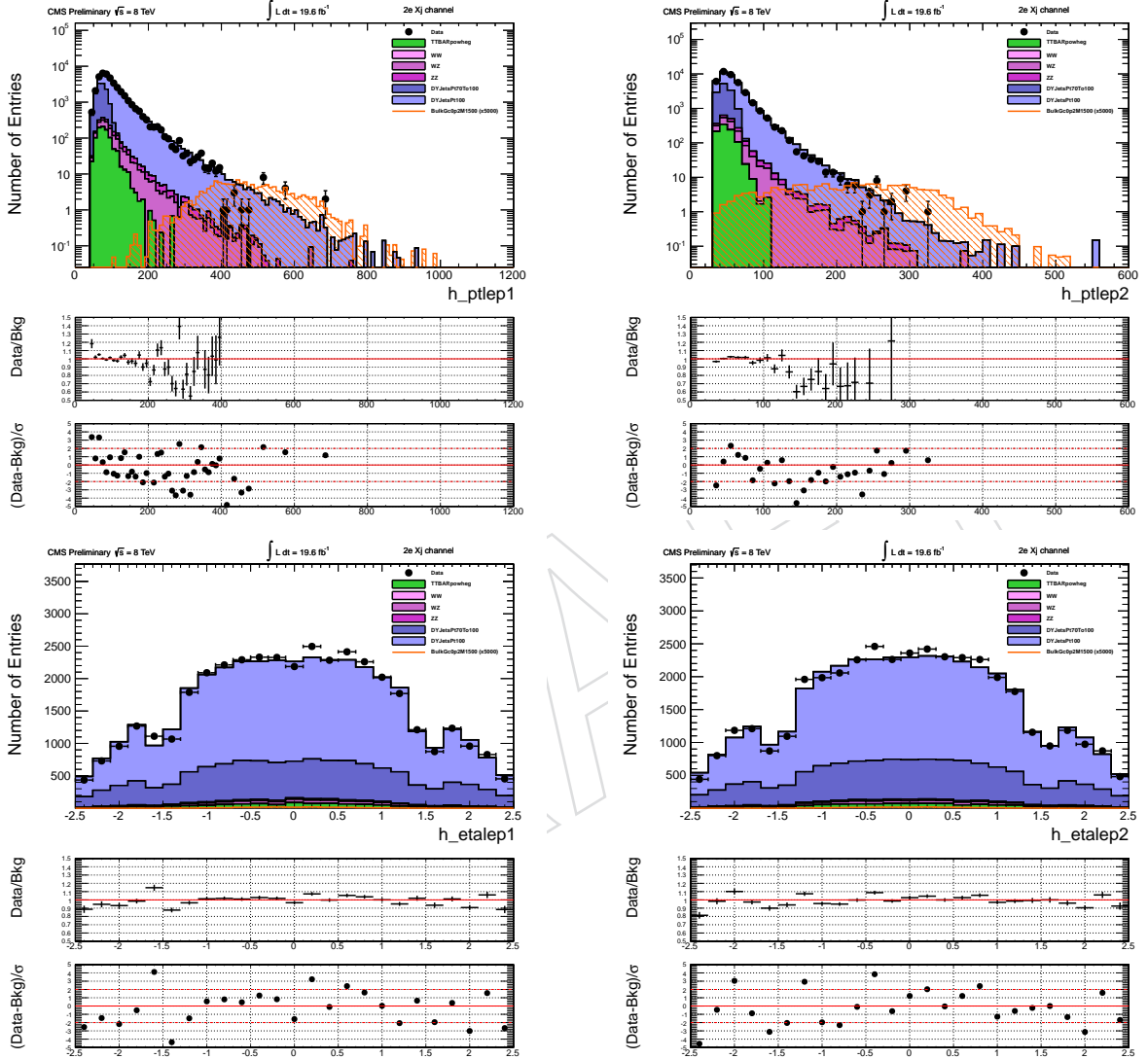


Figure 15: Kinematical variables for the objects in electron channel. Top left: p_T of the leading electron. Top right: p_T of the subleading electron. Bottom left: η of the leading electron. Fourth row: η of the subleading electron.

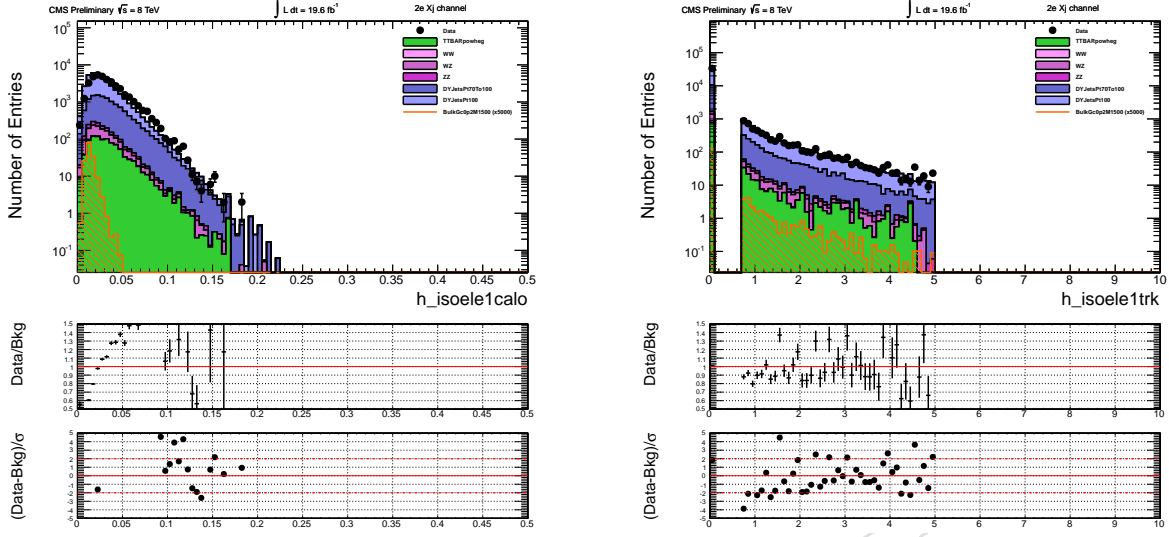


Figure 16: Isolation variables for the electrons, modified as described in the text for the presence of the other nearby electron from the Z. Calorimeter based isolation of the leading (left) and tracker based isolation (right) of the leading electron.

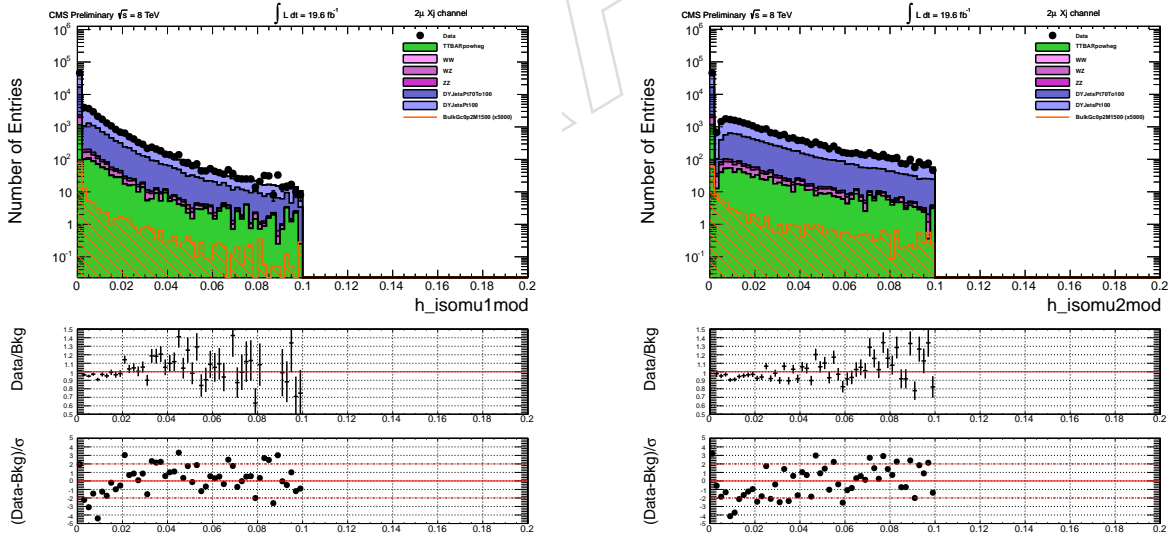


Figure 17: Isolation variables for the muons, modified as described in the text for the presence of the other nearby muon from the Z. The plots show the tracker based isolation of the leading (left) and subleading (right) muon.

426 5.2 Kinematic distributions related to the Z bosons

427 In this section the comparison between data and MC of some basic event and kinematic properties
 428 of the reconstructed diboson system are presented. All the plots refer to the candidates passing the
 429 preselection cuts described in Sections 3 and 4. As in the case of the control plots in Section 5.1, all
 430 the $X \rightarrow ZZ$ candidates are still kept at this stage of the analysis. Those reconstructed using only one
 431 jet which passes the preselections for the single jet topology, are categorized in the single jet topology
 432 (1J). The candidates built from dijets enter in the double jet (2J) category. A comparison between data
 433 and MC for kinematic properties of the $Z \rightarrow \ell^-\ell^+$ candidates is presented in Fig. 18. Fig.19 presents
 434 how events are categorized between the 1J and 2J classes after the preselection cuts. Fig.5.2 shows the
 435 angular distance between the different physics objects i nthe preselected candidates. The p_T and η of the
 436 jets are shown Fig. 20 and 21 for the 1J and 2J categories, respectively. The mass of the pruned jet and
 437 the N-subjettiness ratio τ_{21} , important variables used for the V-tagging in the 1J category, are showin in
 438 Fig.22. Some mismodeling of the MC in the shape of τ_{21} is visible. This effect is taken into account in
 439 the systematic ucnertainties described in Section 8.4. The m_{JJ} distribution for the 2J category is depicted
 440 in Fig.23.

441 The plots demonstrate the overall good quality of the description of the simulation.



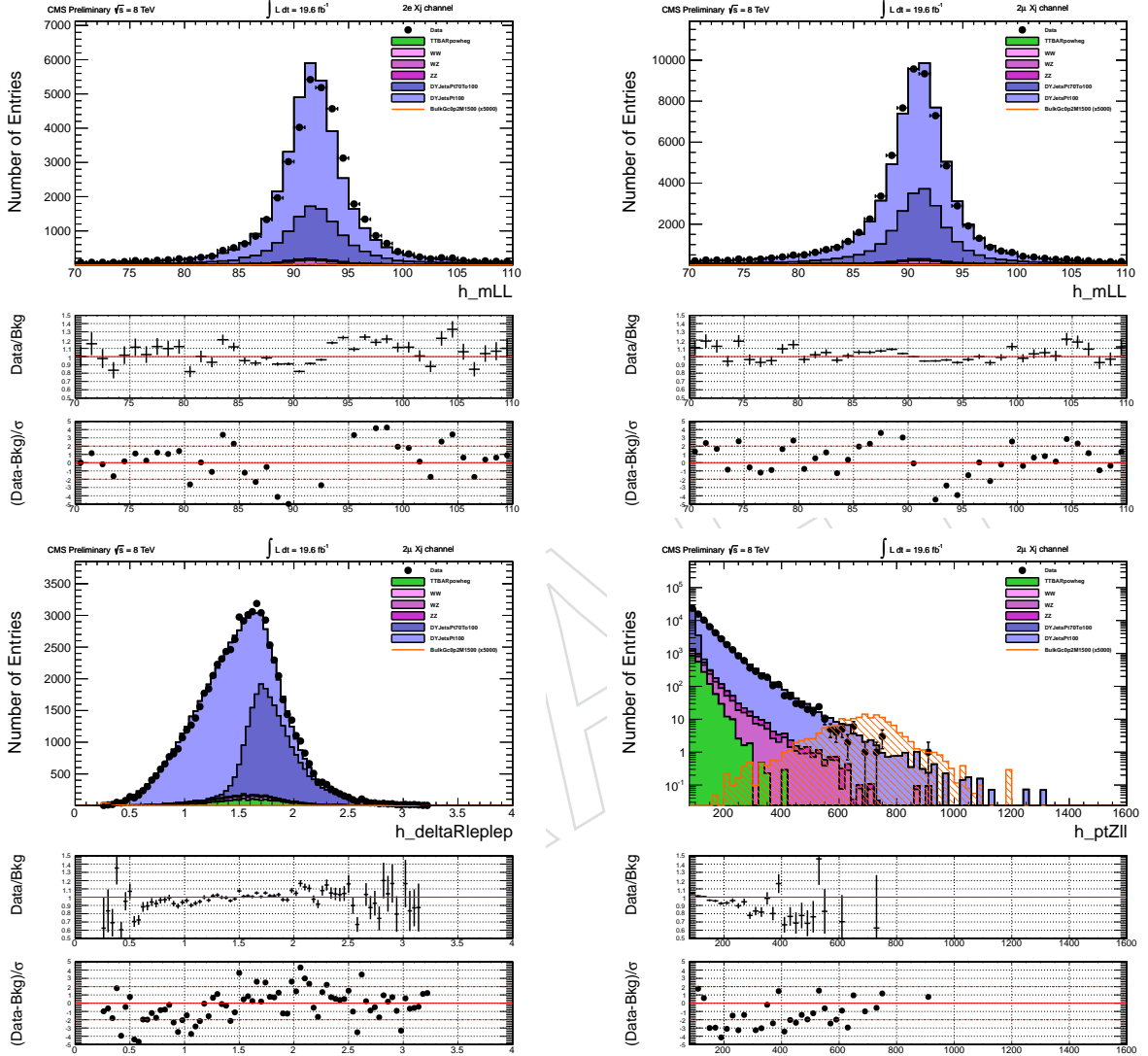


Figure 18: Top row: mass of the leptonic Z reconstructed in the electron channel (left) and in the muon channel (right). Bottom row: ΔR in between the two leptons (left, only muons) and p_T of the leptonic Z (right, only muons). The plots include candidates reconstructed both in the 1J and 2J categories.

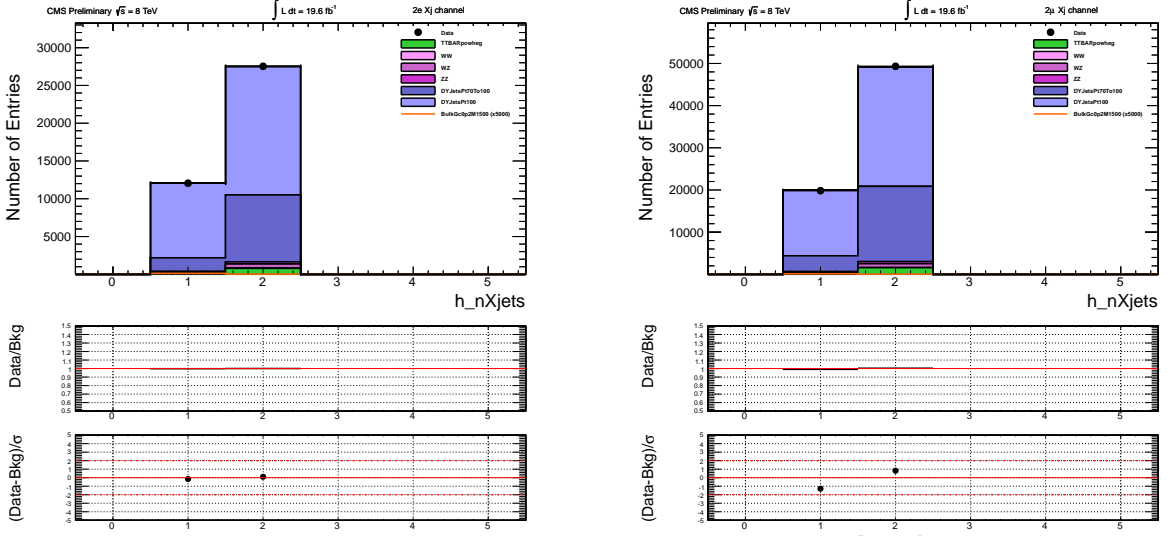
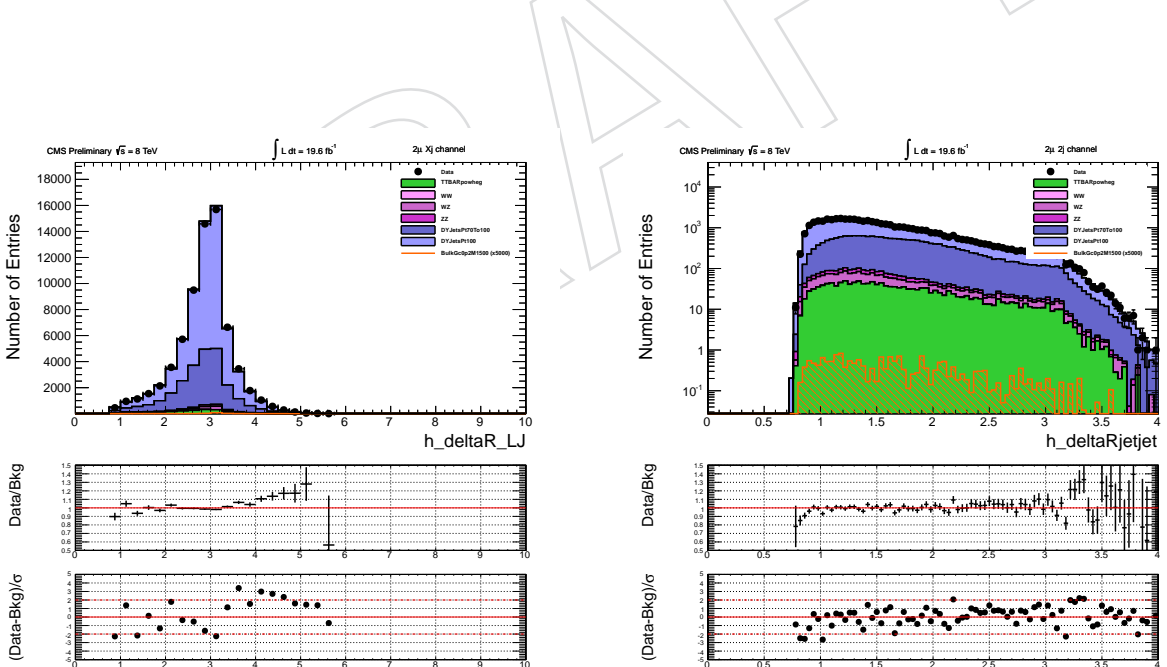


Figure 19: Jet category of the hadronic candidate in the electron (left) and muon (right) channels after the pre-selection cuts.



Left-hand side: ΔR in between the leading lepton used to build the $Z \rightarrow \ell^- \ell^+$ for both single and double jet topologies. Right-hand side: ΔR in between the two jets used to reconstruct the hadronic Z (dijet topology only). The candidates passed the pre-selection cuts in the muon dataset.

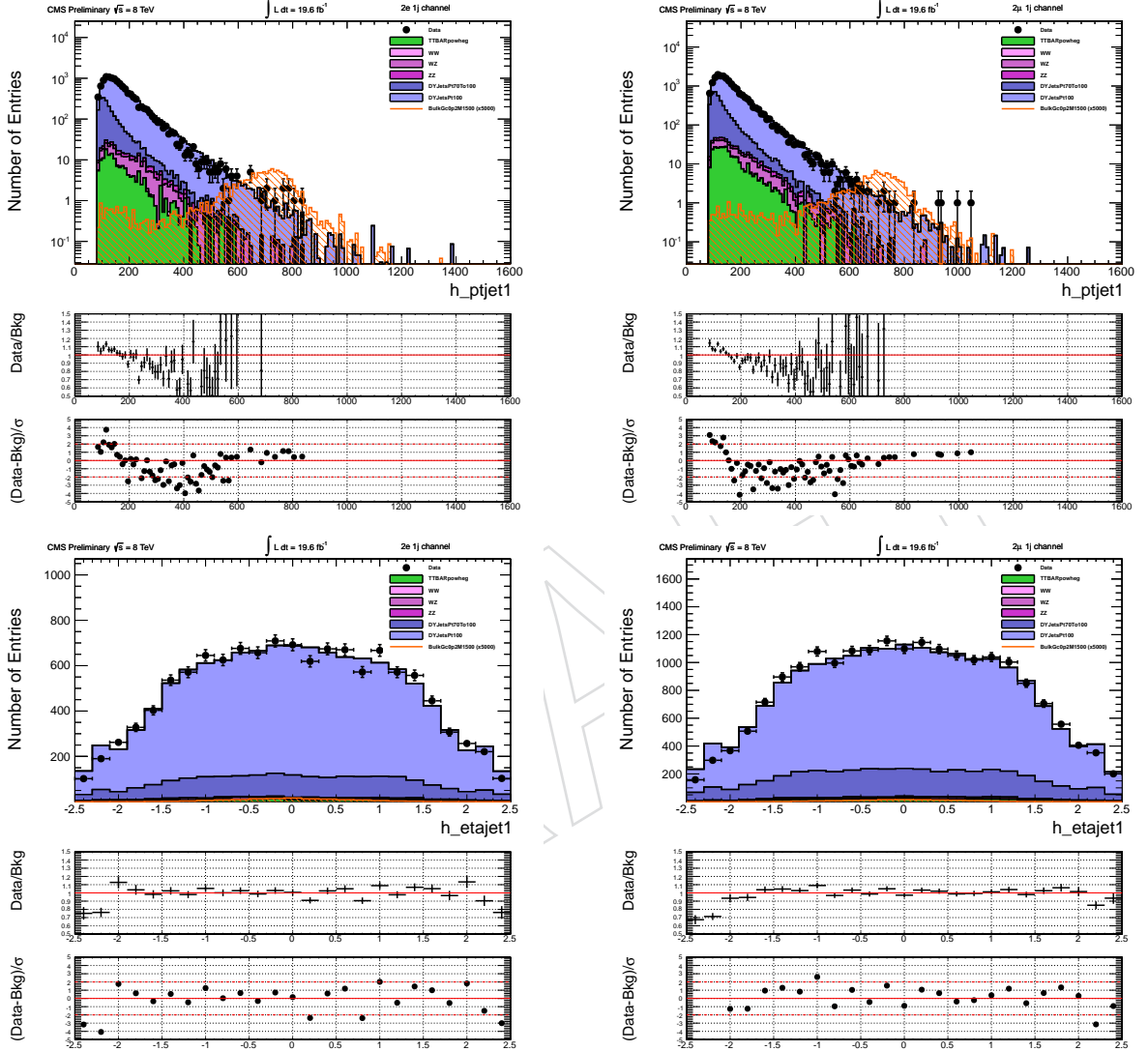


Figure 20: Kinematical variables for the jets used to build the hadronic Z candidate in the 1J category. Top row: p_T of the jet in the electron (left) and muon (right) channel. Bottom right: η of the jet in the electron (left) and muon (right) channel. The $X \rightarrow ZZ$ candidates passed the pre-selection cuts.

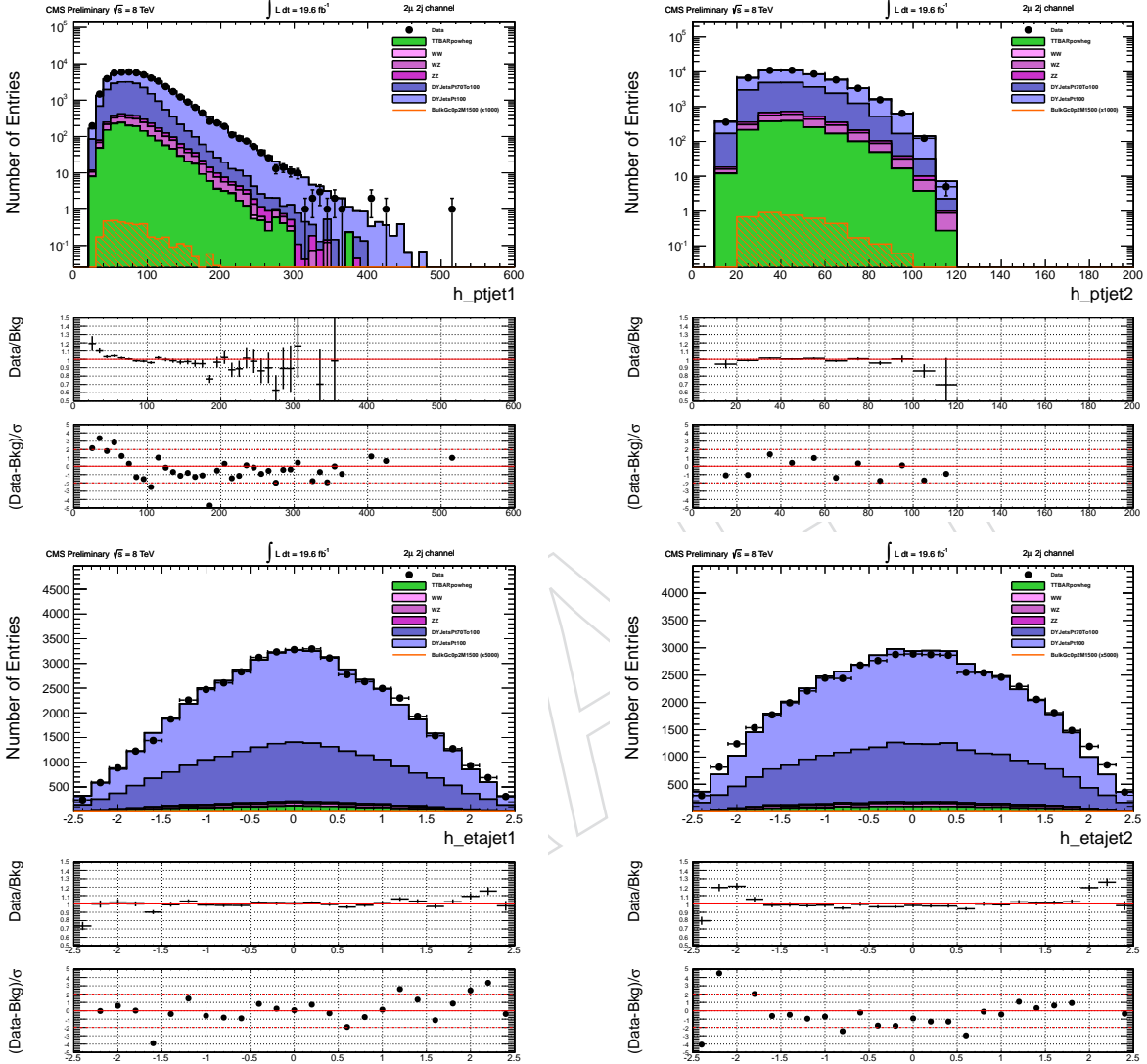


Figure 21: Kinematical variables for the jets used to build the hadronic Z candidate in the 2J category. Top left: p_T of the leading jet. Top right: p_T of the subleading jet (dijet topology only). Bottom left: η of the leading jet. Bottom right: η of the subleading jet (dijet topology only). The $X \rightarrow ZZ$ candidates passed the pre-selection cuts in the muon dataset.

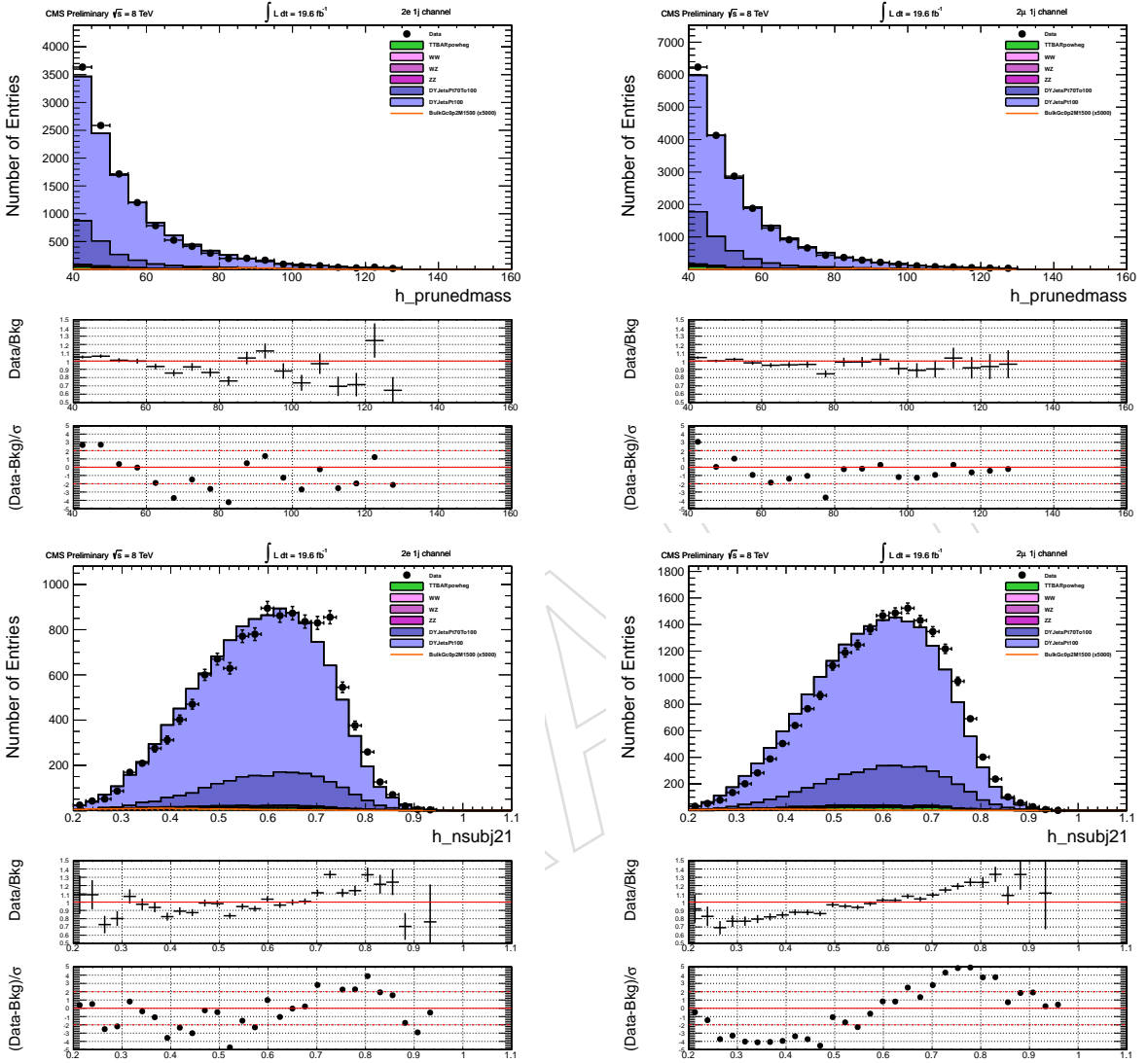


Figure 22: Top row: distributions of the mass of the jet identified as hadronic Z, in the single jet category after jet pruning for the electron (left) and muon (right) datasets. Bottom row: distributions of the 2- to 1-subjettiness ratio, τ_{21} , for the jet identified as hadronic Z, in the single jet category for the electron (left) and muon (right) datasets. The $X \rightarrow ZZ$ candidates passed the pre-selection cuts.

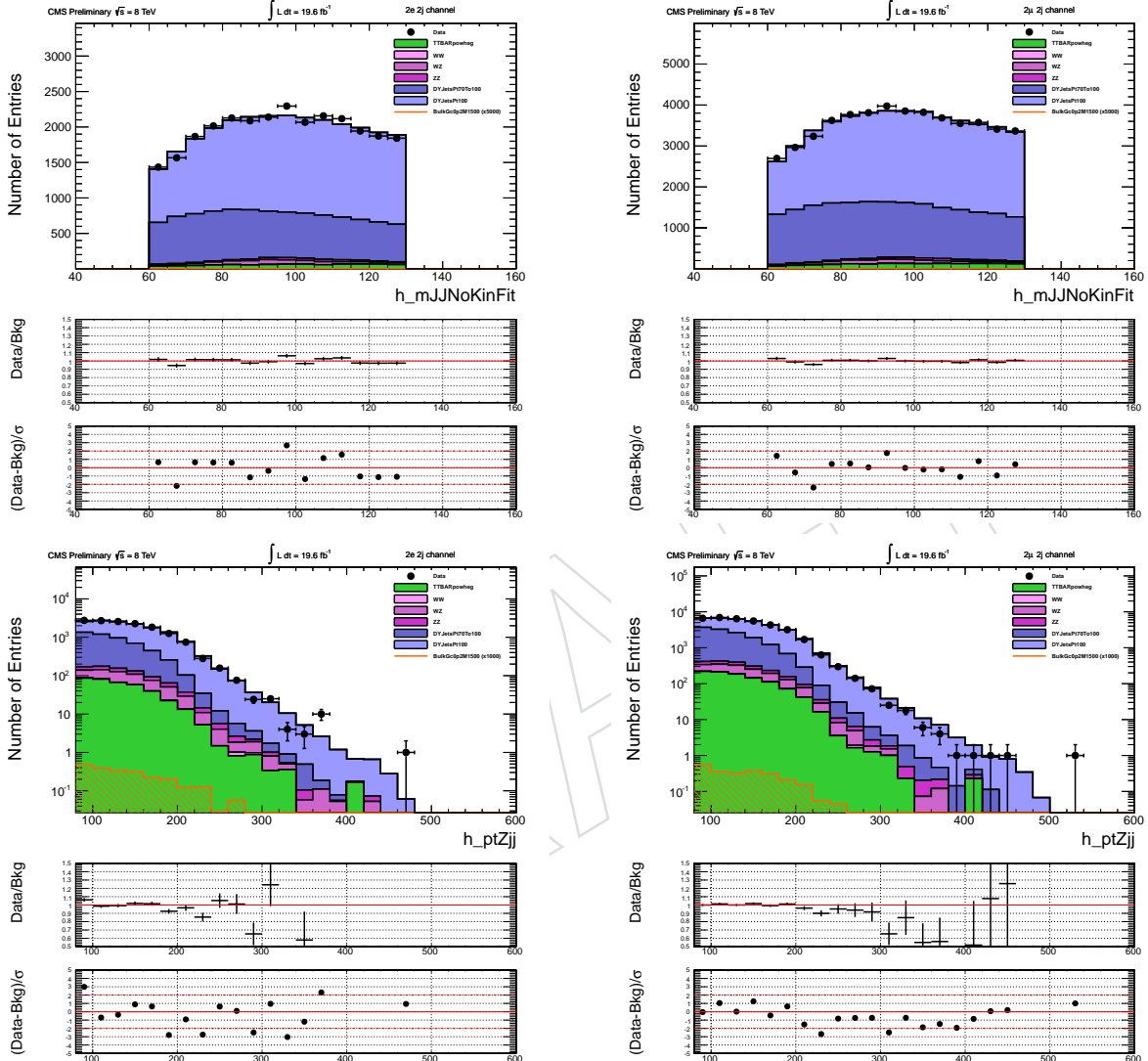


Figure 23: Top row: distributions of the invariant mass of the dijet system in the 2J category, for the electron (left) and muon (right) datasets. Bottom row: distributions of the p_T of the hadronic Z in the 2J category for the electron (left) and muon (right) datasets. The $X \rightarrow ZZ$ candidates passed the pre-selection cuts.

442 6 Resonance Reconstruction and Final Event Selection

443 6.1 Optimization Procedure and Selection Requirements

444 The most powerful handle for discriminating events with two genuine Z bosons from the dominating
 445 $Z+jets$ background is the requirement on the invariant mass of the Z . We found that there is no real
 446 gain in tightening the request on the invariant mass of the dilepton system introduced in Section 4.1,
 447 because also the DY background contains a real Z decaying leptonically and the $t\bar{t}$ background is heavily
 448 suppressed anyway. The cut on the mass of the hadronic system, either in the single jet (1J) or dijet (2J)
 449 topology has strong rejection power against DY. The candidates in the 1J category are required to have
 450 the pruned mass of the jet in the range [70, 110] GeV. The same range is applied on the invariant mass
 451 of the dijet system for the 2J category. The cut was not optimized precisely for this analysis, we rather
 452 based our selection on what was done for previous analyses [16, 48]. The $M_{J(J)}$ cut is slightly larger
 453 than the past analyses in order to minimize the effects of the different M_J resolution in data and MC as
 454 described in Sect.8. The loss in performances due to higher background yield in the signal region was
 455 judged to be acceptable. Although being optimal for the case of a resonance decaying in the ZZchannel,
 456 it retains good efficiency also for the case of a WZ resonance.

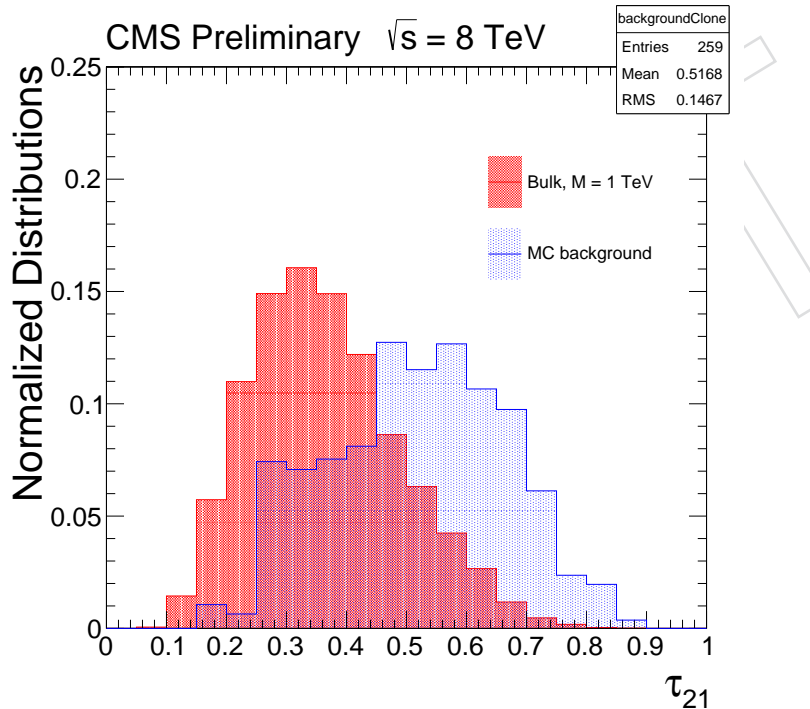


Figure 24: 2- to 1-subjettiness ratio, τ_{21} for signal with $M_G = 1$ TeV and simulated backgrounds.

457 In the single jet analysis, the 2- to 1-subjettiness ratio, τ_{21} , is a key variable able to discriminate between
 458 jets coming from hadronic decays of boosted Z and QCD. As example, in Fig. 24, the distribution of
 459 τ_{21} for a Bulk Graviton signal sample with $M_G = 1000$ GeV and the simulated Drell-Yan background are
 460 shown. In this section we study the optimization of the selection on this variable. Although the variable
 461 has already lost a part of its separation power due to the previous requirement on the jet pruned mass
 462 ($70 < M_J < 110$ GeV), one can see that there is still a degree of separation in between signal and
 463 background. We choose as a figure of merit the quantity suggested in Ref. [49]

$$P = \frac{\epsilon_S}{1 + \sqrt{B}} \quad (6)$$

464 where ϵ_S is the signal selection efficiency and B is the remaining background yield. We perform the
 465 following optimization procedure:

- set a window of $\pm 15\%$ around the target resonance mass.
- histogram the τ_{21} variable for signal events (for the chosen mass) and for background events which pass all the preselection requisites, the cut on the mass of the hadronic Z and also have a reconstructed resonances mass m_{ZZ} in the window defined above.
- set an upper threshold τ_{21}^{\max} and integrate the τ_{21} distributions of signal and background up to the threshold. The value obtained for the signal sample is proportional to the signal efficiency ϵ_S , while the value obtained for the background sample gives B .
- calculate the significance P .

The procedure above is repeated for values of τ_{21}^{\max} ranging from 0.05 from 0.95, in steps of 0.05. The results are shown in Figs. 25 , 26 and 27, for target resonance masses of $M_G = 1000, 1500$ and 1900 GeV. For higher values of the resonance mass, it can be seen how there is a lack of statistics in the simulated background samples. In general, a flat threshold of $\tau_{21}^{\max} = 0.5$ is a reasonable choice. With this flat cut, the analysis is optimal over a broad range of nominal masses, while the loss in performances at high masses is small and hard to quantify because of the limited MC statistics. Furthermore, adopting a m_{ZZ} independent selection avoids any possible biases and sculptings on the m_{ZZ} distribution itself, simplifying the extraction of the background. We show the variation of the best threshold on τ_{21} with the signal mass in Fig. 28, along with the difference in the Punzi figure of merit when choosing the flat $\tau_{21} < 0.5$ requirement as opposed to the optimized one. It is also important to note that the signal distributions are essentially depopulated for values of τ_{21} above 0.75. Therefore, we classify events in the signal region of the 1J topology in two categories:

- **1 Jet, High-purity category:** events in the signal region, with τ_{21} in the $[0, 0.50]$ range.
- **1 Jet, Low-purity category:** events in the signal region, with τ_{21} in the $[0.50, 0.75]$ range.

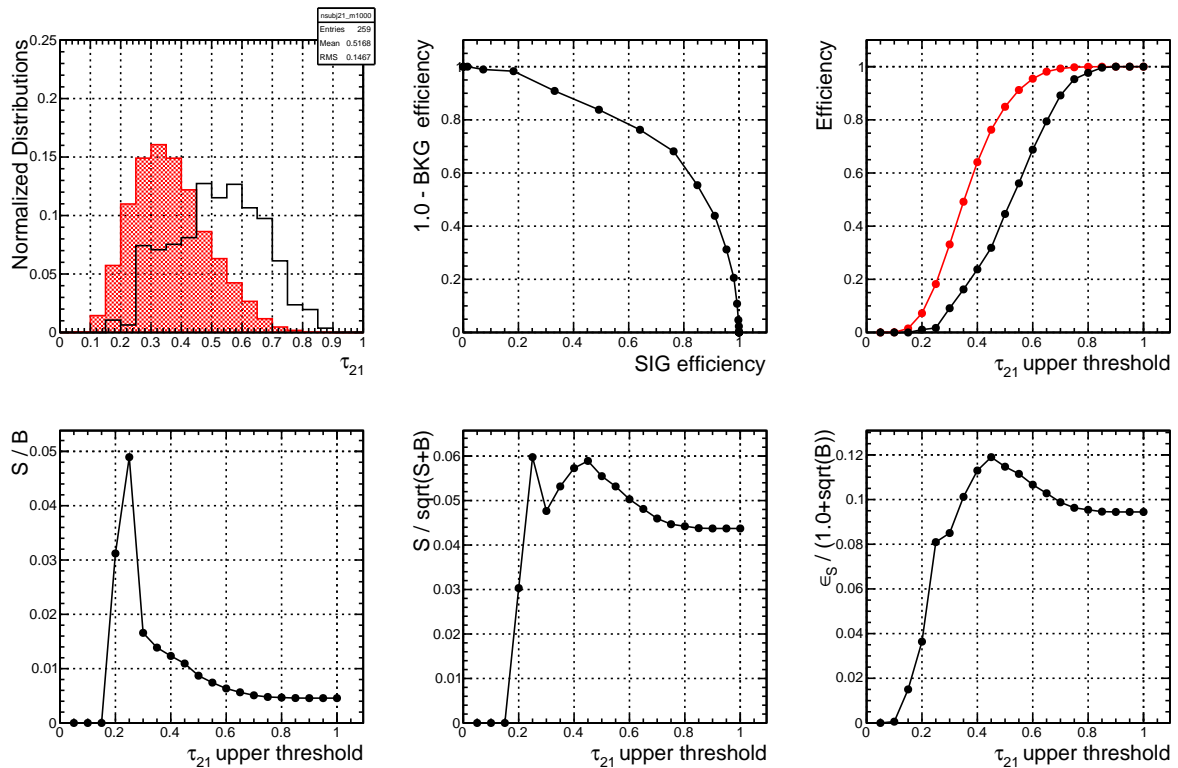


Figure 25: Steps of optimization for $M_G = 1000$ GeV. Top left: distributions of τ_{21} for signal and background. Top middle: signal efficiency \times background rejection curve (ROC curve). Top right: signal (red) and background (black) efficiencies as function of τ_{21} cut. Bottom left: signal S over background B as function of τ_{21} cut. Bottom middle: $S/\sqrt{S+B}$ as function of τ_{21} cut. Bottom right: significance (as defined in Eq.6) as function of τ_{21} cut.

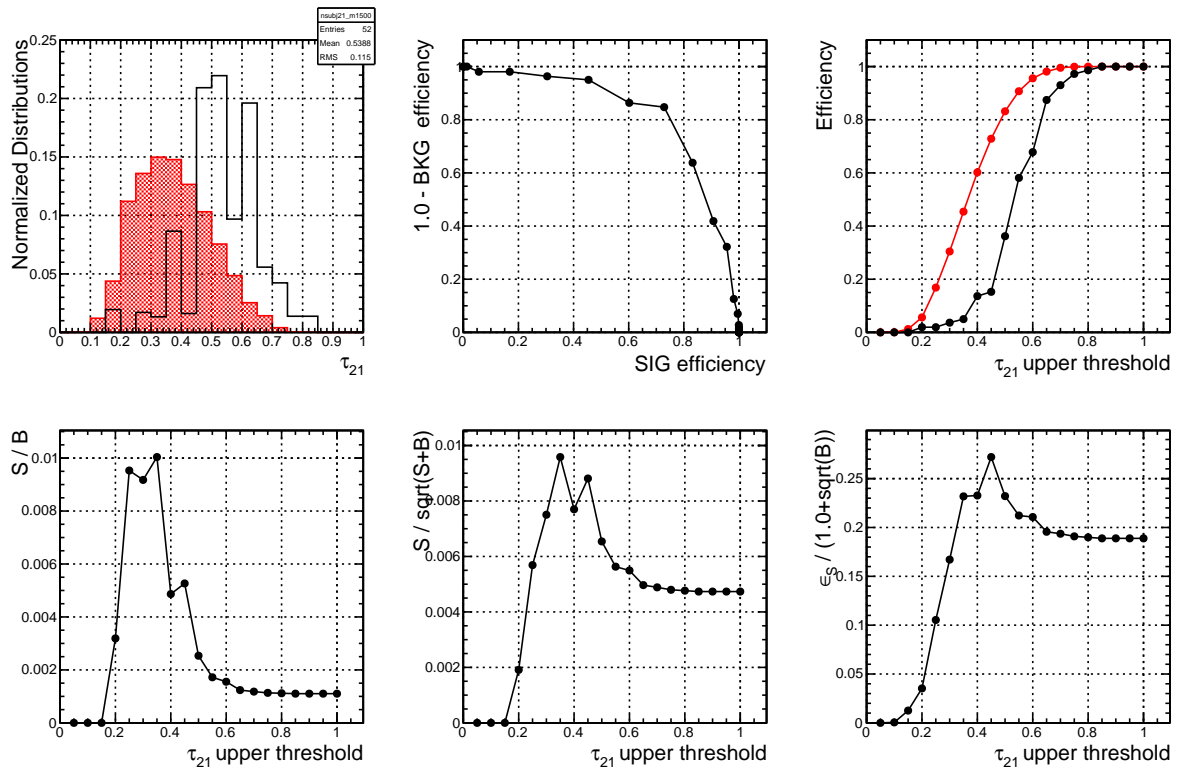


Figure 26: Steps of optimization for $M_G = 1500$ GeV. Top left: distributions of τ_{21} for signal and background. Top middle: signal efficiency \times background rejection curve (ROC curve). Top right: signal (red) and background (black) efficiencies as function of τ_{21} cut. Bottom left: signal S over background B as function of τ_{21} cut. Bottom middle: $S / \sqrt{S+B}$ as function of τ_{21} cut. Bottom right: significance (as defined in Eq.6) as function of τ_{21} cut.

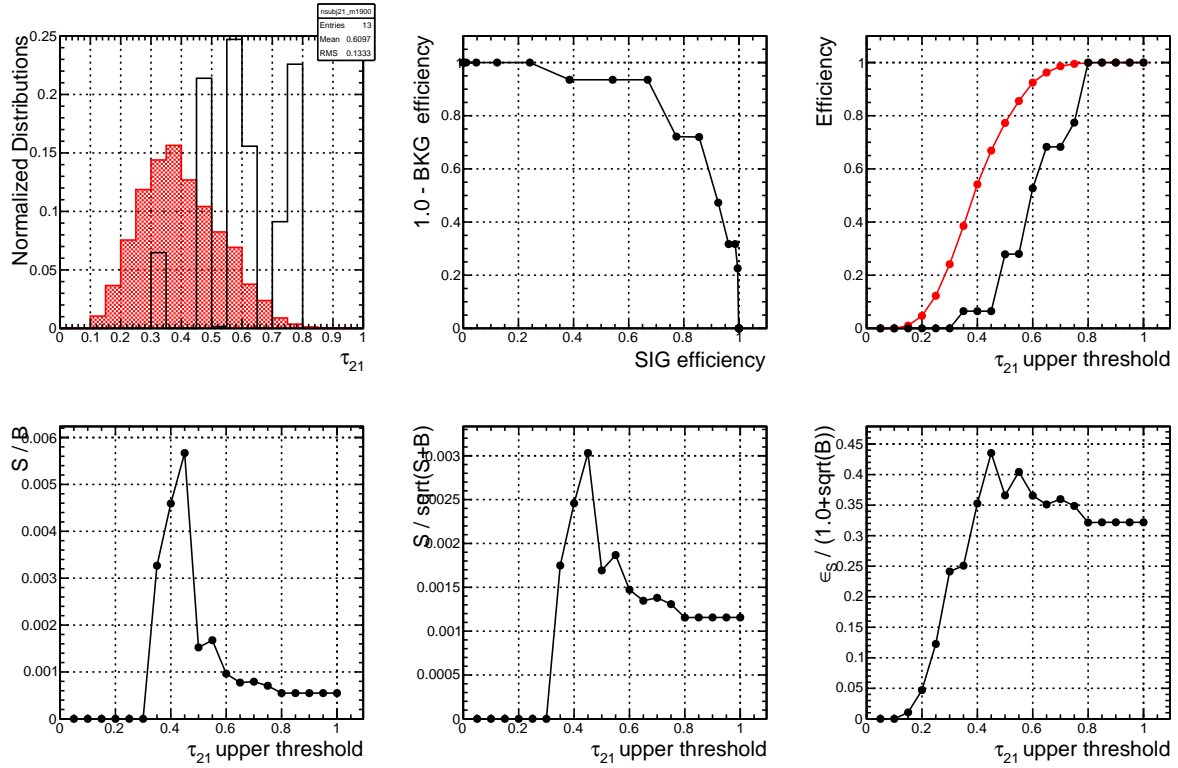


Figure 27: Steps of optimization for $M_G = 1900$ GeV. Top left: distributions of τ_{21} for signal and background. Top middle: signal efficiency \times background rejection curve (ROC curve). Top right: signal (red) and background (black) efficiencies as function of τ_{21} cut. Bottom left: signal S over background B as function of τ_{21} cut. Bottom middle: $S / \sqrt{S+B}$ as function of τ_{21} cut. Bottom right: significance (as defined in Eq.6) as function of τ_{21} cut.

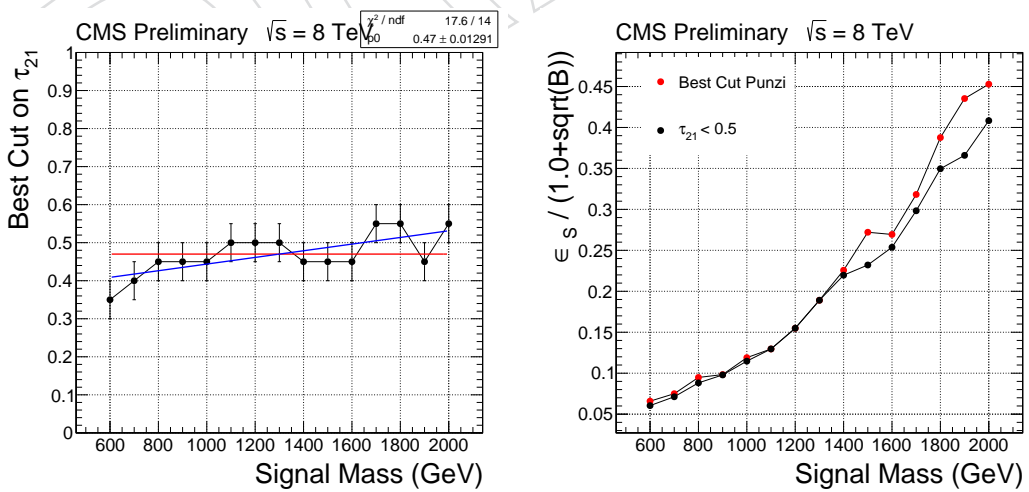


Figure 28: Left: variation of the τ_{21} cut with signal mass, and both a constant (red) and linear (blue) fits. Right: comparison of the fully optimized ("best cut") and flat ($\tau_{21} < 0.5$) thresholds for the figure of merit used for the optimization.

488 **6.2 Efficiency of V-tagging from $t\bar{t}$ control region**

489 The efficiency of the signal selection for the various purity categories is a basic component in the final
 490 statistical analysis and must be controlled with good precision. On the other hand, one can notice from
 491 the data/MC comparison at the preselection level in Fig.22 how the MC describes only approximately
 492 the data. This suggests that one cannot simply trust the efficiency of the V-tagging selection of the MC,
 493 as this number could be different for potential signal events stemming from the collisions. Therefore, a
 494 data-driven procedure to correct the V-tagging efficiency of the MC has been developed, exploiting an
 495 independent control sample.

496 Because of the lack of a pure control sample with Z decaying hadronically and thanks to the kinematic
 497 similarity of W and Z (in first place because of the close values of the two masses), the study of the
 498 normalization uncertainty related to the efficiency of the V-tagging cut is exploits W bosons coming
 499 from top-quark decays. This study is shared with the analysis similar to this one, searching for new
 500 physics in the semi-leptonic decays of pairs of W . More details are given in the analysis notes of this
 501 other analysis [45, 46], here we give only a brief description of the method and the final result². It should
 502 be stressed that because of the close values of the masses of the W and Z and because of the limited
 503 resolution of the jets, this extrapolation is still reliable.

504 The analysis of a $t\bar{t}$ enriched independent control sample, studies the differences between data and
 505 MC and aims at giving a data/MC scale factor by which correcting the MC V-tagging efficiency. The
 506 uncertainty on this scale factor is then assigned as systematic uncertainty of the method. The $t\bar{t}$ events
 507 in the control sample were selected in the semi-leptonic decay channel. Events in both data and MC are
 508 then divided in different categories according if

- 509 • they pass the cut $\tau_{21} < 0.50$ ("passing" sample) or they fail it ("failing" sample);
- 510 • in the case of MC, if the reconstructed jet with the highest p_T is matched at the GEN-level to
 511 a W (geometrical matching done asking for $\Delta R < 0.3$).

512 The procedure follows the steps of a typical tag-and-probe technique. The efficiency for passing both
 513 the HP tagging and the cut on the jet pruned mass in a window $[65, 105] \text{ GeV}/c^2$, ε_{HP} , is extracted from
 514 a simultaneous fit to the pruned mass distributions in the pass-fail distributions. The functional forms
 515 of these two components were chosen using the matched and unmatched categories in the MC. The
 516 data/MC scale factors for the HP category is then calculated as

$$SF_{HP} = \frac{\varepsilon_{HP}^{data}}{\varepsilon_{HP}^{MC}} \quad (7)$$

The scale factor for the LP category is calculated considering that the sum of all the τ_{21} regions must give back the total initial number of events:

$$SF_{LP} = \frac{1 - \varepsilon_{HP}^{data} - \varepsilon_{rej}^{data}}{1 - \varepsilon_{HP}^{MC} - \varepsilon_{rej}^{MC}} \quad (8)$$

517 where ε_{rej} is the fraction of events with $\tau_{21} > 0.75$; for the $t\bar{t}$ control sample considered, it is approxi-
 518 mately 1% and it was assumed to be the same between data and MC. The final scale factors were found
 519 to be $SF_{HP} = 0.93 \pm 0.08$ and $SF_{LP} = 1.10 \pm 0.30$, as reported in Table 6. The errors are statistical in
 520 nature and are mostly driven by the available number of events in the $t\bar{t}$ control region.

521 **6.3 Reconstruction of the heavy resonance and multiple event candidates in an
 522 event**

523 From all the possible combinations of $Z \rightarrow \ell\ell$ and $Z \rightarrow qq$, resonance candidates are constructed.
 524 There is a certain fraction of events when more than one candidate is present in an event after all the

²The methodology used here starts and further develops the strategy used in previous analyses [17, 18, 34, 40, 46, 50].

Category	V-tagging scale factor
1JHP	0.93 ± 0.08
1JLP	1.10 ± 0.30

Table 6: Scale factors for correcting the efficiency of the V-tagging selection in the MC. The scale factors were obtained from the comparison between the V-tagging efficiencies in data and MC for a $t\bar{t}$ -enriched control sample. The uncertainties on the scale factors are used as systematic uncertainties on the signal efficiency.

525 final selection requirements. In the m_{ZZ} range above 400 GeV, the typical multiplicity of candidates
 526 per event is 1.2 in the single jet case and 1.9 in the double jet case. This is predominantly due to more
 527 than one combination of jets satisfying selection requirements. For simplicity of analysis we pick one
 528 unique candidate in each event passing all selection requirements. Priority is given to candidates in the
 529 following order:

- 530 • Single jet, high V-tag purity candidates
- 531 • Single jet, low V-tag purity candidates
- 532 • Double jet candidates

533 In cases where there are more than one candidate in the same category, we choose the one having the
 534 lowest value of the variable:

$$D = (m_{\ell\ell} - M_Z)^2 + (M_{J(J)} - M_Z)^2 \quad (9)$$

535 where the nominal mass of the Z , M_Z , is set to the PDG value of 91.1876. It should be noted how
 536 in the vast majority of cases ($> 99.9\%$) there is only one leptonic Z . The ambiguities arise from
 537 multiple jets passing the selections. A control on the performances of this algorithm has been carried
 538 out verifying the fraction of cases in which the candidate selected by the algorithm matches the Z boson
 539 at the GEN-level ($\Delta R < 0.3$). This fraction is 98.4% for a sample generated with $M = 2000 \text{ GeV}/c^2$. The
 540 high percentage of cases with RECO-GEN matching between the hadronic Z supports the choice of the
 541 proposed arbitration algorithm. We allow to have in the same event two distinct candidates, one in the
 542 sideband and another in the signal region.

543 6.4 Summary of the final event selection

544 Starting from the loosely pre-filtered events as described in Sect. 3, we select the events applying the
 545 final cut selection, including the τ_{21} cut as discussed in Sect. 6.1. We define the final signal region with a
 546 cut in the mass of the hadronic Z candidate, $m_{J(J)}$, around the nominal Z mass, $70 < m_{J(J)} < 110 \text{ GeV}/c^2$.
 547 This cut is important to reduce the Z+jets background which has no genuine mass scale in the hadronic
 548 part of the event. A summary of the kinematic selections applied is presented in Table 7.

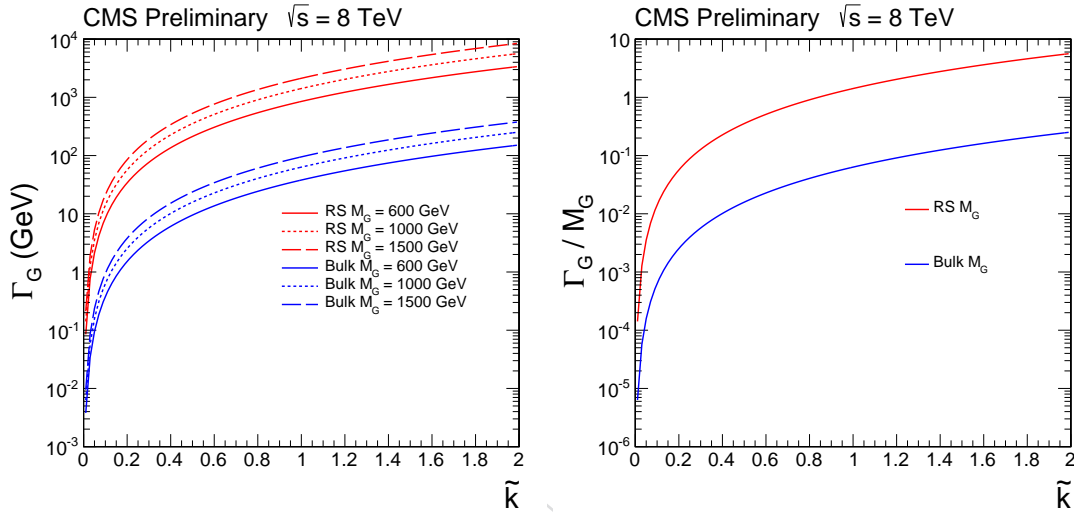
Table 7: Kinematic selections used in the analysis. Trigger and ID cuts are not listed in this table, the reader can refer to the values in Table 5.

Selection	Value	Comments
Lepton selections		
Leading lepton p_T	$p_T > 40 \text{ GeV}$	Same for electrons and muons.
Subleading lepton p_T	$p_T > 40 \text{ GeV}$	For electrons.
Subleading lepton p_T	$p_T > 20 \text{ GeV}$	For muons.
Electron η	$ \eta < 2.5$	
Electron fiducial	$ \eta _{\text{SC}} \text{ out of } [1.4442, 1.566] \text{ range}$	Avoid the ECAL gap.
Muon η	$ \eta < 2.4$	
Jet selections		
Jet p_T	$p_T > 30 \text{ GeV}$	
Jet η	$ \eta < 2.4$	
Boson selections		
m_{LL}	$70 < m_{LL} < 110 \text{ GeV}$	
m_{JJ} (resolved case, signal)	$70 < m_{JJ} < 110 \text{ GeV}$	
m_J (merged case, signal)	$70 < m_J < 110 \text{ GeV}$	
m_{JJ} (resolved case, sideband)	$m_{JJ} \text{ in range } [60, 70] \cup [110, 130] \text{ GeV}$	
m_J (merged case, sideband)	$m_J \text{ in range } [50, 70] \text{ GeV}$	
Leptonic Z p_T	$p_T > 80 \text{ GeV}$	
Hadronic Z p_T	$p_T > 80 \text{ GeV}$	
Diboson selections		
Diboson mass M_{ZZ}	$M_{ZZ} > 180 \text{ GeV}$	
2- to 1-subjettiness ratio (high purity)	$\tau_{21} < 0.50$	
2- to 1-subjettiness ratio (low purity)	$0.50 \leq \tau_{21} < 0.75$	

549 7 Modeling of Signal and Background

550 7.1 Parametrization of the signal shape

551 We used the bulk graviton samples with $\tilde{k} = 0.2$ listed in Sect. 2.1 for modeling the shape of the recon-
 552 structed mass distribution of the signal. Fig. 29 shows the dependence of the width of the graviton line
 553 shape at the parton level. The natural width of the resonance obtained using the chosen value of \tilde{k} is suf-
 554 ficiently small to be neglected when compared to the detector resolution. This makes our modelling of
 555 the detector effects on the signal shape independent of the actual model used for generating the events
 556 and allows us to apply it to a model-independent search.



557 Figure 29: Dependence of the natural width of the graviton as a function of the coupling con-
 558 stant \tilde{k} in the RS1 and Bulk graviton models (left). The same dependence expressed as relative
 559 fraction of the nominal mass is shown in the right-handed plot.

560 The signal distribution varies depending on the Graviton mass hypothesis and the lepton flavor. Several
 561 examples are shown in Figs. 30 and 31. In the final shape analysis of the m_{ZZ} spectrum the discovery po-
 562 tential and exclusion power both depend on an accurate description of the signal shape. MC templates
 563 for the signal are not suitable for this analysis, as the small number of simulated samples necessitates
 564 long range interpolation between different templates. An analytic description of the signal shape, on
 565 the other hand, provides much easier access to the shapes for mass hypotheses not directly covered by
 566 simulation.

567 The m_{ZZ} spectrum of the signal consists of two separate contributions: one in which the jet (or both the
 568 two jets, in the case of resolved topology) of the reconstructed candidate matches the generate quarks
 569 from the resonance decay and another one where one or both jets are not associated to the decay but
 570 originate from initial state radiation, the underlying event or pileup. The matched contribution is fitted
 571 with a double Crystal-Ball function (i.e. a Gaussian core with powerlaw tails on both sides) to describe
 572 the CMS detector resolution. For the values of \tilde{k} considered here, the underlying intrinsic Breit-Wigner
 573 distribution of the Graviton is too narrow to be resolved in this decay channel. The unmatched contri-
 574 bution is significant only in the dijet channel, where it covers a broad range starting at the kinematic
 575 turn-on and slowly falls to high masses with a slope depending on the resonance mass. Crystal-Ball
 576 function was found to give a reasonable description. The two fits are performed independently after
 577 tagging the events as matched/unmatched. The tagging is done by checking if the reconstructed jets
 578 match in ΔR the partons from the Z decay. The estimated unmatched contribution in the monojet chan-
 579 nel is very small ($\lesssim 2\%$). This has to be kept as a very conservative number, as it suffers from signal
 580 contamination due to inefficiencies in the MC matching procedure. For this reason, the unmatched
 581 contribution was neglected in the fits to the shape in the single jet topology.

579 At large masses, $M_1 \geq 1000$ GeV, it has been found that the muon and electron resolutions start to
 580 contribute to the total mass resolution in a visible way. Therefore it has decided to parametrize the mass
 581 shape independently for the electron and muon channel. No significant dependence on the V-tag purity
 582 category has been found.

583 A summary of the natural width and the standard deviation of the gaussian core of the matched part
 584 of the signal is presented for several mass points in Table 8 and 9 for the electron and muon channels,
 585 respectively. For the dijet topology, the numbers are provided only up to $M_1 = 800$ GeV, as for higher
 586 masses the reconstruction efficiency is so low to make impossible a reasonable fit. The parameters for
 587 the signal shape at these mass points, are obtained by interpolating between the fit results to the 15
 588 samples simulated (see Sec. 2.1).

Signal mass [GeV]	Total Natural Width [GeV]	Mean of matched CB [GeV]	Sigma of matched CB [GeV]
monojet category			
600	1.5 (6.0)	609	20
800	2.0 (8.0)	808	28
1000	2.5 (10.0)	1011	31
1600	4.0 (16.0)	1613	41
2000	5.0 (20.0)	2013	50
dijet category			
600	1.5 (6.0)	606	20
800	2.0 (8.0)	813	35
1000	2.5 (10.0)	—	—
1600	4.0 (16.0)	—	—
2000	5.0 (20.0)	—	—

Table 8: Parameters of the signal shape for different mass points at the generator and reconstructed level for the electron channel. The natural width refers to the inclusive decay $G \rightarrow X$ with $\tilde{k} = 0.2$ ($\tilde{k} = 0.5$) and is taken from [51]. The MC samples used for fitting the signal shape parameters are the ones described in Sect. 2.1.

589 The signal reconstruction efficiency in any of the six channels (EE1JHP, MM1JHP, EE1JLP, MM1JLP, EE2J,
 590 MM2J) is defined as the ratio:

$$\varepsilon_{SIG} = \frac{\text{Number of events passing the full selection}}{\text{Total nr. of events generated}} \quad (10)$$

591 where the total number of events generated sums up over all the channels. The events are reweighted
 592 for pileup in the formula above. The efficiency is parameterized as a function of the nominal graviton
 593 mass and is interpolated to all the mass points considered in this search. The efficiency parameterization
 594 is shown in Fig. 32.

595 The signal efficiencies expected with the optimized cuts of Sect.3 and 6.1 are summarized in Table 10
 596 and Figure 32. The efficiencies in this table are calculated normalizing for every category the number
 597 of MC events passing the selection to the total MC statistics of the $G \rightarrow ZZ \rightarrow 2l2q$ ($l = e, \mu$) process.
 598 In the same search in the semi-leptonic WW channel, it has been found that the decrease of efficiency
 599 at high masses in the 1J categories is mostly due to the cut on the pruned mass becoming inefficient,
 600 because the pruned mass loses resolution [45, 46, 52].

Signal mass [GeV]	Total Natural Width [GeV]	Mean of matched CB [GeV]	Sigma of matched CB [GeV]
monojet category			
600	1.5 (6.0)	603	25
800	2.0 (8.0)	807	28
1000	2.5 (10.0)	1007	39
1600	4.0 (16.0)	1604	69
2000	5.0 (20.0)	2005	87
dijet category			
600	1.5 (6.0)	602	25
800	2.0 (8.0)	800	36
1000	2.5 (10.0)	—	—
1600	4.0 (16.0)	—	—
2000	5.0 (20.0)	—	—

Table 9: Parameters of the signal shape for different mass points at the generator and reconstructed level for the muon channel. The natural width refers to the inclusive decay $G \rightarrow X$ with $\tilde{k} = 0.2$ ($\tilde{k} = 0.5$) and is taken from [51]. The MC samples used for fitting the signal shape parameters are the ones described in Sect. 2.1.

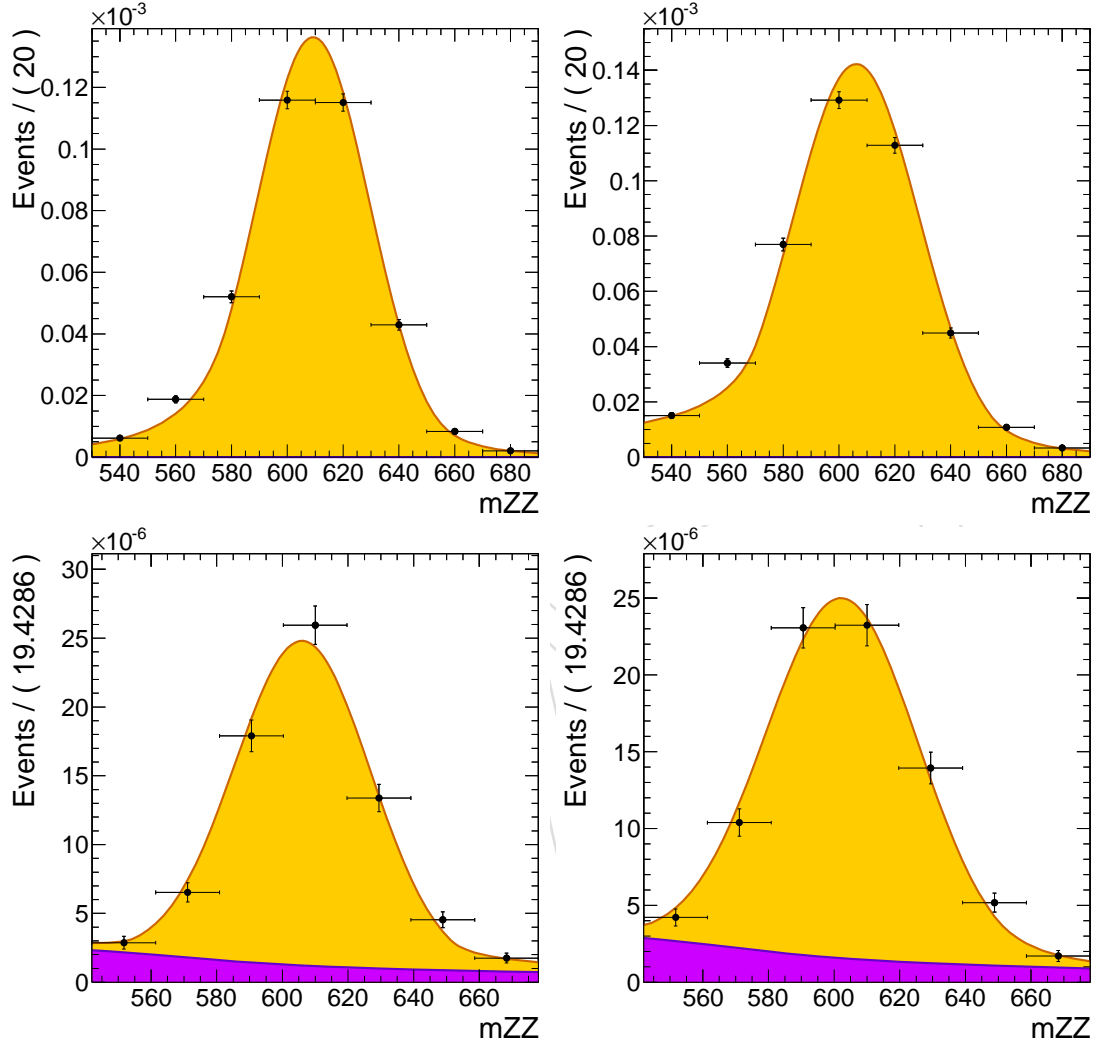


Figure 30: Distribution of the invariant mass, m_{ZZ} , and probability parameterization for MC bulk graviton events with mass $M_1 = 600$ GeV, reconstructed in electron (left) and muon (right) channels. The top plots include only events reconstructed in the single jet category, the bottom plots only events reconstructed in the dijet category. The matched contribution to the pdf is shown in yellow, while the unmatched one is shown in violet.

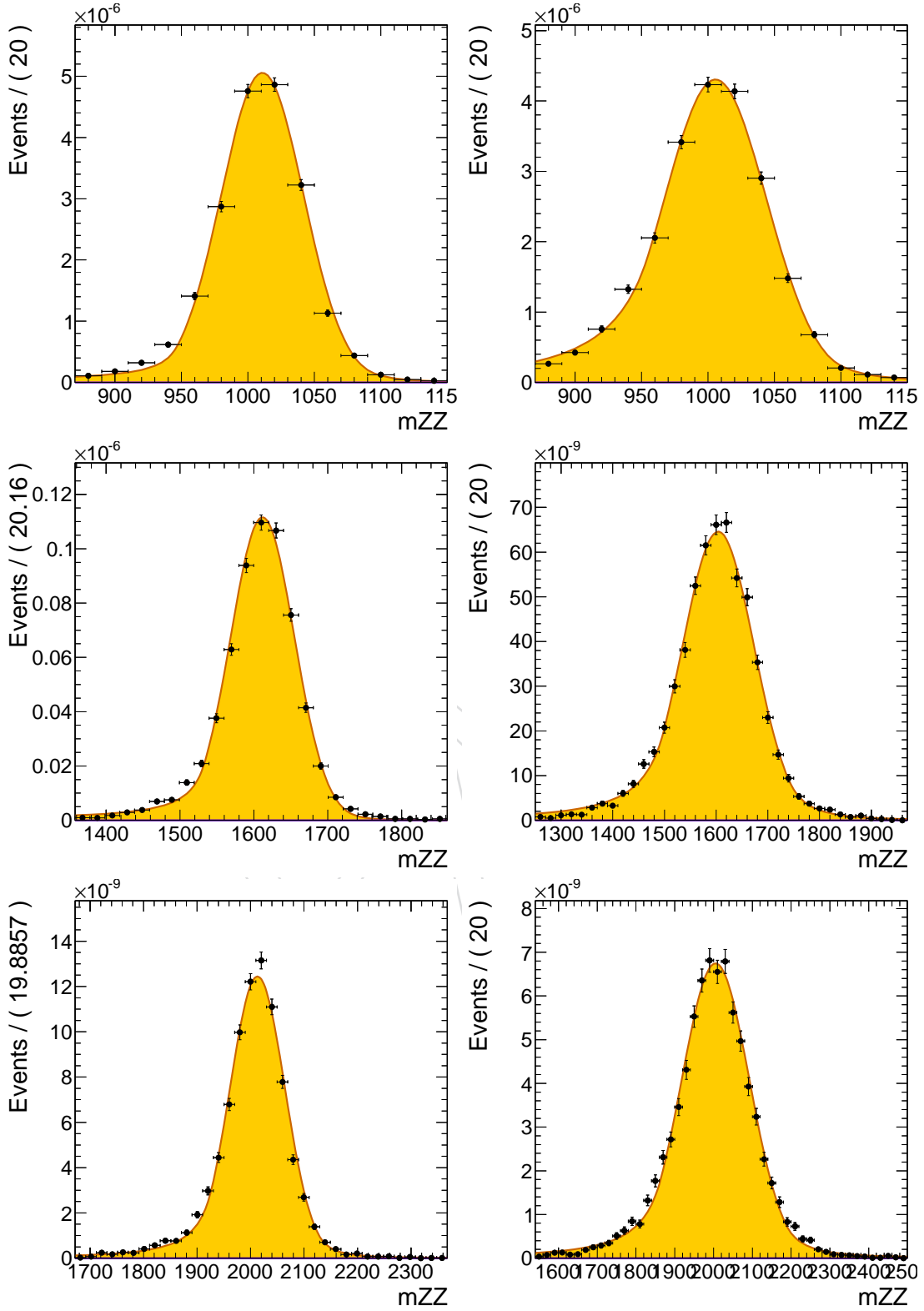


Figure 31: Distribution of the invariant mass, m_{ZZ} , and probability parameterization for MC bulk graviton events with mass $M_1 = 1000$ GeV (top row), $M_1 = 1600$ GeV (top row) and $M_1 = 2000$ GeV (bottom row). Events reconstructed in electron channel are shown in the left column, events reconstructed in the muon channel are shown in the right column. The plots include only events reconstructed in the single jet category.

M_G [GeV]	Signal Efficiency					
	Electron Channel			Muon Channel		
	1JHP	1JLP	2J	1JHP	1JLP	2J
600	0.127	0.017	0.034	0.150	0.023	0.040
700	0.162	0.026	0.017	0.189	0.034	0.021
800	0.190	0.032	0.011	0.210	0.036	0.012
900	0.195	0.035	0.005	0.209	0.041	0.007
1000	0.201	0.037	0.004	0.224	0.041	0.005
1100	0.210	0.041	0.003	0.221	0.041	0.005
1200	0.208	0.043	0.003	0.220	0.045	0.004
1300	0.203	0.044	0.004	0.215	0.045	0.004
1400	0.199	0.044	0.003	0.203	0.045	0.003
1500	0.193	0.046	0.003	0.206	0.043	0.003
1600	0.194	0.047	0.003	0.185	0.045	0.003
1700	0.193	0.043	0.002	0.172	0.049	0.004
1800	0.183	0.045	0.003	0.172	0.047	0.002
1900	0.177	0.048	0.004	0.164	0.047	0.003
2000	0.174	0.049	0.003	0.160	0.045	0.003
2100	0.164	0.051	0.003	0.155	0.046	0.003
2200	0.162	0.049	0.003	0.143	0.048	0.002
2300	0.150	0.050	0.004	0.141	0.047	0.003
2400	0.134	0.050	0.003	0.128	0.046	0.004
2500	0.129	0.050	0.003	0.124	0.050	0.003

Table 10: Expected signal efficiency for single jet high-purity (1JHP), single jet low-purity (1JLP), and double jet (2J) categories for several mass hypothesis.

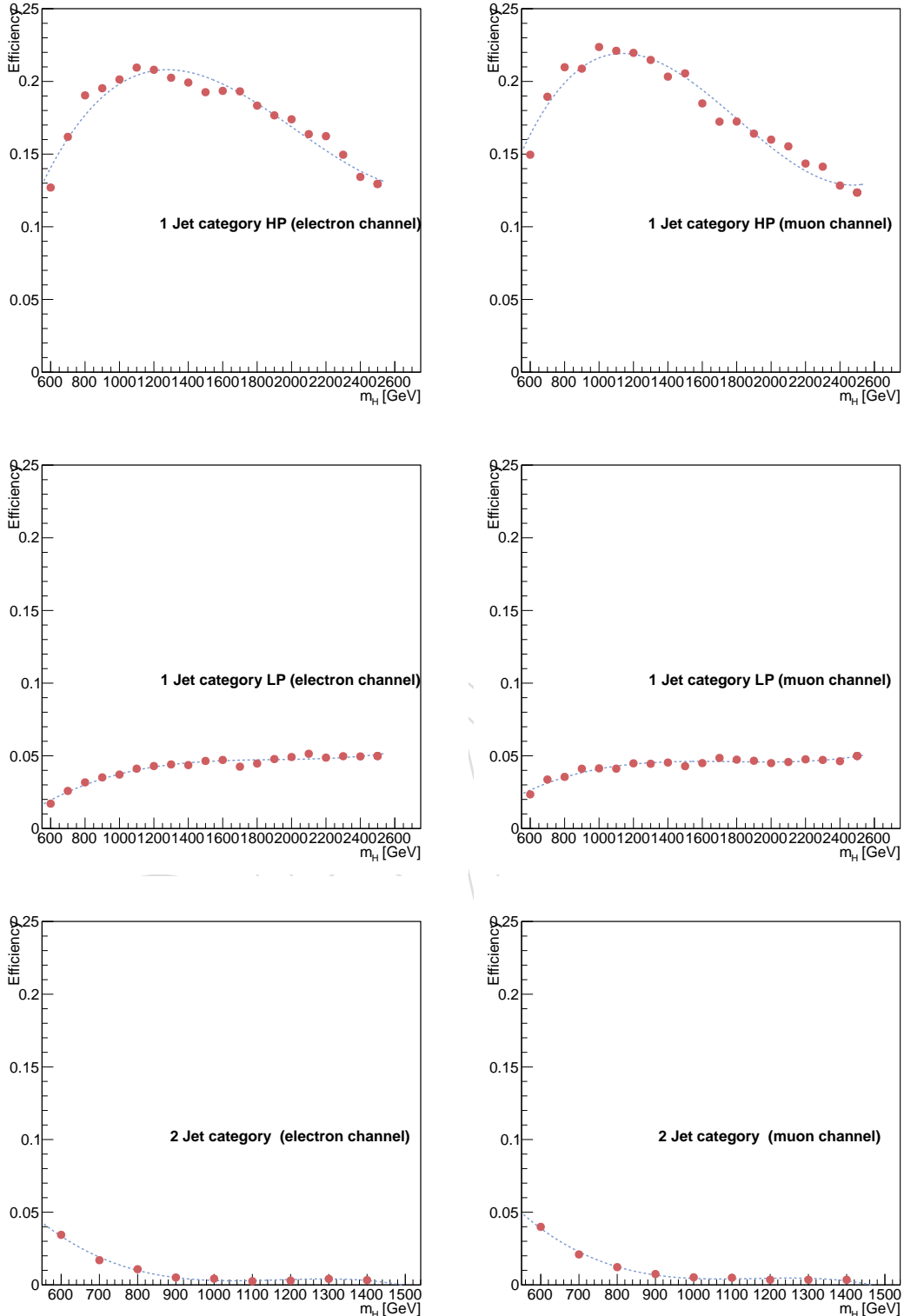


Figure 32: Parameterization of signal efficiency as a function of Graviton mass hypothesis in single jet, high purity category (top), single jet, low purity category (middle), double jet category (bottom) and in the electron (left) and muon (right) channels.

601 7.2 Background estimation from the $M_{J(J)}$ sidebands

602 Despite of the fair description of the event kinematics done by the simulation, we decide to minimize
 603 the dependence on the MC in estimating the SM background and pursue a data-driven strategy.

604 We define a signal region in the mass of the hadronic Z candidate around the nominal Z mass as de-
 605 scribed in Sect.6.4: $70 < M_{J(J)} < 110 \text{ GeV}/c^2$. The sidebands are defined outside the signal region. The
 606 sideband region for the dijet category includes the events which have $60 < M_{JJ} < 130 \text{ GeV}/c^2$, exclud-
 607 ing the signal region. For the single jet topology, the sideband is defined as $50 < M_J < 70 \text{ GeV}/c^2$. The
 608 reason for the difference lies in the different shapes of the distributions of M_J and M_{JJ} as visible in the
 609 left and central columns of Fig.33. In the 1J category, the M_J spectrum falls rapidly and we extend the
 610 sideband region to lower values for gaining more statistics. For the 2J category, the gain is more limited
 611 and we prefer to use events in a control region closer to the signal region in order to minimize the effects
 612 of the extrapolation and have more robust results. For the same reason, we keep the high- M_{JJ} sideband
 613 in the 2J category, but we drop it in the 1J. In the latter case, the gain in terms of statisitcs in the sideband
 614 is limited and there is a potential overlap with an exotic particle decaying to ZH that we prefer to avoid
 615 in view of future analyses.

616 For estimating the dominant Z+jets background ($> 95\%$ over the entire m_{ZZ} range), we exploit the
 617 modeling of the m_{ZZ} mass spectrum in the $M_{J(J)}$ signal region and $M_{J(J)}$ sideband by the Drell-Yan
 618 MC. A ratio $\alpha(m_{ZZ})$ is created from the two. This ratio predicts how sideband data can be scaled to
 619 obtain background prediction in the signal region. The α ratio is shown in Fig. 34 for the 1JHP, 1JLP
 620 and 2J categories. The background expectation $N_{\text{DY}}(m_{ZZ})$ is obtained from distribution of events in the
 621 data sideband $N_{\text{sb}}(m_{ZZ})$ as follows:

$$622 N_{\text{DY}}(m_{ZZ}) = N_{\text{sb}}(m_{ZZ}) \times f_{\text{sb}}^{\text{DY}}(m_{ZZ}) \times \frac{N_{\text{bkg}}^{\text{MC}}(m_{ZZ})}{N_{\text{sb}}^{\text{MC}}(m_{ZZ})} = N_{\text{sb}}(m_{ZZ}) \times f_{\text{sb}}^{\text{DY}} \times \alpha(m_{ZZ}) \quad (11)$$

622 where $f_{\text{sb}}^{\text{DY}}(m_{ZZ})$ is the fraction of DY events in the data sidebands. The advantage of the above ap-
 623 proach is that most systematic uncertainties cancel in the ratios while the remaining factor $\alpha(m_{ZZ})$ re-
 624 flects small kinematic differences between the signal region and sideband, which is mostly independent
 625 from the theoretical prediction of cross-sections. This procedure also provides automatic normalization
 626 of background and makes any needed adjustments to the shape of the m_{ZZ} mass spectrum should there
 627 be any discrepancy. However, we would still like to note that there is a fair agreement between the data
 628 and the MC prediction of the m_{ZZ} and $M_{J(J)}$ distributions after preselection requirements as discussed
 629 in previous sections.

630 The prediction of the minor backgrounds (mostly SM diboson production) is taken directly from the
 631 MC. This is different from what was done in past analyses [16, 48], where minor backgrounds were
 632 treated in the same way as the DY, calculating an overall α ratio. This new strategy is safer at very high
 633 m_{ZZ} because it avoids to require the MC to estimate large extrapolation factors in the not very well-
 634 known tails of the $M_{J(J)}$ distribution. It is also safer not to rely fully on the simulation for quantifying
 635 with high precision the relative ratio of the VV and DY cross sections over a broad range of m_{ZZ} . As
 636 alternative, the estimation of the contribution to the m_{ZZ} spectrum coming from VV is taken directly
 637 from the MC. This procedure, although relying on the MC in a more apparent way, uses the simulation
 638 in a more trusted kinematical region. It is worth to mention that this EWK process is well known and
 639 several other analyses show the reliability of this specific MC [35, 45, 53, 54].

640 For masses $2200 \text{ GeV}/c^2$, the method described above is limited by the total absence of events in the
 641 sideband region (see Fig.33). This allows us to set limits up to $m_{ZZ} = 2000 \text{ GeV}/c^2$, since one must
 642 give some margin able to fully accommodate the signal shape. On the other hand, the presence of
 643 events in the signal region at masses higher than this value would require the ability of estimating the
 644 background up to $2800 - 3000 \text{ GeV}/c^2$. In order to be able to achieve this, it was decided to take the
 645 background prediction straight from the MC (both Madgraph DY+jets and minor backgrounds from
 646 Pythia). The normalization of the prediction of the MC background was scaled up by a factor two,
 647 based on a comparison with the data at lower m_{ZZ} . In order to take into account the limited reliability
 648 of the MC prediction in this range, a large additional systematic uncertainty on the normalization of

the expected background was assigned for $m_{ZZ} = 2000 \text{ GeV}/c^2$. More details on the extension of the background prediction at higher masses are presented in Appendix E.

To estimate the shape of background in data, the events in the sideband region have been rescaled according to the corresponding $\alpha(m_{ZZ})$. These distributions are then fit using either a simple exponential function or a leveled exponential function. the leveled exponential is parametrized as

$$P(m_{ZZ}) = \exp \left[\frac{-(m_{ZZ} - m_0)}{(\sigma + p_0(m_{ZZ} - m_0) + p_1(m_{ZZ} - m_0)^2)} \right] \quad (12)$$

From this functional form, one can see that for the values of the fit parameters $p_0 = p_1 = 0$, one recovers the simple exponential fit. We studied in a quantitative way the quality of the fits and how many free parameters are effectively needed in the fit function for properly describing the background. We performed a F-test, whose results suggest that for the 1JHP and 1JLP categories a simple exponential is able to describe well the m_{ZZ} distribution in the extrapolated sidebands while for the 2J category there is a statistically significant gain in adding one parameter and using a 2-degree leveled expo (i.e., $p_0 \geq 0$ and $p_1 = 0$). However, a bias study indicates that the simple exponential is a too rigid function and can introduce biases in the signal+background fit. A different functional form has been tested in the bias study. A modified power-law with the following parametrization has been study.

$$P(m_{ZZ}) = m_{ZZ}^{(p_0 + p_1 m_{ZZ})} \quad (13)$$

Both the leveled exponential and the modified power law do not introduce any biases. Given their equivalence we decided to use the leveled exponential for all event categories. These studies are discussed in detail in Appendix B (for the F-test) and C.

The fit is always unbinned. The range of the fit (and consequently the range of the search) is different between the various categories. In the 1JHP category, the fit is done on the extrapolated sidebands in the region $[500, 2800] \text{ GeV}/c^2$. In the 1JLP region, shoulders in the m_{ZZ} distribution induced by the kinematic selections make impossible to fit with one simple smooth function at relatively low m_{ZZ} . Since the 1JLP category has a small weight in the final results anyway, it was preferred to favour simplicity and self-consistency of the analysis and restrict the fit to the 1JLP data to a range where one can use safely the same leveled exponential function of 1JHP. This safe range was identified in $[650, 2800] \text{ GeV}/c^2$. For the 2J category, the fit range was defined as $[500, 1400] \text{ GeV}/c^2$. The restricted range for the 2J category is due to the very low signal efficiencies at the masses above that threshold that make this channel not useful in any combination for $M_X > 800 \text{ GeV}/c^2$ (see Section 7.1). The result of the fits are shown in Fig. 35.

The background estimation procedure has been carried out integrating over the two lepton flavours, electron and muon. The motivation for this is to reduce the statistical uncertainties of the procedure. In order to be justified to do this, one must make sure that there are no significant discrepancies in the shape of the m_{ZZ} distribution in the electron and muon channel separately. The results of the unbinned fits to the m_{ZZ} distribution for the two lepton flavours are shown in Fig. 36 and presented in Table 11. A good compatibility between the results is observed, justifying the common background shape estimation. The final statistical analysis described in Section 9 treats the electron and muon channel separately, however. The background normalization is estimated independently for the two cases integrating over the fit range the distribution of the extrapolated sidebands.

Correlations between the two parameters of the leveled exponential can be sizeable and must be taken into account in the statistical treatment. The statistical tools that we use (see Section 9.2) is not able to properly deal with partially correlated parameters. For this reason we redefine the parameters by diagonalizing the covariance matrix in order to decorrelate them. In this procedure, the new parameters are defined in such a way to be centered at zero and with error equal to unity³.

Uncertainties in this procedure result in systematic errors in both normalization and shape parameterization of the m_{ZZ} distributions. The systematic uncertainties on the normalization in the above pro-

³the shift and renormalization of the parameter is a somewhat arbitrary convention present in the diagonalization tool that we use.

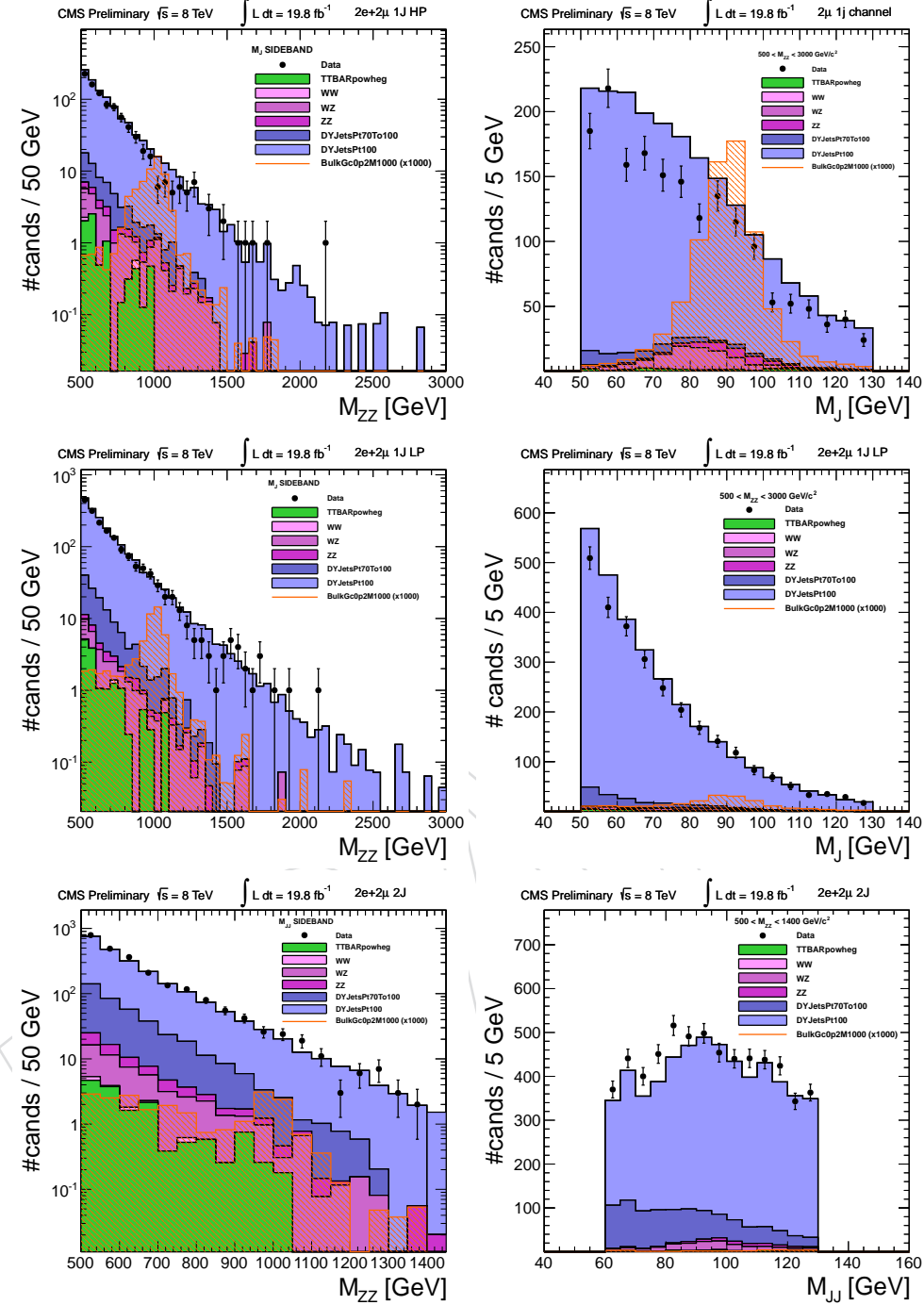


Figure 33: The m_{ZZ} distribution in the sideband range for the 1J and 2J categories. The Z+jets contribution is modeled with Madgraph. The three categories are shown from top to bottom: 1JHP (top), 1JLP (middle), and 2J (bottom). Left: m_{ZZ} distribution in the sideband $m_{J(J)}$ range, log scale. Right column: the $m_{J(J)}$ distribution in the three categories in both the sideband and signal region. All the distributions for the 1JHP and 1JLP category are prepared in the range $500 < m_{ZZ} < 3000$. For the the 2J category, the m_{ZZ} range considered is $500 < m_{ZZ} < 1400$. Points with error bars show data after final selection, histograms show MC prediction with the dominant contributions shown separately.

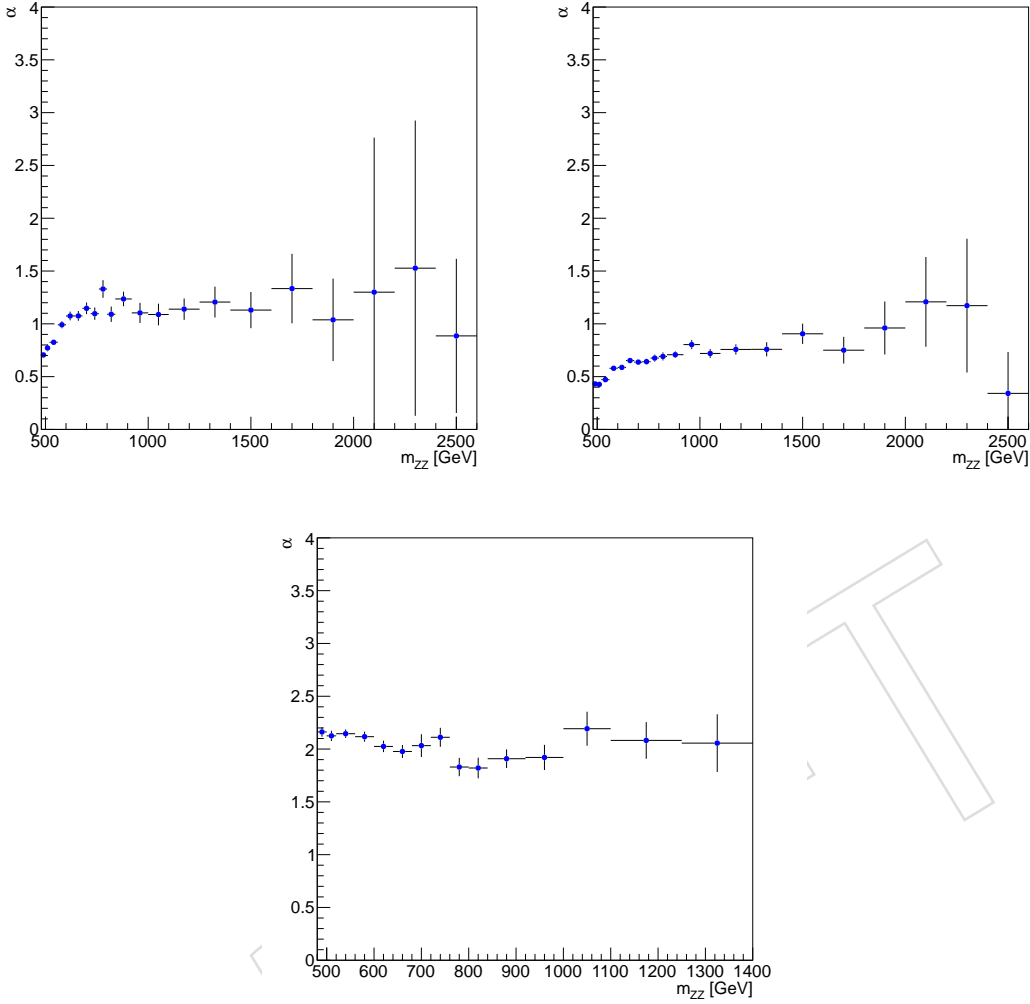


Figure 34: Histograms of $\alpha(m_{ZZ})$ for 1JHP (top left), 1JLP (top right), and 2J (bottom) categories using all relevant MC samples.

692 procedure are statistical in nature and scale with the size of the sideband data and MC samples. Table 12
 693 shows the expected yield from applying the above procedure and observed yield in each of the 6 chan-
 694 nels. The errors on these expectations are on the order of $\sim 3\%$ for the two 1J categories and $\sim 2\%$ for
 695 the 2J category. Errors on the shape parameters are taken from the covariance matrix of the fits to the
 696 extrapolated sideband.

697 In addition to the statistical uncertainties from the number of events in the sidebands of data, there are
 698 statistical uncertainties on the extrapolation factors α due to the limited size of the simulated samples.
 699 These uncertainties are propagated to the the final background parameterization in the following way:
 700 a large number of alternative m_{ZZ} distributions for the MC in both the signal and sideband region are
 701 randomly generated from from the nominal distributions. The random generation was performed toss-
 702 ing the bin contents following a Poissonian statistics. For each of the pseudo-experiments, an alternative
 703 α ratio was prepared from the generated MC distributions. We generated 500 pseudo-experiments in
 704 this way, each with the same data in the sideband but with a different α . The fit to the extrapolated
 705 sidebands is repeated for each of them and the varied extrapolated shape noted.

706 The distribution of the parameters of the fit function derived from these alternative fits is shown in
 707 Figure 37, including the diagonalization procedure, in the case of fits with leveled exponential. The
 708 systematic uncertainty that we assign at the end of this procedure corresponds to the standard devia-

Inverse of the slope of the exponential, σ [GeV]			
	Ele channel	Muon channel	Both channels
1JHP category	205 ± 10	183 ± 8	195 ± 6
1JLP category	222 ± 13	217 ± 11	218 ± 8
2J category	131 ± 5	132 ± 4	132 ± 3

Table 11: Inverse of the fitted slope parameter for different categories and lepton flavours. In all cases, we fit with a simple exponential function parametrized as $y = A \cdot e^{-x/\sigma}$.

	1JHP	1JLP	2J	
observed yield	866	1082	3691	
expected background (data-driven, $m_{J(J)}$)	943 ± 31	1018 ± 25	3818 ± 84	
expected background (MC)	1059 ± 33	1096 ± 33	5517 ± 74	
signal expectation (MC)				
Bulk Graviton ($\tilde{k} = 0.5$)	$M_1 = 800 \text{ GeV}$ $M_1 = 1200 \text{ GeV}$ $M_1 = 2000 \text{ GeV}$	18.1 1.2 0.016	3.1 0.25 0.004	1.4 < 0.05 ≈ 0

Table 12: Observed and expected yields with 19.8 fb^{-1} of data compared to the predictions from the MC samples and from the data-driven background estimation with the m_J -sideband method. The yields are quoted in the range $500 < m_{ZZ} < 2200 \text{ GeV}$ for the 1J category and $500 < m_{ZZ} < 1400 \text{ GeV}$ for the 2J category, integrating over the two lepton flavors. Notice that signal extraction requires further analysis of the m_{ZZ} spectrum exploiting the shapes of the expected signal. The errors on the expected background from MC simulation include only statistical uncertainties.

709 tion of the Gaussian fit to the distributions of the fitted values. The values of these uncertainties are of
 710 the same order of magnitude of the errors coming from the covariance matrix, emphasizing the impor-
 711 tance of including this uncertainty in the final statistical analysis. The fact that the varied parameter
 712 follows a Gaussian distribution indicates that the width of these Gaussian distributions may be added
 713 in quadrature to the data statistical errors to include the uncertainty due to limited MC statistics.

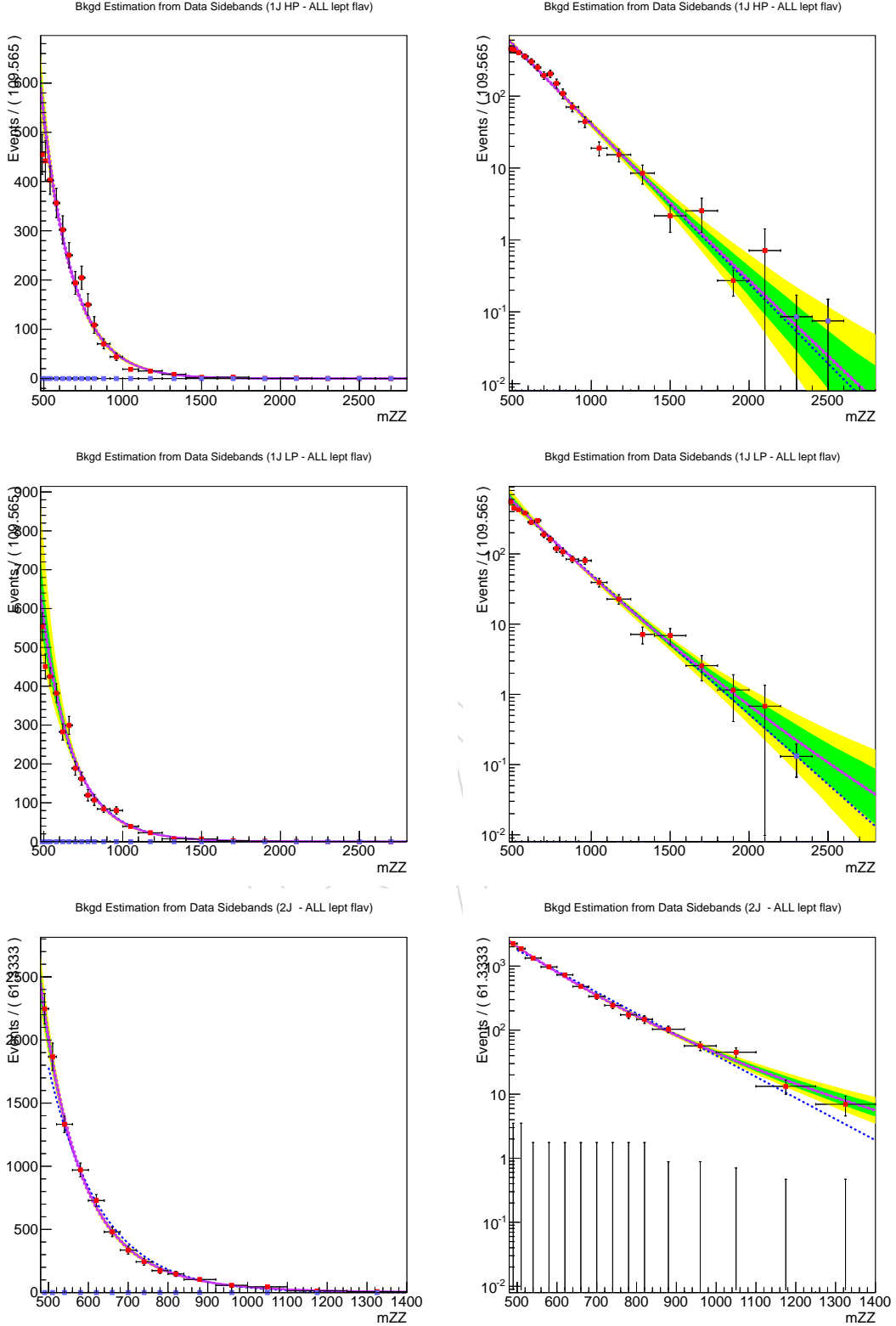


Figure 35: Fits to sideband data rescale to signal region, using 19.5 fb^{-1} lumi. Three event categories are shown from top to bottom: 1JHP, 1JLP, 2J. The distributions sum up over the two lepton flavor considered by the analysis, electron and muons. Left: linear scale, right: log scale. The blue solid line shows the result of the fit with a simple exponential, the violet solid line with a 2-degree leveled exponential. The green and yellow bands show the fit uncertainty coming purely from the covariance matrix of the parameters.

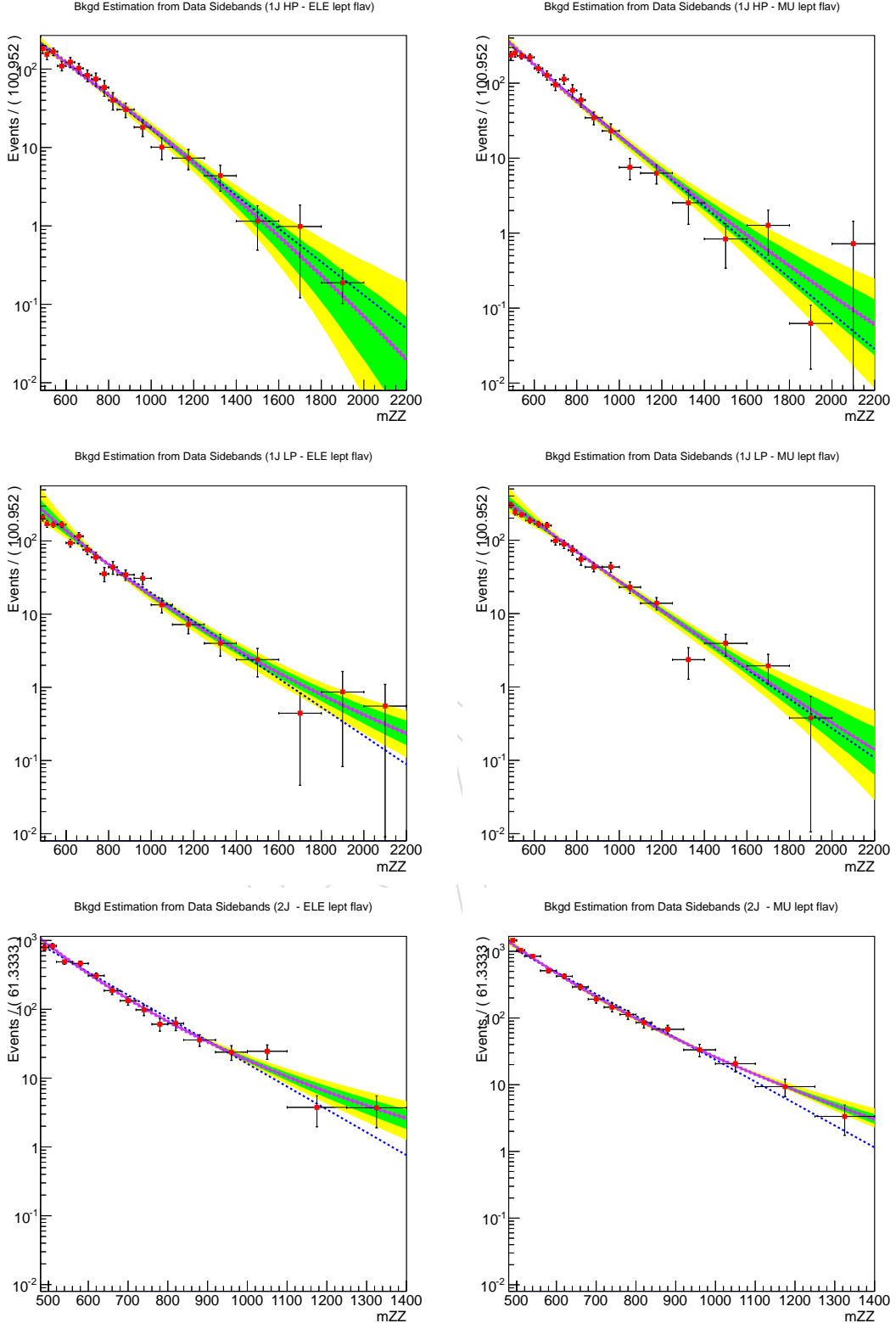


Figure 36: Fits to sideband data rescale to signal region, using 19.5 fb^{-1} lumi. Three event categories are shown from top to bottom: 1JHP, 1JLP, 2J. The left column shows the results of the fit performed on the electron channel the right column presents the same fits to the muon channel.

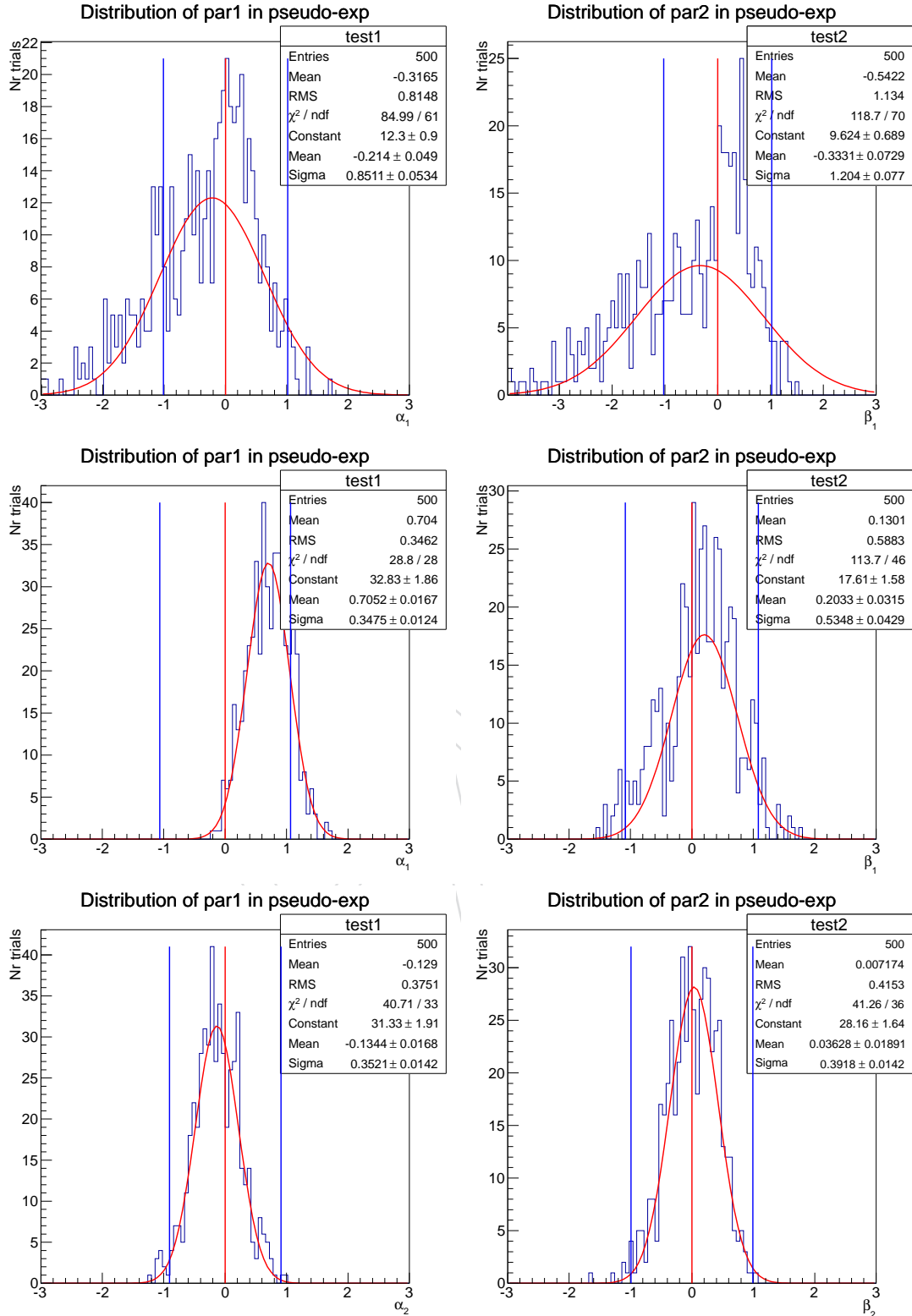


Figure 37: Background shape parameters as derived from the alternative extrapolation factors (black histogram), compared to the nominal values (red line) and the uncertainty on the nominal values calculated from the covariance matrix of the fit (blue lines). The distributions are presented for the 1JHP category (top), the 1JLP category (middle), the 2J category (bottom), respectively.

714 8 Systematic Uncertainties

715 Uncertainty on background is considered separately and is one of the dominant effects on the exclusion
 716 limits. Systematic uncertainties on background are discussed in Section 7.2.

717 Uncertainty on the signal shape parameterization arise from the experimental uncertainty in the CB
 718 resolution function. In general signal shape uncertainties are not the dominant sources of systematics
 719 compared with expected signal yield of several events.

720 The main systematic uncertainties on signal normalization are summarized in Table 13, and are dis-
 721 cussed in more detail below. Lepton and trigger efficiencies are evaluated with a tag-and-probe ap-
 722 proach when one lepton from an inclusive sample of Z decays serves as a tag and efficiency for the
 723 other lepton is calculated. Effects of jet reconstruction are evaluated with variation of the jet energy
 724 and resolution within calibration uncertainties. Effects of pile-up are taken as a difference between re-
 725 construction efficiency with pileup below and above the average expected value, otherwise distributed
 726 according to observed values in data. Uncertainty on the V-tagging has been evaluated within the frame-
 727 work of WW semi-leptonic searches on a $t\bar{t}$ control sample [35, 45, 46]. Uncertainties in the production
 728 mechanism affect both longitudinal momentum of the BSM resonance, due to PDFs, and transverse
 729 momentum, due to QCD initial-state radiation effects. We follow the PDF4LHC recommendation to
 730 estimate uncertainty due to PDF knowledge and calculate uncertainty on signal acceptance. We cannot
 731 evaluate the uncertainty due to the mismodeling of the transverse momentum of the Graviton due to the
 732 lack of suitable higher order calculations. The only uncertainty on the Graviton production cross-section
 733 considered here is the effect of the proton parton densities.

734 8.1 Lepton energy scale, resolution, selection, and trigger

735 The uncertainties on the muon trigger and muon ID efficiencies are estimated with the tag-and-probe
 736 analysis described in Appendix A. The uncertainty on the trigger efficiency depends on the kinematics of
 737 the leptons, but we decided to adopt a flat 3% uncertainty that conservatively covers the variations. With
 738 the same tag-and-probe analysis, we evaluated the uncertainties on the data/MC scale factors applied to
 739 the simulation in order to account for mismodellings in the muon ID. The systematic uncertainty on the
 740 scale factors for muons was found to be 4%. We refer to the appendix for more details on the evaluation
 741 of these systematics. For the electron trigger and ID efficiency, we use the numbers evaluated by other
 742 analyses that developed the boosted electron selection [31] corresponding to a total 3% uncertainty.

743 For the systematics on lepton scale and resolution, we adopt the following sources of systematics:

- 744 • For electrons: we take the energy scale from the official EGM POG recommendations for
 745 HEEP electrons [30] and the energy resolution uncertainties from the W' analysis note [55].
 746 Based on those studies, we assign in the barrel (endcaps) a 0.6% (1.5%) uncertainty on the
 747 overall electron energy scale, and a 1.3% (1.5%) uncertainty on the electron energy resolution.
- 748 • For muons: we take the energy scale and energy resolution from the Muon POG official
 749 recommendations [56], which assign a systematic uncertainty of 0.2% for momentum scale
 750 and 0.6% on p_T resolution for low p_T muons, together with an extra uncertainty on the $1/p_T$
 751 bias of 5% momentum scale for high- p_T ($> 200 \text{ GeV}/c$) muons.

752 For each signal mass point, we redo the standard analysis but changing the momentum assigned of
 753 the leptons in different ways: either shifting their overall energy scale up and down by a value equal
 754 to their energy scale; or smearing their energy scale around its nominal value by multiplying it with
 755 a random number drawn from a Gaussian of unitary mean and variance equal to the square of the
 756 uncertainty on their energy resolution. Those variations are then propagated to the reconstruction of
 757 the BSM resonance, and three different effects are considered:

- 758 • Changes on the reconstruction efficiency: these are estimated by considering the variation of
 759 the number of entries in the reconstructed distribution of m_{ZZ} .
- 760 • Changes on the peak of m_{ZZ} distribution: these are estimated by considering the variation of
 761 the mean in the reconstructed distribution of m_{ZZ} .
- 762 • Changes on the width of m_{ZZ} distribution: these are estimated by considering the variation

763 of the RMS in the reconstructed distribution of m_{ZZ} .

764 Effects due to the uncertainty on the knowledge of the electron scale and resolution were found to have
 765 only a minor impact, always below 1%. Figure 38 shows an example of the procedure for the lepton
 766 energy scale effects in the peak position of the m_{ZZ} distribution.

767 8.2 Jet Energy Scale and Resolution

768 The systematic on the jet energy scale was studied by scaling up and down the jet mass and p_T accord-
 769 ing to the uncertainty associated to the Jet Energy Corrections used. This study was performed only
 770 for the 1JHP and 1JLP categories. In the signal MC events falling in the 1J category, the jet used for
 771 reconstructing the BSM resonance has usually very large p_T , above 300 GeV. The typical scaling factors
 772 applied were of the order of 1%. In Fig.39 we show for one example mass ($M_g=1000$ GeV, $\tilde{k}=0.2$) of the
 773 signal MC, the change in signal efficiency. The change caused by this procedure is always below 1%
 774 and we took this value for all the signal masses (see Fig.41). An additional 2% uncertainty was added

Source	1JHP	1JLP	2J	Comment
Signal normalization uncertainties				
Muon trigger	3%			tag-and-probe study
Muon ID	4%			tag-and-probe study
Muon scale	2%			
Muon resolution	0.5%			
Electrons trigger and ID	$\sim 3\%$			tag-and-probe study
Electron scale	$< 0.1\%$			in progress
Electron resolution	$< 0.1\%$			
Jet energy scale	1%	–		JER uncert. negligible
Pileup	0.5%			
V-tagging	8%	30%	–	from $t\bar{t}$ control sample [46], anti-correlated between categories
Proton PDFs	0.4%			PDF4LHC, acceptance only
Luminosity	4.4%			
Signal shape uncertainties				
μ scale - bias	0.6%			shift on signal mean
μ scale - smearing	1.8%			change on signal RMS
μ resolution - bias	$< 0.1\%$			shift on signal mean
μ resolution - smearing	0.2%			change on signal RMS
e scale - shift on signal mean	0.5%			electron scale uncert.
Jet scale - shift on signal mean	0.5%			JES uncert.
Jet scale - change on signal RMS	2%			JES uncert.
Jet resolution - change on signal mean	$< 0.1\%$			JER uncert.
Jet resolution - change on signal RMS	2%			JER uncert.

Table 13: Summary of systematic uncertainties on signal. Uncertainties on normalization are multiplicative factors. The shape uncertainties affect the parametrization of the core of the m_{ZZ} distribution (see Sect.7). See text for more details.

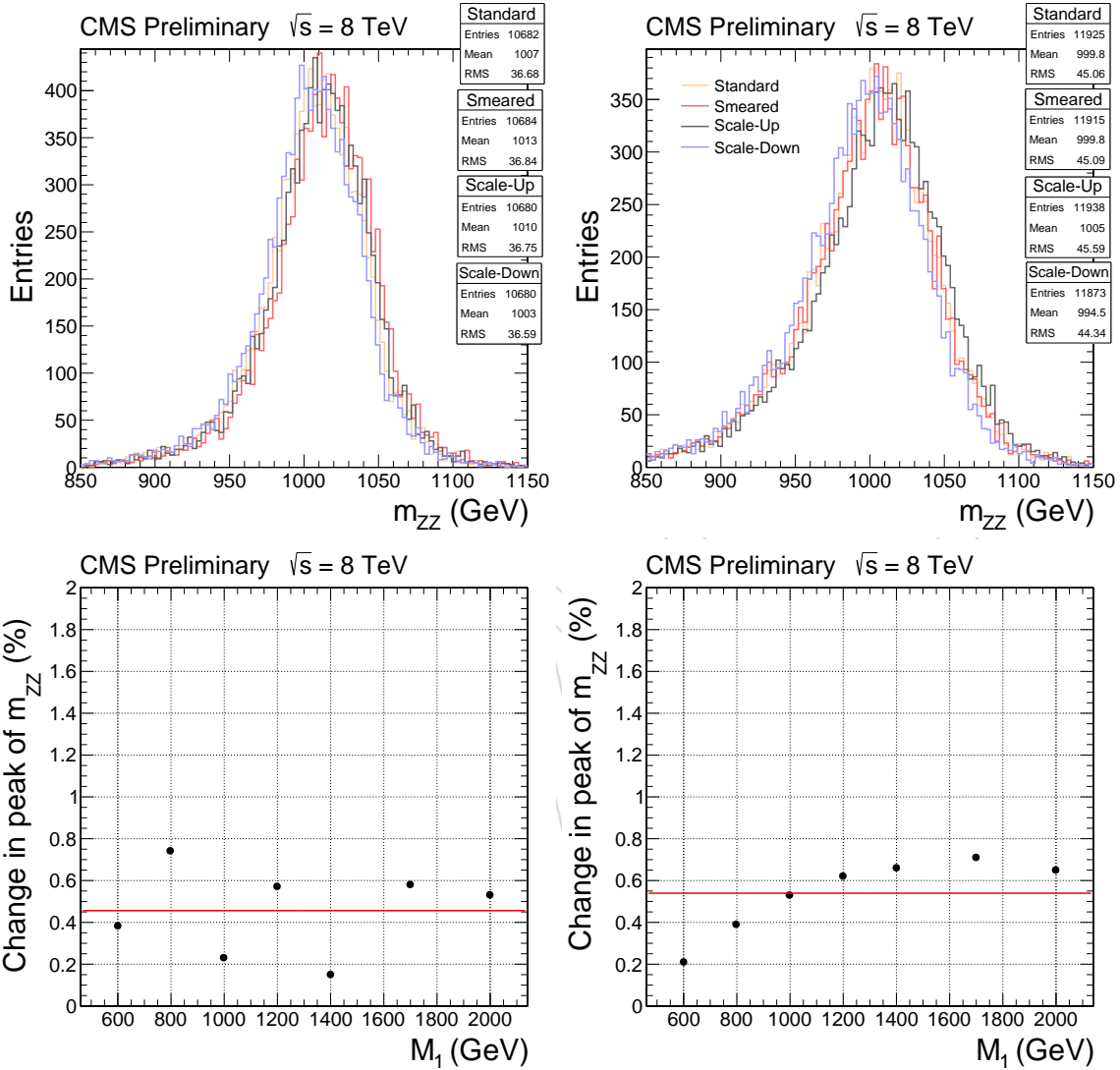


Figure 38: Top: Distributions of m_{ZZ} for a signal sample of Bulk graviton ($M_1 = 1000 \text{ GeV}$, $\tilde{k} = 0.2$) for the nominal (yellow), smeared (red) and shifted Lepton Energy Scale values (black and blue) histograms, in the electron (left) and muon (right) channels. Bottom: Summary of changes in the m_{ZZ} distribution peak position due to systematic effects in the lepton energy scale, for electrons (left) and muons (right). The red lines are there to guide the eye.

775 linearly to it for taking into account the fact that we are applying on the CA8 jets JEC calculated for AK7
 776 jets, following the strategy used in [35]. Associated to the jet energy scale, also the systematic related
 777 to the signal shape is measured, looking on how the mean and the RMS of the m_{ZZ} distribution change
 778 by scaling up and down the jet mass and pT of the same factor. Since no dependence on the resonance
 779 mass has been observed (see Fig.41), a flat 0.5% for the signal peak position and a flat 2% for the signal
 780 width is taken for all the signal masses.

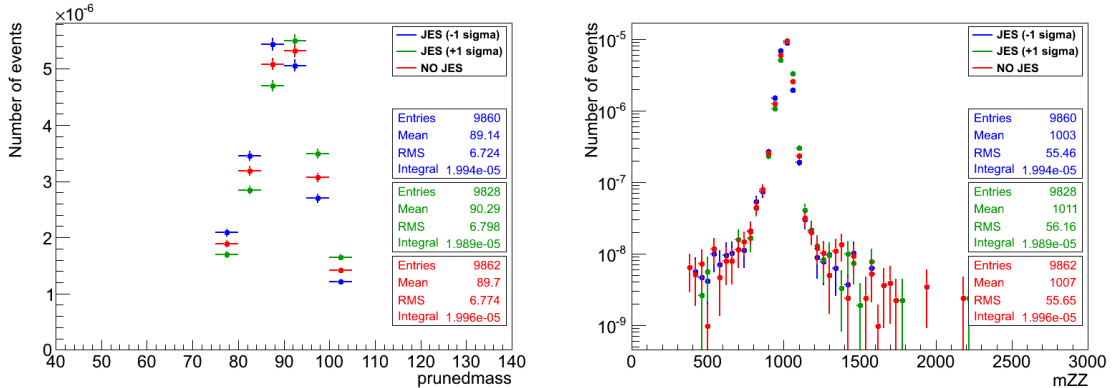


Figure 39: Distributions of the pruned mass (left) and m_{ZZ} (right) for a signal sample of Bulk graviton ($M_1 = 1000 \text{ GeV}$, $\tilde{k} = 0.2$) for the nominal (red markers) and shifted Jet Energy Scale values (blue and green markers).

781 A second source of systematic error related to the jet energy that has been evaluated, is the one associated
 782 to the jet energy resolution. In fact measurements show that the jet energy resolution in data is worse
 783 than in the MC. Also here the study is performed only for the 1JHP and 1JLP categories. To evaluate this
 784 systematic the signal jet energy distribution has been smeared in order to match the jet energy resolution
 785 measured in data. The systematic is given by the difference of the two results with and without the jet
 786 energy resolution smearing. In Fig. 40 we show for one mass ($M_1 = 1000 \text{ GeV}$, $\tilde{k} = 0.2$) of the signal
 787 MC, the change in signal efficiency, given by this smearing. A flat 0.5% error is measured for all the
 788 signal masses. For the change of the signal shape, as expected no peak position movement is observed,
 789 while a flat 2% is measured for the width of the signal distribution. In Fig.41 a summary of the JES and
 790 JER systematics related to the signal efficiency, the signal peak position and the signal width is shown
 791 explicitly for each signal mass.

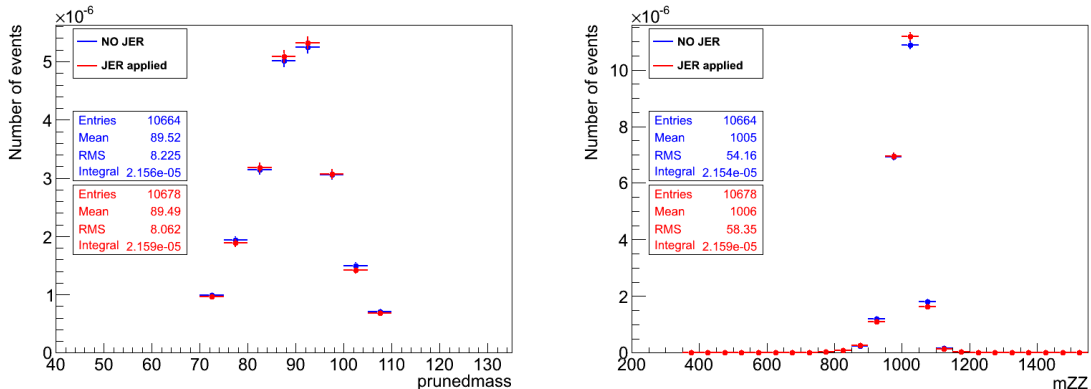


Figure 40: Distributions of the pruned mass (left) and m_{ZZ} (right) for a signal sample of Bulk graviton ($M_1 = 1000 \text{ GeV}$, $\tilde{k} = 0.2$) for the nominal (blue markers) and after the smearing given by the jet energy resolution (red markers).

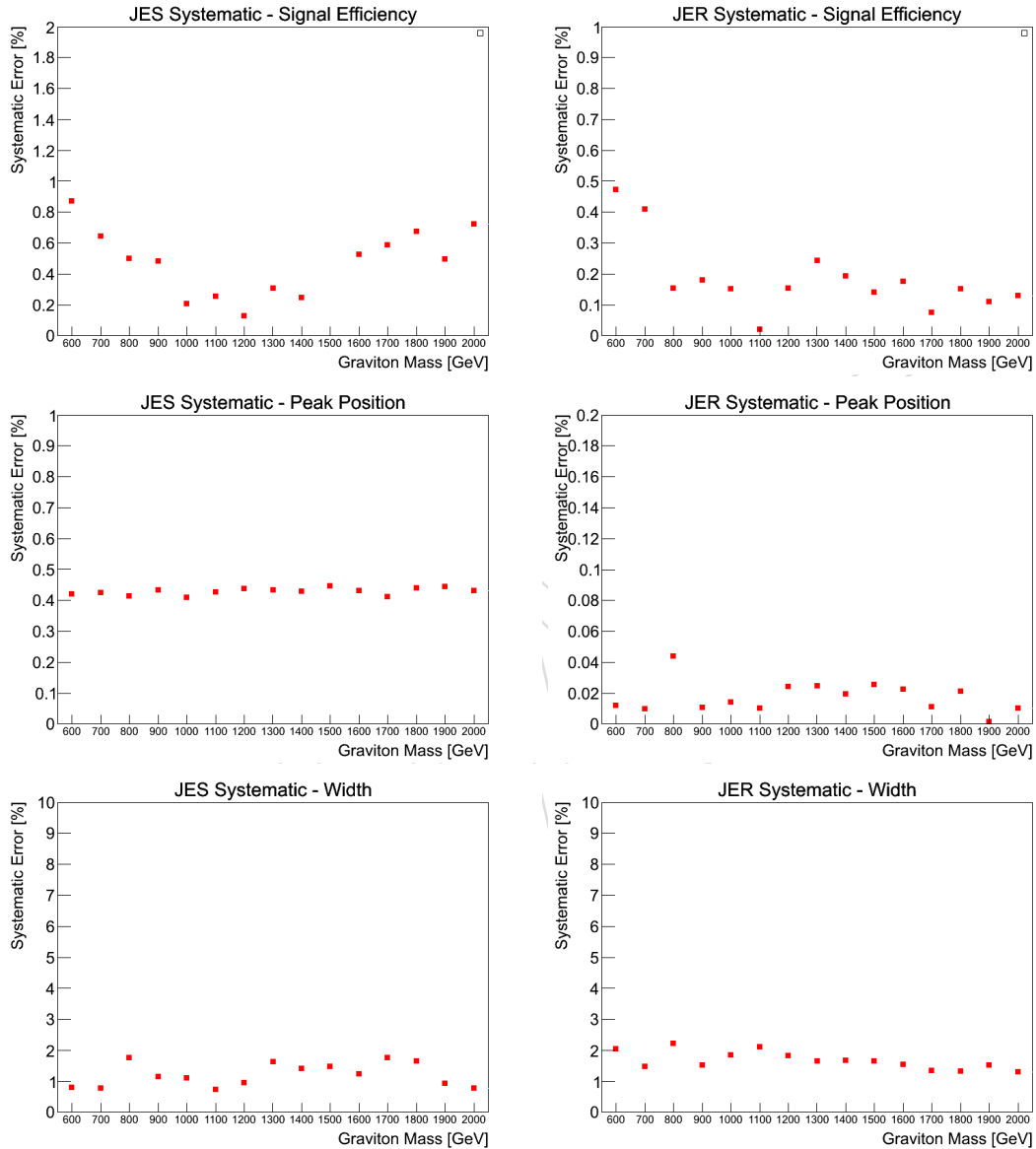


Figure 41: Dependence between systematics due to the Jet Energy Scale (left) and to the Jet Energy Resolution (right) and the resonance mass for the signal efficiency (top), the signal peak position (center) and the signal width (bottom)

792 8.3 Pile-up

793 As described previously, we try to model the effect of the pileup interactions in the event and their
 794 effect on the signal efficiency by adding a number of MinBias events to the simulated signal, at DIGI
 795 level. According to the recommendations of the Physics Validation Group, a variation of $\pm 6\%$ for 2012 in
 796 the number of interactions should be sufficient to cover the uncertainties due to pileup modeling. This
 797 includes an additional $\sim 3\%$ uncertainty to cover all of the modeling and physics aspects of the pileup
 798 simulation that have not been properly studied. Using a central value of 69.4 mb for the total inelastic
 799 cross-section, we vary this number up and down by 6%, redo the analysis and consider the changes in
 800 the signal efficiency. The average effect on the signal efficiency is $\sim 0.5\%$, irrespective of the resonance
 801 mass.

802 8.4 V-tagging and jet substructure

803 Mismodelings in the MC can bias the efficiency of the V-tagging selections described in Section 4.2 and
 804 6.1. An example of this is the τ_{21} distribution shown in Fig.22. The discrepancy between data and
 805 MC suggests that the efficiency of this cut for the MC signal samples - eventually used in the statistical
 806 analysis of the data - might be mis-estimated. In Sect.6.2, a procedure for measuring from the data
 807 appropriate correction factors to the signal efficiency has been described. The final scale factors were
 808 found to be $SF_{HP} = 0.93 \pm 0.08$ and $SF_{LP} = 1.10 \pm 0.30$. The errors on the scaling factors are assigned
 809 as systematic uncertainties of the procedure. Since the analysis does not really cut on τ_{21} but rather
 810 categorizes the events according to it, the uncertainties on the V-tagging scaling factors will reflect on
 811 an uncertainty on the exact migrations between the low and high purity category. For this reason, this
 812 systematic uncertainty was treated as fully anti-correlated between the categories.

813 8.5 Production mechanism

814 The uncertainty of the proton parton distribution functions (PPDFs) introduces a systematic error on
 815 the kinematics of the final state and eventually on the signal acceptance. In particular, the rapidity of
 816 the BSM resonance can be affected by the choice of the PPDFs. This effect was studied following the
 817 PDF4LHC recommendations [57, 58] and using two PPDFs alternative to CTEQ6: MSTW and NNPDF.
 818 We use the standard CMSSW modules PdfWeightProducer and PdfSystematicsAnalyzer. The
 819 effects on the signal acceptance are of the order of 0.4%, irrespective of the resonance mass.

820 8.6 Luminosity uncertainty

821 The latest recommendation is the uncertainty on LHC luminosity of 4.4%.

822 9 Statistical Interpretation of Results

823 9.1 Comparison between data and background prediction in the signal region

824 The m_{ZZ} distribution of the selected events after all the event selections is illustrated in Fig. 42. The
 825 observed distribution is presented for the three event categories and the two leptonic decay channels,
 826 together with the predicted background parametrization. The background distribution is parameterized
 827 with an exponential function and is extracted from data via extrapolation from the $m_{J(J)} -$ sideband. De-
 828 tailed discussion of application of the background determination technique to data is given in Section 7.
 829 The final statistical interpretation will analyze the m_{ZZ} distributions in order to assess any significant
 830 deviation from the SM background.

Event category	# expected Signal evts	#exp bkgd evts	# obs evts	exp UL [fb] (no syst.)	exp UL [fb] (with syst.)	obs UL [fb] (no syst.)	obs UL [fb] (with syst.)
ELE, 1JHP	0.059	398.1	363	—	—	—	—
ELE, 1LP	0.014	419.4	438	—	—	—	—
ELE, 2J	—	1577.2	1458	—	—	—	—
MU, 1JHP	0.061	545.4	503	—	—	—	—
MU, 1LP	0.015	598.3	644	—	—	—	—
MU, 2J	—	2240.9	2233	—	—	—	—
combined				9.5	8.9	8.6	9.1

Table 14: The number of expected signal and background events (without uncertainties)and the observed number of events in the range [500, 2200] GeV/c^2 for the 1JHP and 1JLP categories and in the range [500, 1400] GeV/c^2 for the 2J. The last four columns shows the expected and observed limits with the unbinned shape analysis and the Asymptotic CL_s method calculated for a nominal mass $M_1 = 1600 \text{ GeV}$. Results are separated between three categories and lepton flavour. The theoretical cross section predicted at LO for a Bulk Graviton decaying to ZZ is 0.171 fb ($M = 1600 \text{ GeV}/c^2$, $\tilde{k} = 0.5$).

831 It should be noticed how the 2J category is characterized by very low efficiencies and expected yields
 832 and the highest expected background. Its contribution to the total sensitivity is going to be negligible
 833 and for simplicity we decide to omit it from the final statistical analysis. The good agreement between
 834 the observed data and the predicted background further increases our confidence in our capability to
 835 control the SM background.

836 9.2 Extraction of the upper limit

837 Based on the expected normalization and shape of the m_{ZZ} distribution for signal and background, we
 838 perform an unbinned statistical analysis of the data using the Higgs combination tool [59]. We used
 839 the asymptotic approximation [60] of the LHC CL_s method [61, 62]. A comparison to the modified fre-
 840 quentist prescription (the CL_s method) has been carried out for few mass points and the Asymptotic
 841 observed and central expected limits were found in agreement with CL_s within 5%. Systematic un-
 842 certainties are treated as nuisance parameters and profiled in the statistical interpretation. The shape
 843 analysis that we pursued studied simultaneously the four event categories considered (1JHP and 1JLP
 844 in the electron and muon channel separately) using shapes and normalization predicted for the signal
 845 and background as described in Sections 2.1 and 7. We tested 29 different mass hypotheses of the Bulk
 846 graviton model separated scanning the mass range $m_{ZZ} \in [600, 2000] \text{ GeV}$ at regular steps of 50 GeV.
 847 This choice covers the mass range where previous limits are weaker, focusing on the interesting region
 848 around the TeV scale. For signal mass points where there was no generated MC sample, we estimated
 849 the signal shape and efficiency interpolating the corresponding quantities from the neighbouring mass
 850 points.

851 Fig. 43 shows the final 95% exclusion limit on the cross section of the process $pp \rightarrow G^* \rightarrow ZZ$ com-
 852 bining the four event categories. For comparison, the production cross sections times branching ratio
 853 of $G^* \rightarrow ZZ$ are presented for the benchmark Bulk graviton model [19] with values of the coupling
 854 strength $\tilde{k} = k/M_{Pl}$ equal to 0.2 and 0.5. The upper limits in Figure 43 allow us to exclude at the

855 95% C.L. bulk gravitons with $M_1 < 710 \text{ GeV}/c^2$ for $\tilde{k} = 0.5$, while the expected limit for the same
856 value of \tilde{k} is $730 \text{ GeV}/c^2$. In order to assess quantitatively the significance of the excesses observed in
857 the m_{ZZ} distributions, one can study the p-value as a function of the mass. The p-value is defined as
858 the probability for the background-only hypothesis to fluctuate by the same amount (or more) of the ob-
859 served data. Low p-values indicate large incompatibilities with the background-only hypothesis. The
860 local p-values of the observation are presented in Fig. 44. The most significant excess is reported to have
861 a significance of approximately 2σ and locates at the highest end of the search, at $m_{ZZ} \sim 2450 \text{ GeV}/c^2$.
862 A similar excess, just slightly less significant is visible at $m_{ZZ} \sim 1750 \text{ GeV}/c^2$.

863 Figs. 45 and 46 show the same limits and significance splitting the events in two categories, the high-
864 purity and the low-purity, respectively. Electron and muon channel were combined in this exercise. One
865 can appreciate how the sensitivity of the HP category is the dominant one, the low-purity contributing
866 only marginally.

867 A similar exercise is done breaking down the events by their lepton flavor and combining the LP and
868 HP categories. The results are shown in Figs. 47 and 48. The two lepton flavor have roughly the same
869 sensitivity.



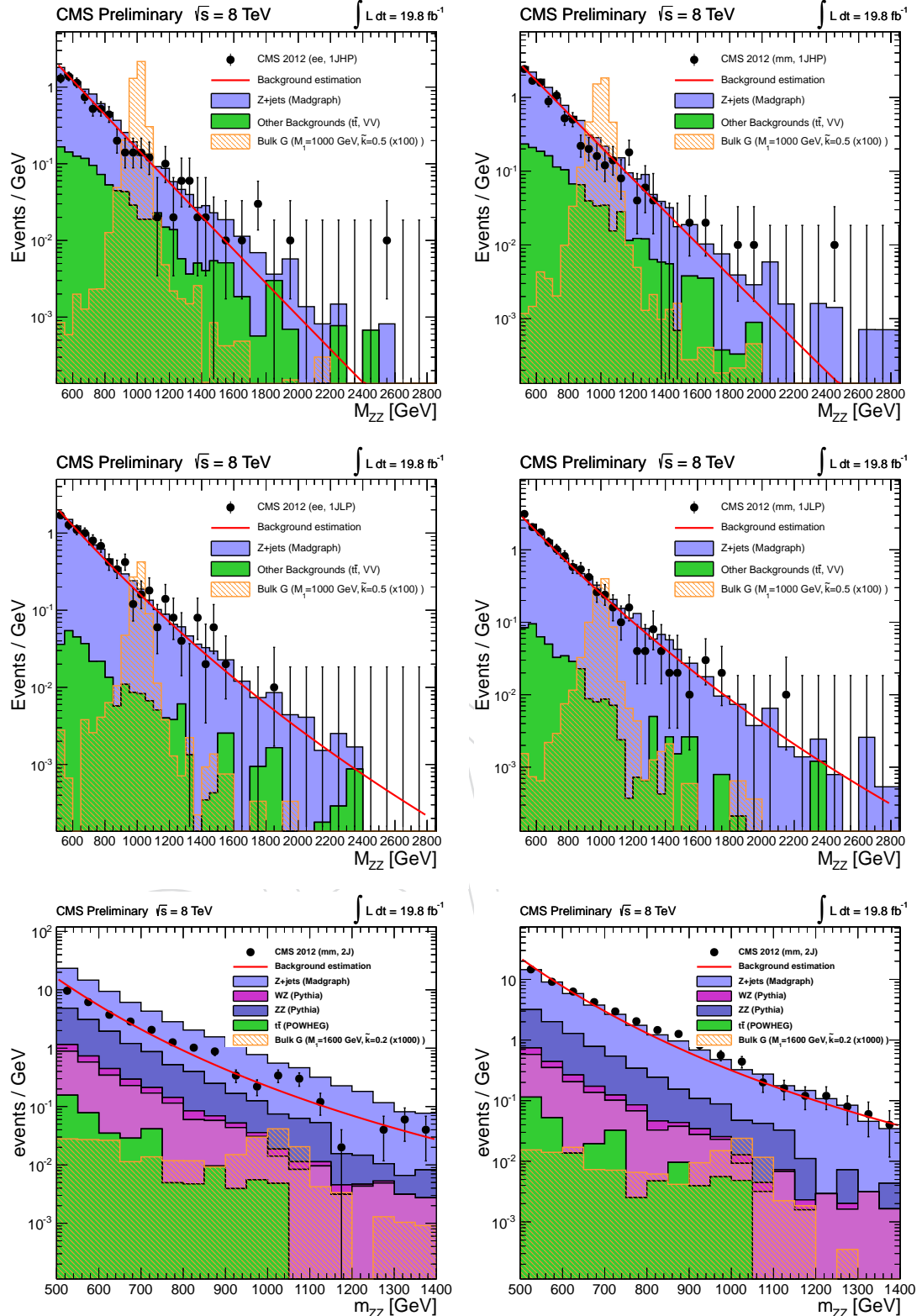


Figure 42: The m_{ZZ} invariant mass distribution after final selection in three categories: 1JHP (top), 1JLP (middle), 2J (bottom). The two channels $2e2q$ and $2\mu2q$ are presented separately on the left and on the right, respectively. Points with error bars show distributions of data, solid histograms depict the background expectation from simulated events with the different components illustrated. Also shown is a hypothetical Bulk Graviton signal with mass of 1600 GeV and $\tilde{k} = 0.50$. The solid curved line shows the central value of the prediction of background from the sideband extrapolation procedure.

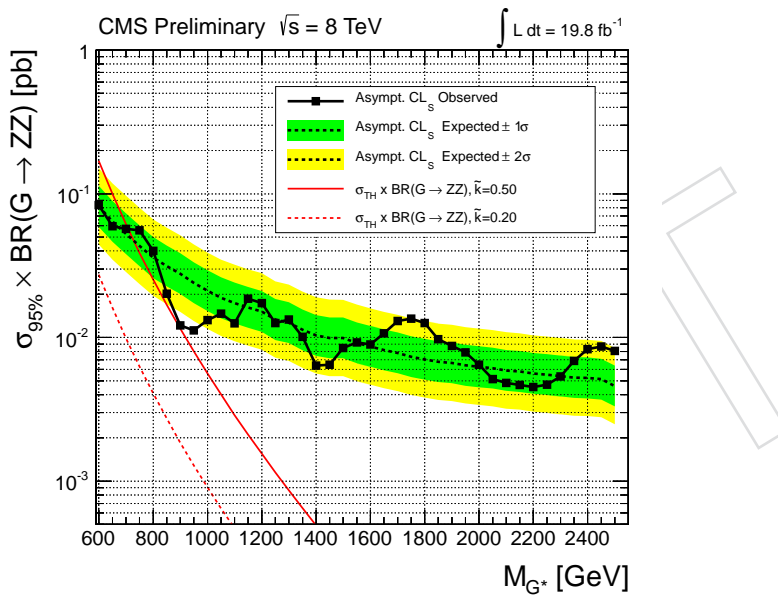


Figure 43: Observed (dashed) and expected (solid) 95% CL upper limit on the product of the graviton production cross section and the branching fraction of $G^* \rightarrow ZZ$ using 19.8 fb^{-1} of data. The limit is obtained with the Asymptotic CL_s technique. For the calculation of this limit, the technique described in Sect.7.2 for estimating the background has been used. The 68% and 95% ranges of expectation are also shown with green and yellow bands. The expected product of the Bulk graviton production cross section and the branching fraction is shown as a red solid (dashed) curve for $\tilde{k} = 0.2$ ($\tilde{k} = 0.5$).

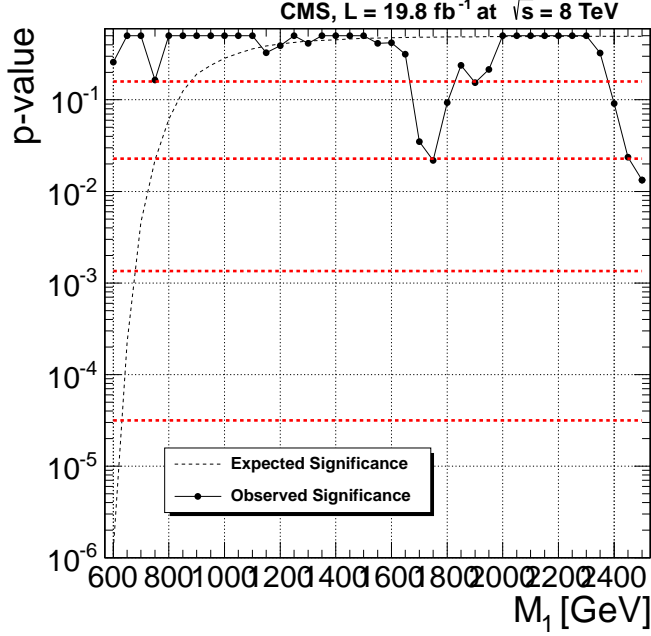


Figure 44: Observed p-values as a function of the nominal signal mass (black dots and solid black line) using 19.8 fb^{-1} of data. The expected p-value in presence of a Bulk graviton ($\tilde{k} = 0.5$) is shown by the dashed line. Conversions of the p-value to number of standard deviations of a two-tail Gaussian are drawn as dashed horizontal red lines.

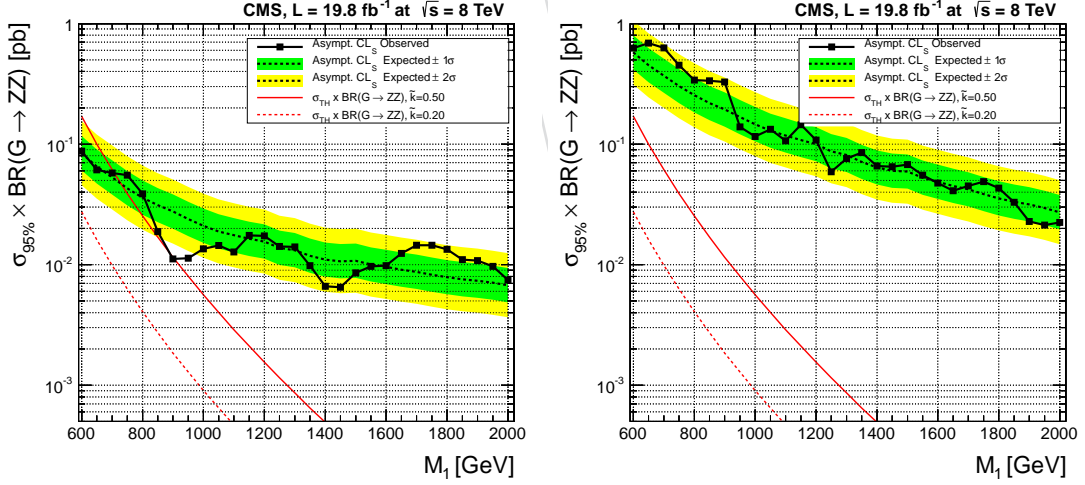


Figure 45: Observed (dashed) and expected (solid) 95% CL upper limit on the product of the graviton production cross section and the branching fraction of $G^* \rightarrow ZZ$ using 19.8 fb^{-1} of data. The limit is obtained with the Asymptotic CL_s technique. The 68% and 95% ranges of expectation are also shown with green and yellow bands. The expected product of the Bulk graviton production cross section and the branching fraction is shown as a red solid (dashed) curve for $\tilde{k} = 0.2$ ($\tilde{k} = 0.5$). The left-hand panel presents the limit using only the High-Purity category, the right-hand panel uses only the Low-Purity category.

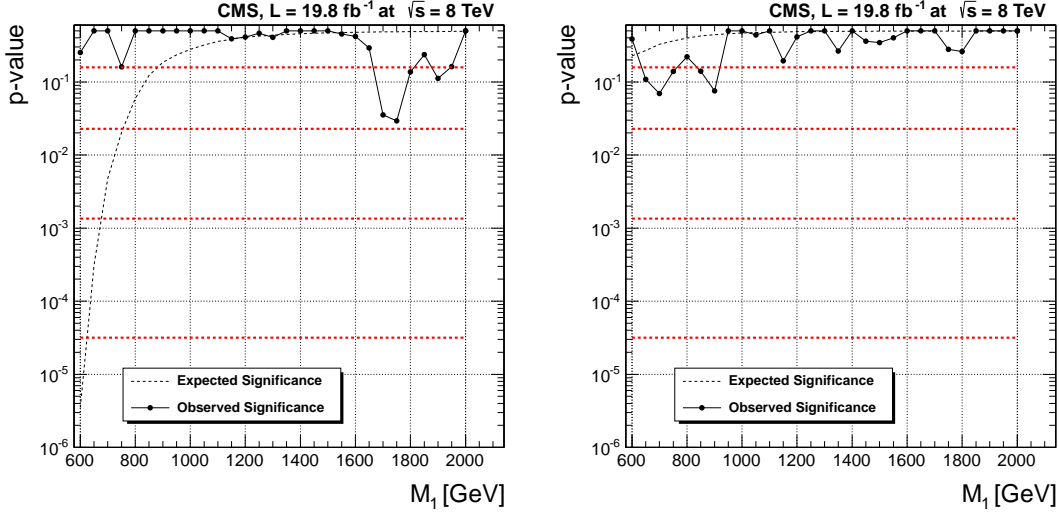


Figure 46: Observed p-values as a function of the nominal signal mass (black dots and solid black line) using 19.8 fb^{-1} of data presented individually for the categories 1J High-Purity (left) and 1J Low-Purity (right). More details on the figure in the caption of Fig.44.

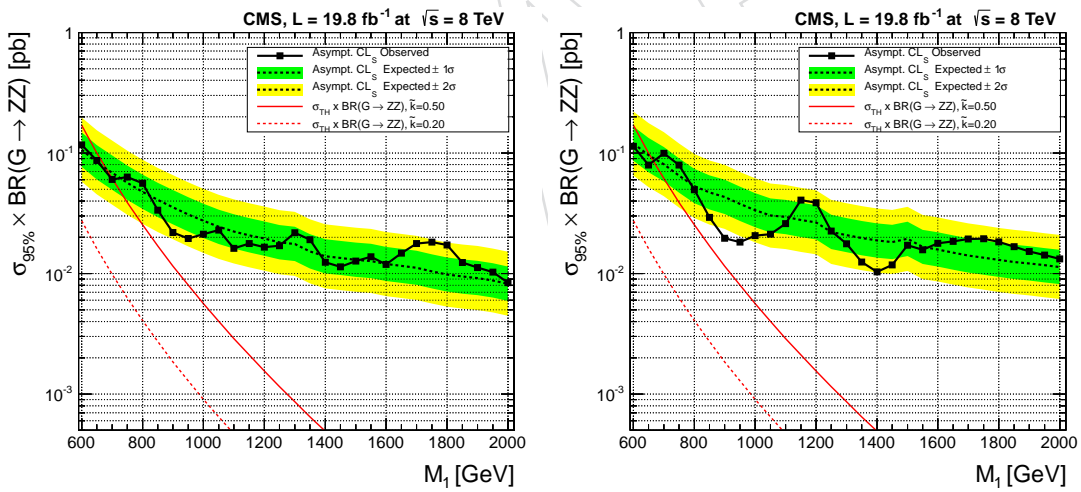


Figure 47: Observed (dashed) and expected (solid) 95% CL upper limit on the product of the graviton production cross section and the branching fraction of $G^* \rightarrow ZZ$ using 19.8 fb^{-1} of data. The limit is obtained with the Asymptotic CL_s technique. The 68% and 95% ranges of expectation are also shown with green and yellow bands. The expected product of the Bulk graviton production cross section and the branching fraction is shown as a red solid (dashed) curve for $\tilde{k} = 0.2$ ($\tilde{k} = 0.5$). The left-hand panel presents the limit using only the electron decay channel, the right-hand panel uses only the muon decay channel, combining the low- and high-purity categories.

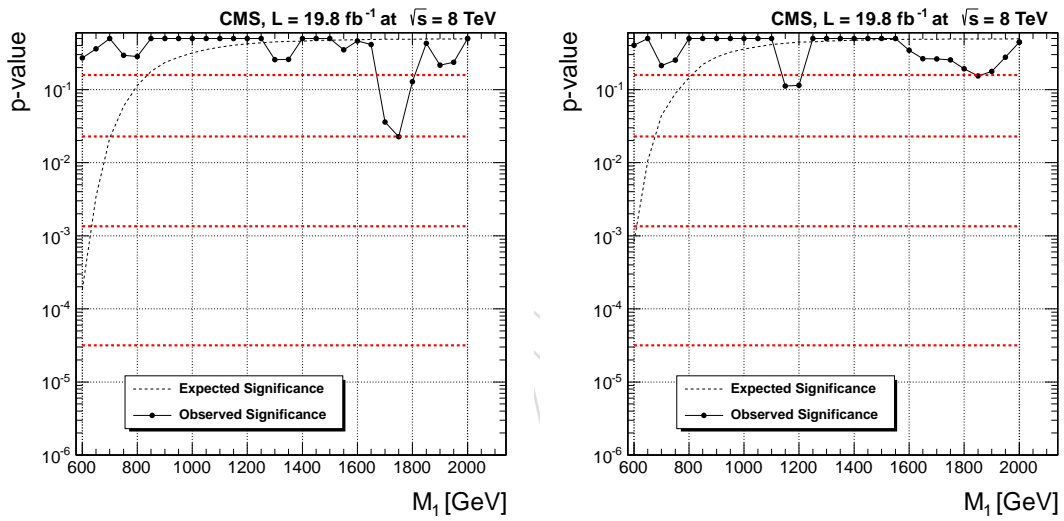


Figure 48: Observed p-values as a function of the nominal signal mass (black dots and solid black line) using 19.8 fb^{-1} of data presented individually for the electron channel (left) and the muon channel (right). More details on the figure in the caption of Fig.44.

870 10 Summary and Conclusions

871 Gravitons decaying to $ZZ \rightarrow 2\ell 2q$ are searched exploiting jet substructure techniques for retaining high
872 efficiency even when the hadronic Z is very boosted. A categorization based on the number of jets used
873 for constructing the $Z \rightarrow qq$ candidate and the value of a kinematic quantity sensitive to the substructure
874 inside the jet is adopted in order to enhance the sensitivity of the search. A detailed MC simulation is
875 used for modeling the main background channels as well a specific benchmark model for the signal. A
876 data-driven technique is used for estimating the expected background in the signal region. A precise
877 assessment of the systematic uncertainties, including the sensitivity to the pile-up, is performed. No
878 excess above the expected background is found. Bulk gravitons with a coupling strength of $\tilde{k} = 0.5$ are
879 excluded at 95% confidence level up to a mass, $M_1 < 710 \text{ GeV}/c^2$. This result represents a significant
880 improvement respect to previous results thanks to the increased luminosity, centre-of-mass energy of
881 the pp collisions and improved analysis techniques.

DRAFT

882 A Study of trigger and reconstruction efficiencies for muons

883 As explained in the Section 3.3 we consider a modified selection for muons in order to deal with the
 884 characteristic small distance (in general $\Delta R < 0.5$) in the plane $\eta \times \phi$ between two muons from the decay
 885 of a boosted Z gauge boson. The selections that we consider are the following:

- 886 • HighPT Identification with a Global Muon (Global Muon ID)
 - 887 • muon identified as a GlobalMuon
 - 888 • number of muon hits larger than zero
 - 889 • number of matched muon stations larger than one
 - 890 • transversal impact parameter dB smaller than 0.2 cm
 - 891 • longitudinal impact parameter dZ smaller than 0.5 cm
 - 892 • number of pixel hits larger than zero
 - 893 • number of tracker layers with hits larger than five
 - 894 • SigmaPtOverPt smaller than 0.3
- 895 • HighPT Identification with a Tracker Muon (Tracker Muon ID)
 - 896 • muon identified as a TrackerMuon
 - 897 • number of matched muon stations larger than one
 - 898 • transversal impact parameter dB smaller than 0.2 cm
 - 899 • longitudinal impact parameter dZ smaller than 0.5 cm
 - 900 • number of pixel hits larger than zero
 - 901 • number of tracker layers with hits larger than five
 - 902 • SigmaPtOverPt smaller than 0.3

903 In addition to these criteria we consider a modified tracker-based isolation with removal of the other
 904 muon. These dimuon events are required as well to pass the double muon trigger: HLT-Mu22TkMu8.

905 Because we have a modified selection, the global calculations from Muon POG are not applicable in our
 906 case, then we present a dedicated study of muons efficiencies with the Tag and Probe technique using
 907 the officially supported package in “PhysicsTools/TagAndProbe” [63]. The main idea of this method is
 908 to use a known resonance, in the case a Z boson, in order to select the pair candidates, and this feature
 909 combined with a choose of a candidate with a very good selection requirement (Tag candidate), ensures
 910 that the other particle of the pair (Probe candidate) has a very good chance to be the aimed candidate
 911 (for example, a muon), and then we calculate the efficiency of this candidate to pass a given selection.
 912 We use this method to calculate the efficiencies in the data and comparing with Drell-Yan events we
 913 obtain scale factors to correct our monte carlo.

914 A.1 Samples

915 For these studies in general we work with Single Muon PD considering the ReReco 2012 ABCD runs and
 916 for the Monte Carlo we use a Drell-Yan sample as showed in Tab. 15. For part of the trigger efficiency
 917 calculations we used as well double muon PD datasets showed in the same table.

918 A.2 Tracking, ID and Isolation Efficiencies

919 After many iterations with the muon POG group, we found a fixed way to define our objects (Tags,
 920 Probes and Pairs) in order to calculate properly the efficiencies. When considering efficiencies that is
 921 related only to one leg we define the tag using the same criteria applied in the construction of the Muon
 922 POG Tag-and-Probe trees[64], i.e., a Tight muon with $p_T > 15 \text{ GeV}$ matched with the L3 trigger collec-
 923 tion and with a loose PFlow isolation cut. These definitions were used to calculate our identification and
 924 isolation efficiencies.

925 Tracking Efficiency

926 For this case we use scale factors values provided by the muon POG[64]. The Tags have the same defi-

Table 15: Data and Monte Carlo samples.

PD	$\int Ldt (fb^{-1})$
SingleMu	
/SingleMu/Run2012A-22Jan2013-v1/AOD	0.89
/SingleMu/Run2012B-22Jan2013-v1/AOD	4.4
/SingleMu/Run2012C-22Jan2013-v1/AOD	7.1
/SingleMu/Run2012D-22Jan2013-v1/AOD	7.3
DoubleMu	
/DoubleMu/Run2012A-22Jan2013-v1/AOD	0.89
/DoubleMuParked/Run2012B-22Jan2013-v1/AOD	4.4
/DoubleMuParked/Run2012C-22Jan2013-v1/AOD	7.1
/DoubleMuParked/Run2012D-22Jan2013-v1/AOD	7.3
MC	# events
/DYJetsToLL-M50-TuneZ2Star-8TeV-madgraph	30459503

nitions as described above with an additional matching with the single trigger IsoMu24-eta2p1 and the Probes are defined as standalone muons. The efficiency is obtained requiring the muon to be matched to a tracker within $\Delta R < 0.3$.

930 Muon ID Efficiency

Table 16: Efficiencies for the “Global Muon ID” using the trees that we produced and the trees from muon POG group.

	p_T (GeV)	DATA - Our Trees	DATA - POG Trees	MC - Our Trees	MC - POG Trees
$0 < \eta < 0.9$	20-40	0.9615 ± 0.0003	0.9615 ± 0.0003	0.9650 ± 0.0002	0.9651 ± 0.0002
	40-60	0.9614 ± 0.0002	0.9614 ± 0.0002	0.9662 ± 0.0002	0.9662 ± 0.0002
	60-80	0.9694 ± 0.0008	0.9694 ± 0.0008	0.9676 ± 0.0007	0.9673 ± 0.0007
	80-100	0.9758 ± 0.0018	0.9758 ± 0.0018	0.9685 ± 0.0016	0.9687 ± 0.0016
	100-500	0.9760 ± 0.0029	0.9762 ± 0.0029	0.9694 ± 0.0023	0.9691 ± 0.0023
$0.9 < \eta < 1.2$	20-40	0.9643 ± 0.0005	0.9643 ± 0.0005	0.9681 ± 0.0004	0.9687 ± 0.0004
	40-60	0.9655 ± 0.0003	0.9655 ± 0.0003	0.9690 ± 0.0004	0.9691 ± 0.0004
	60-80	0.9751 ± 0.0015	0.9752 ± 0.0015	0.9738 ± 0.0015	0.9740 ± 0.0015
	80-100	0.9764 ± 0.0034	0.9761 ± 0.0034	0.9706 ± 0.0032	0.9726 ± 0.0032
	100-500	0.9753 ± 0.0059	0.9753 ± 0.0059	0.9697 ± 0.0049	0.9725 ± 0.0049
$1.2 < \eta < 2.1$	20-40	0.9565 ± 0.0003	0.9565 ± 0.0003	0.9573 ± 0.0001	0.9579 ± 0.0001
	40-60	0.9578 ± 0.0002	0.9578 ± 0.0002	0.9596 ± 0.0003	0.9597 ± 0.0003
	60-80	0.9675 ± 0.0012	0.9674 ± 0.0012	0.9637 ± 0.0011	0.9631 ± 0.0011
	80-100	0.9752 ± 0.0027	0.9750 ± 0.0027	0.9629 ± 0.0025	0.9619 ± 0.0025
	100-500	0.9784 ± 0.0052	0.9785 ± 0.0052	0.9609 ± 0.0034	0.9608 ± 0.0034
$2.1 < \eta < 2.4$	20-40	0.9651 ± 0.0022	0.9650 ± 0.0022	0.9644 ± 0.0024	0.9648 ± 0.0024
	40-60	0.9623 ± 0.0010	0.9623 ± 0.0010	0.9668 ± 0.0007	0.9668 ± 0.0007
	60-80	0.9679 ± 0.0061	0.9674 ± 0.0061	0.9748 ± 0.0032	0.9770 ± 0.0032
	80-100	0.9493 ± 0.0075	0.9491 ± 0.0075	0.9657 ± 0.0049	0.9807 ± 0.0077
	100-500	1.0000 ± 0.0122	1.0000 ± 0.0122	0.9581 ± 0.0092	0.9530 ± 0.0128

For the muon ID we define the probes as general tracks and test the two identification definitions presented above. We study these efficiencies in bins of p_T and η . Just as a cross-check in the Table 16 we present a comparison between our trees and muon POG trees for “Global ID” efficiencies for both data and MC, and as expected we note that the values are very close, in general within 1%. Also in the Table 17 we present the results including the “Tracker ID”, but now only using our trees. We note that in general we have higher efficiencies for the “Tracker ID” (in both DATA and MC) varying between 0.5 – 3% higher than the “Global ID”. In general for the last bin in η we have higher oscillations in the efficiencies values due to the smaller statistic in this bin for high p_T .

Table 17: *Efficiencies for the “Tracker and Global Muon ID” in DATA and MC.*

	p_T (GeV)	DATA - Glb ID	MC - Glb ID	DATA - Tkr ID	MC - Tkr ID
$0 < \eta < 0.9$	20-40	0.9615 ± 0.0003	0.9650 ± 0.0002	0.9694 ± 0.0002	0.9712 ± 0.0002
	40-60	0.9614 ± 0.0002	0.9662 ± 0.0002	0.9694 ± 0.0002	0.9719 ± 0.0002
	60-80	0.9694 ± 0.0008	0.9676 ± 0.0007	0.9768 ± 0.0007	0.9740 ± 0.0007
	80-100	0.9758 ± 0.0018	0.9685 ± 0.0016	0.9837 ± 0.0017	0.9744 ± 0.0015
	100-500	0.9760 ± 0.0029	0.9694 ± 0.0023	0.9836 ± 0.0029	0.9762 ± 0.0021
$0.9 < \eta < 1.2$	20-40	0.9643 ± 0.0005	0.9681 ± 0.0004	0.9692 ± 0.0005	0.9714 ± 0.0004
	40-60	0.9655 ± 0.0003	0.9690 ± 0.0004	0.9707 ± 0.0003	0.9721 ± 0.0004
	60-80	0.9751 ± 0.0015	0.9738 ± 0.0015	0.9799 ± 0.0015	0.9773 ± 0.0015
	80-100	0.9764 ± 0.0034	0.9706 ± 0.0032	0.9804 ± 0.0034	0.9746 ± 0.0031
	100-500	0.9753 ± 0.0059	0.9697 ± 0.0049	0.9780 ± 0.0059	0.9731 ± 0.0046
$1.2 < \eta < 2.1$	20-40	0.9565 ± 0.0003	0.9573 ± 0.0001	0.9639 ± 0.0003	0.9650 ± 0.0003
	40-60	0.9578 ± 0.0002	0.9596 ± 0.0003	0.9650 ± 0.0002	0.9667 ± 0.0003
	60-80	0.9675 ± 0.0012	0.9637 ± 0.0011	0.9747 ± 0.0011	0.9709 ± 0.0010
	80-100	0.9752 ± 0.0027	0.9629 ± 0.0025	0.9815 ± 0.0026	0.9737 ± 0.0023
	100-500	0.9784 ± 0.0052	0.9609 ± 0.0034	0.9845 ± 0.0052	0.9674 ± 0.0032
$2.1 < \eta < 2.4$	20-40	0.9651 ± 0.0022	0.9644 ± 0.0024	0.9833 ± 0.0167	0.9813 ± 0.0005
	40-60	0.9623 ± 0.0010	0.9668 ± 0.0007	0.9827 ± 0.0007	0.9843 ± 0.0005
	60-80	0.9679 ± 0.0061	0.9748 ± 0.0032	0.9887 ± 0.0002	0.9959 ± 0.0024
	80-100	0.9493 ± 0.0075	0.9657 ± 0.0049	0.9714 ± 0.0072	0.9876 ± 0.0039
	100-500	1.0000 ± 0.0122	0.9581 ± 0.0092	1.0000 ± 0.0063	0.9918 ± 0.0077

939 **Isolation Efficiency**Table 18: *Modified tracker based relative isolation efficiencies in DATA and MC. We present efficiencies values defining the probes with “Global and Tracker Muon ID”.*

	p_T (GeV)	DATA - ISO Glb ID	MC - ISO Glb ID	DATA - ISO Tkr ID	MC - ISO Tkr ID
$0 < \eta < 0.9$	20-40	$0.987017 \pm 8.345\text{e-}05$	0.986199 ± 0.0001142	$0.987011 \pm 8.328\text{e-}05$	0.986204 ± 0.0001139
	40-60	$0.99766 \pm 3.192\text{e-}05$	$0.997783 \pm 4.584\text{e-}05$	$0.99766 \pm 3.164\text{e-}05$	$0.9977 \pm 4.106\text{e-}05$
	60-80	$0.999391 \pm 6.683\text{e-}05$	$0.999404 \pm 8.298\text{e-}05$	$0.999394 \pm 6.307\text{e-}05$	$0.999407 \pm 8.244\text{e-}05$
	80-100	$0.999842 \pm 6.620\text{e-}05$	0.999776 ± 0.0001139	$0.999843 \pm 6.56\text{e-}05$	0.999777 ± 0.0001133
	100-500	$0.999895 \pm 7.751\text{e-}05$	1.000000 ± 0.0001451	$0.999895 \pm 7.696\text{e-}05$	1.000000 ± 0.0001446
$0.9 < \eta < 1.2$	20-40	0.987164 ± 0.0001950	0.986167 ± 0.0002144	0.987177 ± 0.0002025	0.986175 ± 0.0002146
	40-60	$0.997886 \pm 5.501\text{e-}05$	$0.998024 \pm 7.931\text{e-}05$	$0.997892 \pm 5.500\text{e-}05$	$0.998022 \pm 7.840\text{e-}05$
	60-80	0.999455 ± 0.0001270	0.999385 ± 0.0001619	0.999458 ± 0.0001264	0.999387 ± 0.0001615
	80-100	1.000000 ± 0.0001278	1.000000 ± 0.0003052	1.000000 ± 0.0001276	1.000000 ± 0.0003035
	100-500	1.000000 ± 0.0002391	1.000000 ± 0.0004903	1.000000 ± 0.000238	1.000000 ± 0.000487
$1.2 < \eta < 2.1$	20-40	$0.988400 \pm 9.79\text{e-}05$	0.987406 ± 0.0001250	$0.988428 \pm 9.673\text{e-}05$	0.987423 ± 0.000125
	40-60	0.957781 ± 0.0002291	0.959644 ± 0.0002916	$0.998301 \pm 3.341\text{e-}05$	$0.998116 \pm 1.368\text{e-}05$
	60-80	$0.99956 \pm 6.052\text{e-}05$	0.999621 ± 0.0001055	$0.999563 \pm 6.055\text{e-}05$	0.999641 ± 0.0001029
	80-100	$0.999967 \pm 4.731\text{e-}05$	0.999852 ± 0.0001223	$0.999967 \pm 4.700\text{e-}05$	0.999854 ± 0.0001212
	100-500	1.000000 ± 0.0001234	0.999731 ± 0.0002263	1.000000 ± 0.0001226	$0.999733 \pm 5.825\text{e-}06$
$2.1 < \eta < 2.4$	20-40	0.992463 ± 0.0001300	0.991757 ± 0.0001901	0.992435 ± 0.0001265	0.991727 ± 0.0001785
	40-60	$0.999135 \pm 5.994\text{e-}05$	$0.998997 \pm 7.742\text{e-}05$	$0.999121 \pm 6.563\text{e-}05$	$0.999008 \pm 7.628\text{e-}05$
	60-80	$0.999876 \pm 9.518\text{e-}05$	$0.999956 \pm 3.63\text{e-}05$	$0.999878 \pm 9.316\text{e-}05$	$0.999957 \pm 3.539\text{e-}05$
	80-100	1.000000 ± 0.0003940	0.999637 ± 0.0004728	1.000000 ± 0.0003858	0.999643 ± 0.0004648
	100-500	1.000000 ± 0.000867	1.000000 ± 0.00137	1.000000 ± 0.0008542	1.000000 ± 0.001335

940 We calculate the isolation efficiency considering two situations for the Probes: defined with a “Global
941 ID” and with a “Tracker ID”. Then the probes are required to pass a cut in the isolation variable,
942 $\text{Isolation} < 0.1$. In Table 18 we present these efficiencies. In general we note a very good agreement
943 between DATA and MC within 0.1% in both cases (for Probes with Global and Tracker ID). Comparing
944 between the Tracker and Global probes definitions we don’t observe big differences. As we are studying
945 a relative isolation, for the bins with smaller p_T ($p_T < 40\text{GeV}$) we observe smaller efficiencies in both
946 DATA and MC.

947 **Scale Factors**

Table 19: *Scale Factors for the ID times isolation efficiencies. These values consider the “Tracker and Global muon ID” definitions.*

	p_T (GeV)	GlobalID*ISO	TrackerID*ISO
$0 < \eta < 0.9$	20-40	0.9972 ± 0.0004	0.9989 ± 0.0004
	40-60	0.9948 ± 0.0003	0.9973 ± 0.0003
	60-80	1.0018 ± 0.0011	1.0029 ± 0.0010
	80-100	1.0076 ± 0.0025	1.0096 ± 0.0023
	100-500	1.0068 ± 0.0039	1.0075 ± 0.0037
$0.9 < \eta < 1.2$	20-40	0.9971 ± 0.0007	0.9988 ± 0.0007
	40-60	0.9963 ± 0.0005	0.9985 ± 0.0005
	60-80	1.0014 ± 0.0022	1.0028 ± 0.0021
	80-100	1.0060 ± 0.0049	1.0060 ± 0.0047
	100-500	1.0058 ± 0.0080	1.0050 ± 0.0077
$1.2 < \eta < 2.1$	20-40	1.0001 ± 0.0004	0.9999 ± 0.0005
	40-60	0.9982 ± 0.0004	0.9985 ± 0.0004
	60-80	1.0039 ± 0.0017	1.0039 ± 0.0016
	80-100	1.0129 ± 0.0039	1.0081 ± 0.0036
	100-500	1.0185 ± 0.0065	1.0180 ± 0.0063
$2.1 < \eta < 2.4$	20-40	1.0015 ± 0.0030	1.0028 ± 0.0009
	40-60	0.9955 ± 0.0012	0.9985 ± 0.0009
	60-80	0.9929 ± 0.0071	0.9927 ± 0.0024
	80-100	0.9834 ± 0.0092	0.9839 ± 0.0082
	100-500	1.0438 ± 0.0160	1.0083 ± 0.0099

948 The scale factors presented in this subsection are taken from the ratio between data and MC of the ID
949 times Isolation efficiencies. The idea is to apply on top of these values the scale factors of the tracking
950 efficiencies from muon POG.

951 On Table 19 we present the scale factors for the ID times isolation for both cases: Tracker and Global
952 ID. Looking to these numbers we confirm what we saw in the previous tables, that in general the DATA
953 and MC have a very similar behaviour concerning our ID and Isolation definitions. We observe some
954 oscillations in the values of the scale factors for the last bin in η , but it's mostly due to the small statistic
955 in this region.

956 It's important to note that all the uncertainties showed in the tables are statistical ones. For the sys-
957 tematics we apply a flat conservative value per event. We consider a 2% from standard muon POG
958 systematics in the ID and isolation and add a more 2% due to the boosted topology (see [65]).

959 A.3 HLT Trigger Efficiencies

960 The double trigger HLT-Mu22TkMu8 in 2012 Runs has in its path a last filter that apply a cut in the
961 z-coordinate of the Point of Closest Approach (PCA) of the two muons ($dz < 0.2$ cm), so that in order
962 to calculate the efficiency of the trigger we need to consider this dz filter as well. In this analysis we
963 are using the Reference Trigger Method developed by muon POG [66] that works in the framework of
964 a single trigger (called reference trigger) to obtain efficiencies of double triggers or more complicated
965 combinations of triggers (Soup). After many iterations with muon POG experts it was possible to com-
966 pare our results with the POG results for a known double muon trigger - in the case HLT-Mu17TkMu8
967 (see Figure 49). We note a very good agreement within 1% for most of the bins in $|\eta|$. With these cross-
968 checks we calculate the efficiencies in data and mc for our path and obtain the scale factors presented
969 in Figure 50. In this plot we consider our modified ID and isolation. Using the same object definitions
970 we show the plots in a different η binning for HLT Mu22TkMu8 and the reference trigger HLT Mu17 in
971 data and mc (respectively, Figures 51 and 52). Based in previous studies by muon POG on systematics
972 for this method [66], in general studies of possible efficiencies variations due to the binning in eta or the
973 choose of the reference trigger (in the case the highly prescaled HLT-Mu17), we decided to consider a
974 constant conservative value of 3% for the systematics.

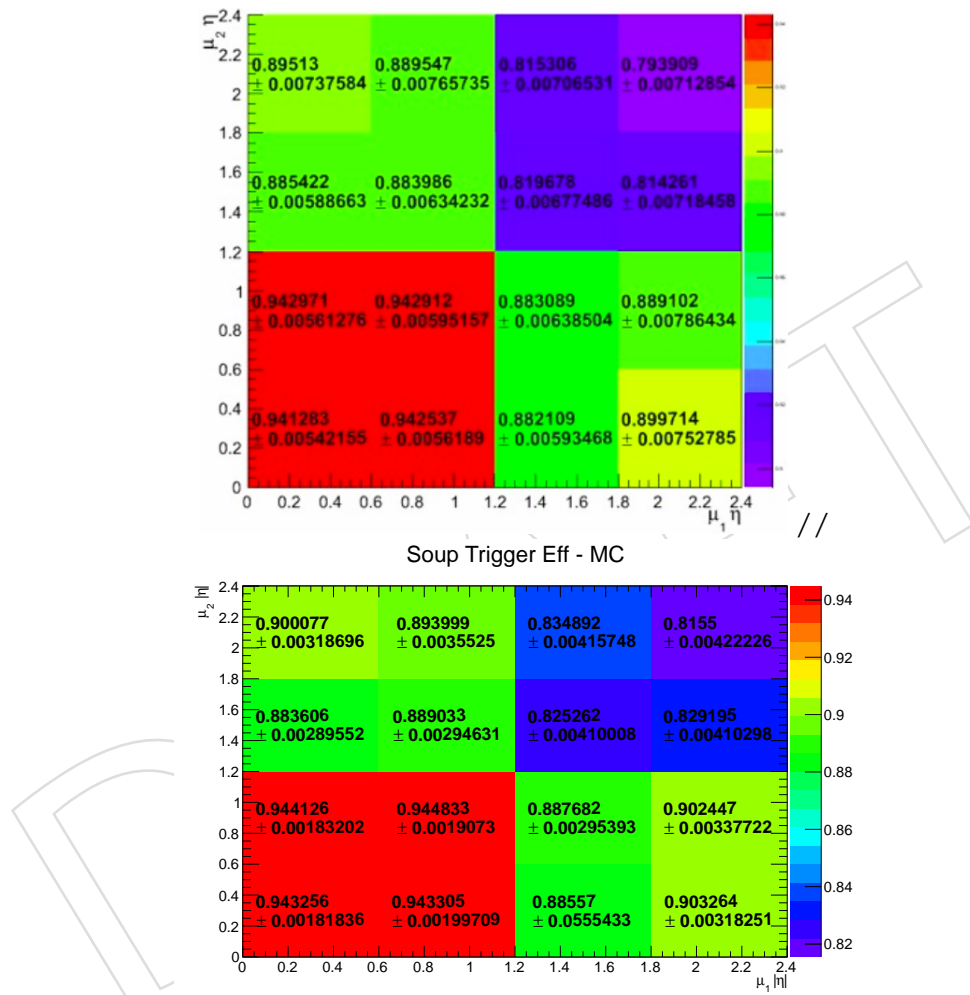


Figure 49: Comparison with muon POG results using DY events for Mu17TkMu8 double trigger considering muons passing the Loose ID. The two muons (μ_1 and μ_2) have the same p_T cut of 20 GeV. Top: Muon POG result. Bottom: result calculated by this analysis team.

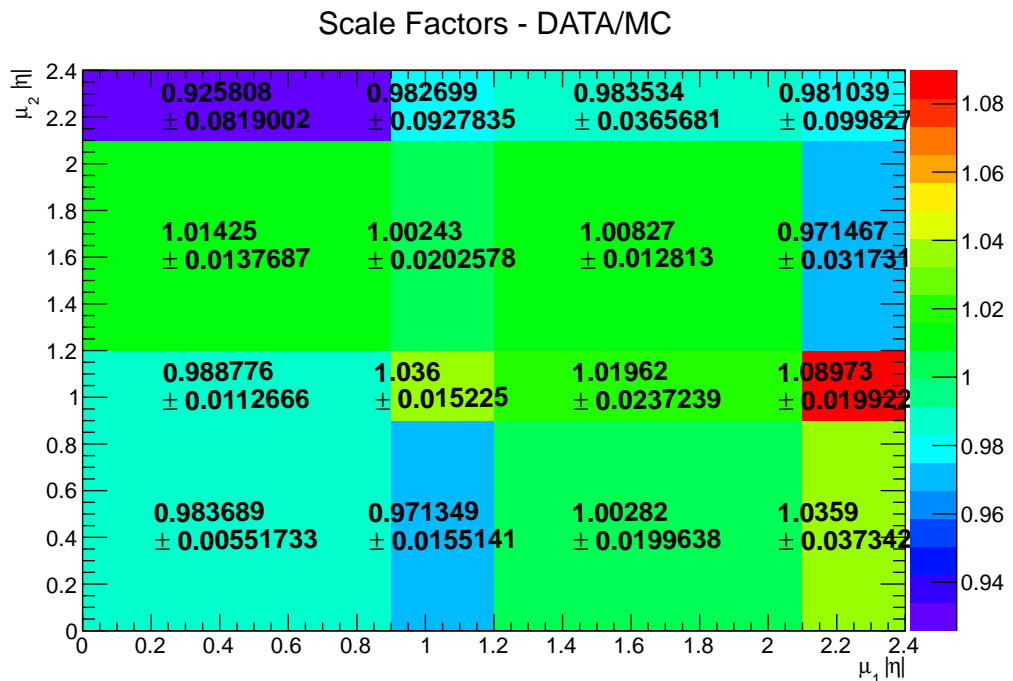


Figure 50: Final Scale Factors for Mu22TkMu8 double trigger considering muons passing our modified ID and isolation requirements. We consider one muon with $p_T > 20$ GeV (μ_1) and the other with $p_T > 40$ GeV (μ_2).

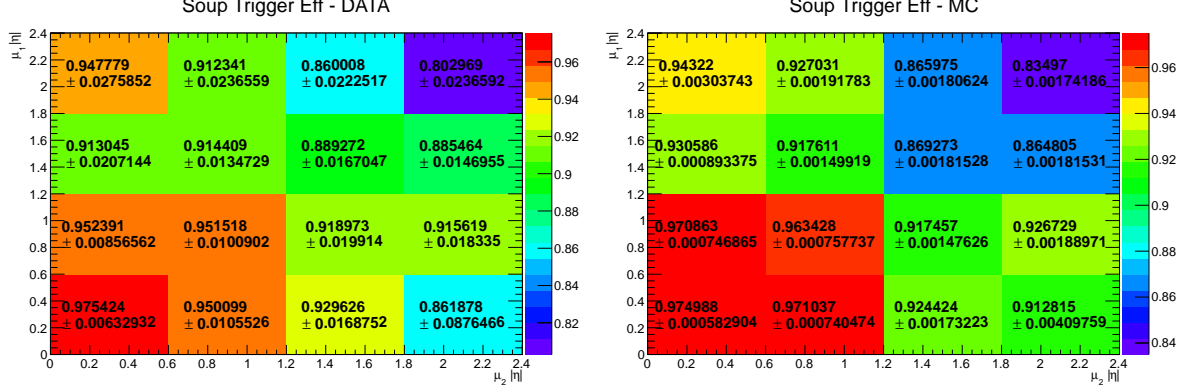


Figure 51: $HLTMu22TkMu8$ efficiency for muons passing our modified ID and isolation criteria for Data (left) and MC (right). We consider one muon with $p_T > 20$ GeV (μ_1) and the other with $p_T > 40$ GeV (μ_2).

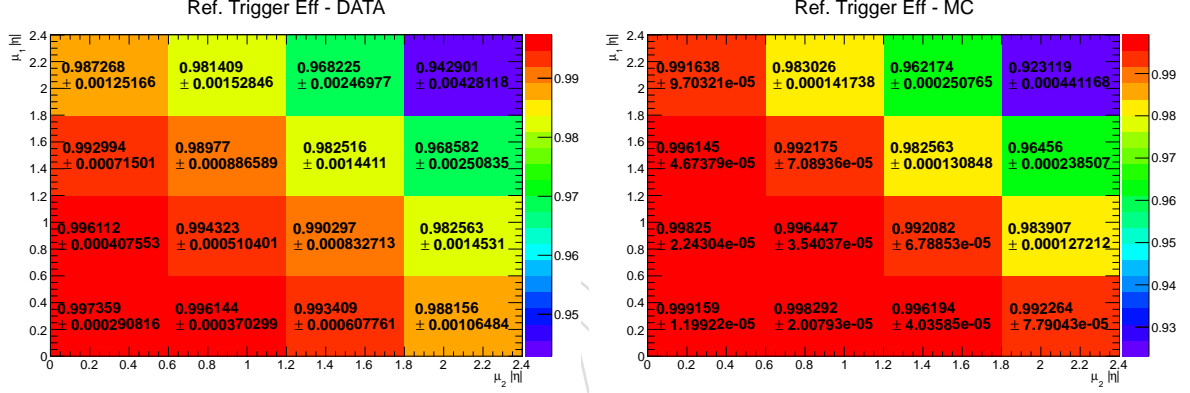


Figure 52: Efficiency for at least one muon passing our ID and isolation criteria to pass $HLTMu17$ for Data (left) and MC (right). We consider one muon with $p_T > 20$ GeV (μ_1) and the other with $p_T > 40$ GeV (μ_2).



975 B Quality of the background fits and parametrization studies

976 The distributions in data of m_{ZZ} extrapolated from the sideband to the signal region are used as inputs
 977 to a fit. The result of the fit is then used as model for the background to be compared to the data in the
 978 signal region. Therefore, it is of crucial importance to have a fit of good quality, able to describe properly
 979 the extrapolated sidebands. The gauge of the fit quality that we use is the χ^2 of the fit normalized by the
 980 number of degrees of freedom, dof .

981 The other criterion for choosing an appropriate functional form of the fit function is the simplicity. Wher-
 982 ever two functions have similar performances, we prefer to use the one with less fit parameters. This
 983 choice has several advantages and it improves the robustness of the procedure: it is simpler from the
 984 conceptual and computational point of view, it reduces correlations between the parameters, eventually
 985 simplifying the treatment of the shape systematic uncertainties in the final statistical analysis.

986 In order to assess the need for more parameters, we performed what is called an “F-test”. We started
 987 from a functional form with several parameters, where the simple exponential can be recovered fixing all
 988 but one of the parameters. This expression is the leveled exponential of Eq.12, where one can recover the
 989 simple exponential fit by setting $p_0 = p_1 = 0$. We progressively complicate the form of the expression
 990 by letting the parameters free to float in the fit one-by-one. If the simpler model with np free parameters
 991 is correct (i.e., the χ^2 matches approximately the number of degrees of freedom), we expect that by
 992 increasing the number of free parameters by one the following relation holds

$$\frac{SS_{np} - SS_{np+1}}{SS_{np+1}} \approx \frac{dof_{np} - dof_{np+1}}{dof_{np+1}} \quad (14)$$

993 where we defined the sum of squares $SS = \sum_{i=1}^{nbins} (N_{pred} - N_{obs})^2$, with the sum running over the bins
 994 of the m_{ZZ} distribution. On the other hand, if the more complex model is more correct, in Eq.14 the
 995 left-hand side will be larger than the right-hand side.

996 The test statistics

$$F = \frac{(SS_{np} - SS_{np+1})(dof_{np} - dof_{np+1})}{SS_{np+1} dof_{np+1}} \quad (15)$$

997 distributes according to an F-distribution $f(F; 1, dof_{p+1})$. Large values of F will suggest a preference
 998 for the more complex function. The procedure of the $F - test$ is to define as null hypothesis the option
 999 with less parameters and set before the start a false-rejection critical value. Every time we increased np
 1000 by one, the value of the cumulative distribution of $f(F; 1, dof_{p+1})$, $Int_f(F; 1, dof_{p+1})$, was evaluated. If
 1001 $1 - Int_f$ is smaller than the critical value, the functional form with more parameters has to be preferred⁴.

1002 We compared three different functions, letting free respectively the parameters σ (simple exponential),
 1003 (σ, p_0) (leveled exponential of 2nd degree) and (σ, p_0, p_1) (leveled exponential of 3rd degree). In all
 1004 cases, we set to zero the parameters of Eq.12 that were kept fixed, except $m_0 = 560$ GeV⁵.

1005 The results of the fits to the three categories (1JHP, 1JLP, 2J) with the three fit functions considered
 1006 are shown in Fig.53. Qualitatively speaking, adding more parameters does not change very much the
 1007 resulting fit shape. The largest differences are seen at very high m_{ZZ} , where the statistical uncertainties
 1008 are dominant anyway.

1009 The m_{ZZ} distribution in the data sidebands after the extrapolation to the signal region with the $\alpha(m_{ZZ})$
 1010 ratio has been discretized with regular bins 50 GeV wide in the range [600, 2400] GeV. This allows us

⁴The calculation of the cumulative F-distribution is implemented in the standard ROOT libraries (`TMath::FDistI`).

⁵This parameter is very largely correlated to the others and the quality of the fit is only very weakly affected by its value - as long as it is smaller than the lowest bound of the fit range.

1011 to perform tests of goodness-of-fit with the χ^2 and the $F - test$. The errors used for evaluating bin-by-
 1012 bin the χ^2 are the Poissonian errors of the fitted dataset. We defined as critical value for type I errors
 1013 (wrong rejection of the null hypothesis) to 0.05. A compilation of the results of the $\chi^2 -$ and $F - test$ are
 1014 summarized in Table 20, 21 and 22.

1015 For the 1JHP and 1JLP categories, the fits are in general very good, with very good χ^2 probabilities. The
 1016 $F - test$ in the 1JHP category (the one with the highest sensitivity, see Sect. 9) suggests to use the simple
 1017 exponential, as the gain in the description brought by the other functions is not significant. In the 1JLP
 1018 category, there is the numerical preference for a 3rd degree leveled exponential fit function. However, it
 1019 has to be stressed how this improvement is done at the expenses of the χ^2 probability and how the 3rd
 1020 degree leveled exponential of the fit has a strange turn-off at high m_{ZZ} . Since in the region of the turn-
 1021 off there are no data able to constrain this behaviour, we think it is safer to stick to the 2nd degree leveled
 1022 exponential as it gives already a good quality of the description and exhibits a smoother behavior.

1023 The fits in the 2J category do not have a good χ^2 . Non-smooth structures around $m_{ZZ} \sim 1000$ GeV affect
 1024 the general quality of the fit and make very hard to find a suitable functional form. While the origin of
 1025 these structures is still under investigation, it has to be reminded that we do not plan to use this category
 1026 in that mass range anyway (see Sect. 9). Therefore this discrepancy is harmless to the analysis.

np	χ^2	dof	χ^2/dof	$Prob(\chi^2; dof)$	F (respect to $np + 1$)	$1 - Int_f(F; 1, dof_{np+1})$
1	22.3	13	1.715	0.051	-0.440	1
2	23.0	12	1.917	0.028	+10.795	0.007
3	49.6	11	4.508	$< 10^{-6}$	—	—

Table 20: Comparison between different functional forms used for the fit to the 1JHP category. The m_{ZZ} range considered is [600, 2400] GeV. As a function of the number of parameters of the leveled exponential left free in the fit (np), the results of the $\chi^2 - test$ and $F - test$ are presented.

np	χ^2	dof	χ^2/dof	$Prob(\chi^2; dof)$	F (respect to $np + 1$)	$1 - Int_f(F; 1, dof_{np+1})$
1	20.292	12	1.691	0.062	-1.476	1
2	20.378	11	1.853	0.040	-0.223	1
3	18.885	10	1.888	0.042	—	—

Table 21: Comparison between different functional forms used for the fit to the 1JLP category. The m_{ZZ} range considered is [600, 2400] GeV. As a function of the number of parameters of the leveled exponential left free in the fit (np), the results of the $\chi^2 - test$ and $F - test$ are presented.

np	χ^2	dof	χ^2/dof	$Prob(\chi^2; dof)$	F (respect to $np + 1$)	$1 - Int_f(F; 1, dof_{np+1})$
1	22.796	7	3.257	0.002	51.422	3.7E-04
2	13.267	6	2.211	0.039	-1.255	1
3	12.615	5	2.523	0.027	—	—

Table 22: Comparison between different functional forms used for the fit to the 2J category. The m_{ZZ} range considered is [600, 2400] GeV. As a function of the number of parameters of the leveled exponential left free in the fit (np), the results of the $\chi^2 - test$ and $F - test$ are presented.

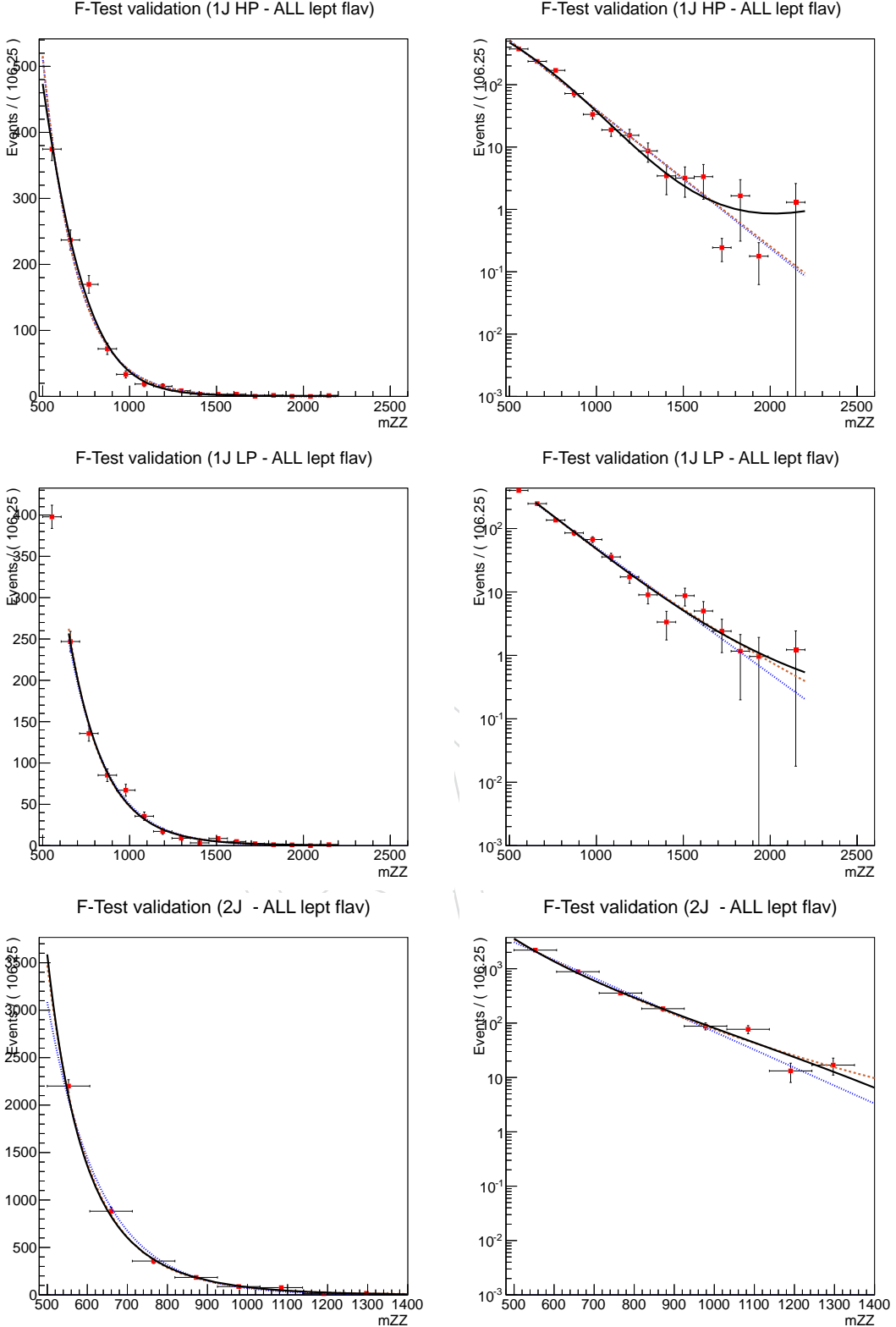


Figure 53: Fits to sideband data rescale to signal region, using 19.5 fb^{-1} lumi. Three different fit functions are considered: a simple exponential (dotted blue), a leveled exponential of 2nd degree (dashed red) and a leveled exponential of 3rd degree (solid black). Three event categories are shown from top to bottom: 1JHP, 1JLP, 2J. The distributions sum up over the two lepton flavor considered by the analysis, electron and muons. Left: linear scale, right: log scale.

1027 C Bias Studies

1028 To guard against possible biases due to the specific choice of background function, we study the realtive
 1029 bias of several possible choices. The functions under study are:

- 1030 • a simple exponential
- 1031 • a leveled exponential (see equation 12, with $p_1 = 0$)
- 1032 • a modified powerlaw: $m_{ZZ}^{(a+b*m_{ZZ})}$

1033 The procedure to test for possible biases is as follows: The weighted sideband data (high purity channel)
 1034 is fit with one of the three functions. Using the fit-result, we generate a large number of pseudo-
 1035 experiments. Each of the pseudoexperiments is fit with the sum of the signal shape (1.5 TeV) and another
 1036 one of the three functions. We then plot the pull for the signal fraction $(f_{sig,fit} - f_{sig,true}) / \sigma_f$, where the
 1037 true signal fraction $f_{sig,true}$ is zero, as no signal events are added to the pseudoexperiment. The fitted
 1038 signal fraction, $f_{sig,fit}$, was constrained to be non-negative. This strategy should enhance possible biases
 1039 compared to the full analysis, as the final fit of the background shape is not constrained to any sideband
 1040 data.

1041 The results for all nine combinations of generating and fitting function are shown in figure 54. The plots
 1042 on the diagonal show the inherent bias for each of the functions chosen, which is small and similar
 1043 among our choices, so this number is used as baseline for comparisons with different generating and
 1044 fitting functions. Two plots in the top row, indicate that each of the two-paramter functions can ade-
 1045 quately describe spectra produced from the simple exponential. This is expected at least for the leveled
 1046 exponential, which describes a strict superset of functions compared to the simple exponential. In the
 1047 first column, we see the opposite effect: the simple exponential cannot adequately describe spectra gen-
 1048 erate with the more complex 2-parameter functions, leading to a comparatively large average signal
 1049 fraction in the absence of a real signal. The pull-plots showing the performance of the leveled expo-
 1050 nential compared to the modified powerlaw are very similar to the plots that were produced with the
 1051 same generating and fitting functions. Althought the two functions are structurally quite similar, each
 1052 of them can well describe spectra generated by the other one.

1053 From this study we conclusde that the simple exponential is not adequate to describe the background
 1054 in the high purity category, while both 2-parameter functions appear adequate.

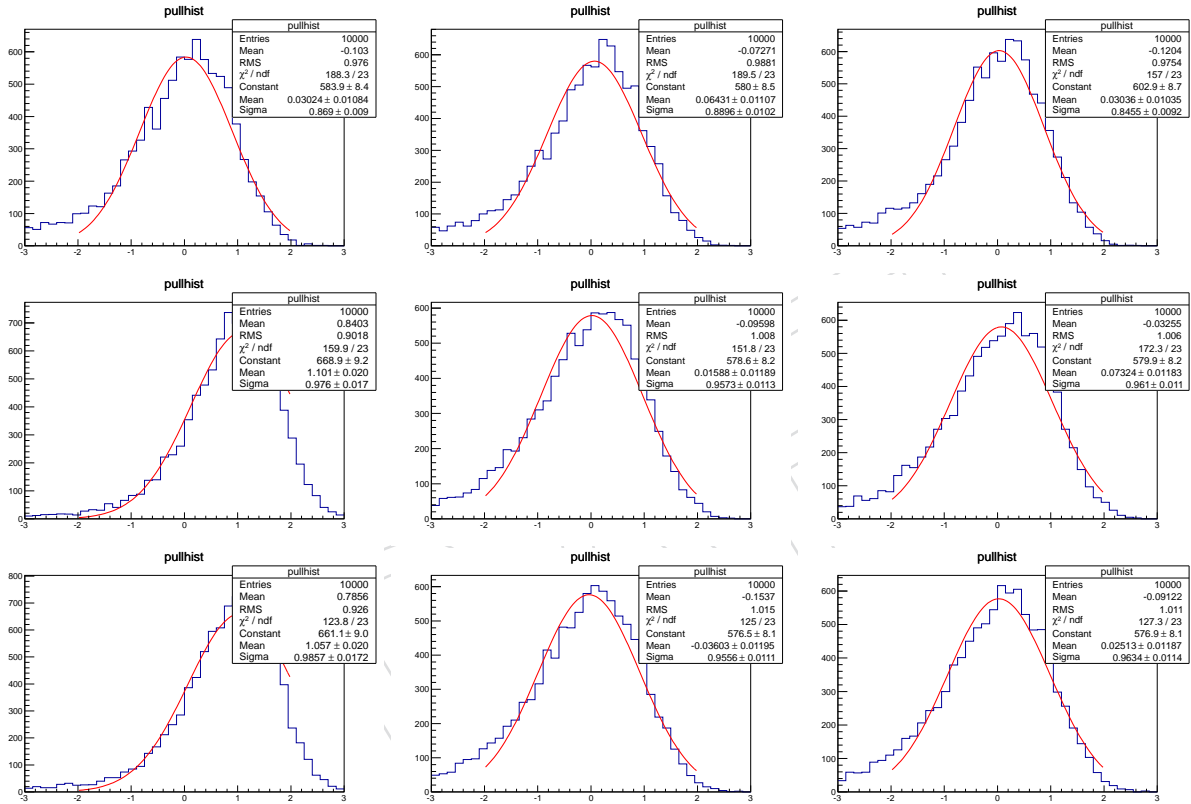


Figure 54: Signal fraction pulls for the nine combinations of generating and fitting function. Rows denote generating function (top: exponential, middle: leveled exponential, bottom: modified powerlaw). The columns denote fitting functions (left: exponential, middle: leveled exponential, bottom: modified powerlaw).

1055 D Alternative Approach to the Limit-setting Procedure

1056 As a cross-check to the limit-setting procedure detailed in Sect. 9, we consider the alternative approach
 1057 used in the “Search for Resonances in the Dijet Spectrum” [18, 67]. In this alternative approach, no
 1058 sideband region in the jet pruned mass is considered at all. Instead, the standard model background in
 1059 the signal region is considered to be well-described by a steeply falling reconstructed mass distribution.
 1060 and we simply consider the two competing hypotheses:

- 1061 • observed data is described by this smooth background
- 1062 • observed data is not described by a sum of this smooth background because of a localized
 1063 excess (“bump”).

For the background parametrization, we use the aforementioned levelled exponential:

$$f(m_{ZZ}) = N \cdot e^{-\frac{m_{ZZ}}{p_0 + p_1 m_{ZZ}}} \quad (16)$$

1064 while we parametrize the posited excesses as the signal shapes from the standard analysis (Double
 1065 Crystal Ball shapes).

1066 The main strength of this method is that it does not rely on the knowledge of a transfer function between
 1067 the sideband region and the signal region in jet pruned mass. Conversely, since this information is not
 1068 used, that means that the cross-section upper limit inferred from the observed data is higher than that
 1069 which is obtained from the standard analysis.

1070 In technical terms, the limit-setting procedure in this approach is as follows:

- 1071 • The observed data are divided in four categories (electron/muon, low/high purity)
- 1072 • For each category, the background is posited to take the form of the levelled exponential.
- 1073 • For each category, the signal shapes are taken to be the same as in the standard analysis.
- 1074 • The data are both fit to the background-only hypothesis, and the background+signal hypothesis,
 1075 in each of the four categories separately.
- 1076 • An hypothesis test is performed and then inverted, through usage of the CL_S method, for
 1077 each of the four categories.
- 1078 • The four upper-limits are combined in order to form a final upper-limit; correlated system-
 1079 atics are taken into account.

1080 The background fits in the signal region are shown in Fig. 55. The results of this approach to the limit-
 1081 setting can be seen in Fig. 56. This cross-check is meant only to support the main result: for this reason
 1082 only a subset of systematics was included; in particular, no signal shape systematics were considered.
 1083 Despite of this, it can be seen that the limit set with this procedure follows the general trend of the limit
 1084 set in the standard analysis, albeit at higher values the expected limit is approximately 25% worse. This
 1085 is due to the lack of extra information (from the sideband region) that we input to the limit-setting tool.

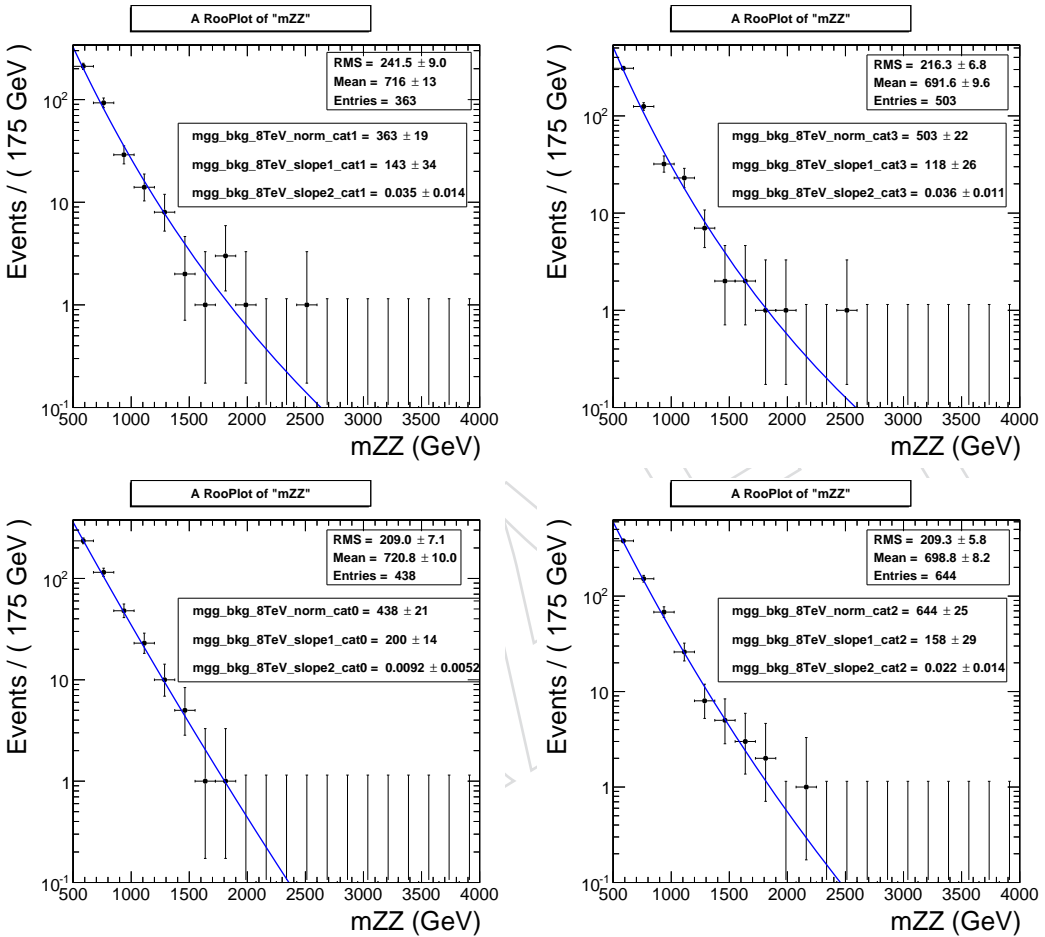


Figure 55: Background fits with the levelled exponential function. Top left: electron channel, high-purity category. Top right: muon channel, high-purity category. Bottom left: electron channel, low-purity category. Bottom right: muon channel, low-purity category.

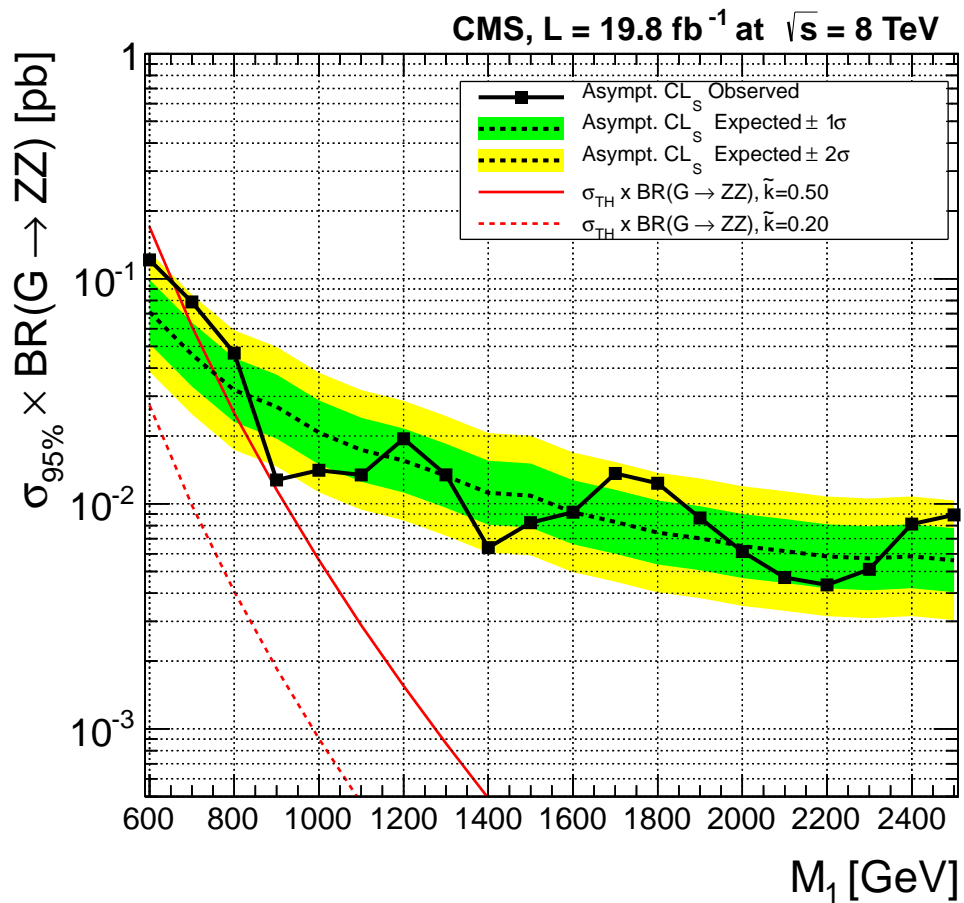


Figure 56: Combined limit of the four categories, as derived with the bump-search over smooth background technique. The limits are similar to the ones in the standard analysis.

1086 E Extension of the background fit to higher masses

1087 For masses $2200 \text{ GeV}/c^2$, the method described above is limited by the total absence of events in the
 1088 sideband region (see Fig.33). This allows us to set limits up to $m_{ZZ} = 2000 \text{ GeV}/c^2$, since one must
 1089 give some margin able to fully accommodate the signal shape. On the other hand, the presence of
 1090 events in the signal region at masses higher than this value would require the ability of estimating the
 1091 background up to $2800 - 3000 \text{ GeV}/c^2$. In order to be able to achieve this, it was decided to take the
 1092 background prediction straight from the MC (both Madgraph DY+jets and minor backgrounds from
 1093 Pythia).

1094 The normalization of the prediction of the MC background was validated against the data in the signal
 1095 region but with lower m_{ZZ} values. At a given value of m_{ZZ} , the total number of events predicted by
 1096 the background MC was counted in a window $[m_{ZZ} - 200 \text{ GeV}/c^2, m_{ZZ} + 200 \text{ GeV}/c^2]$. The same event
 1097 count was done for the data in the signal region and the pull of the two is built, giving a measure of how
 1098 much the MC normalization is off with respect to the data. This of course assumes the absence of a signal
 1099 in the data distribution. This is verified by the fact that with the standard background estimation method
 1100 no significant excesses are observed. The dependence of the pull versus m_{ZZ} gives us information on
 1101 the reliability of the MC normalization in the range $[2200, 2800] \text{ GeV}/c^2$. Fig. 57 shows this dependence
 1102 for the 1JHP category. While at medium m_{ZZ} the MC tends to overshoot the data, at high m_{ZZ} the
 1103 situation is the opposite. This indicates that the trend of the m_{ZZ} distribution in MC is steeper than
 1104 the data one and that the MC above $2200 \text{ GeV}/c^2$ must be likely scaled up. The plot indicates that the
 1105 scaling factor is approximately constant at high masses. Based on it, in the analysis we scale up by a
 1106 factor 2 the normalization of the MC prediction in the high-mass range where we include it in the fit
 1107 to the background function. Because of the many assumptions done in such a procedure and the large
 1108 statistical uncertainties in both data and MC, in the final statistical analysis described in Sect.9 we assign
 1109 a 100% systematic uncertainty on the background normalization for resonance masses above 2000 GeV .

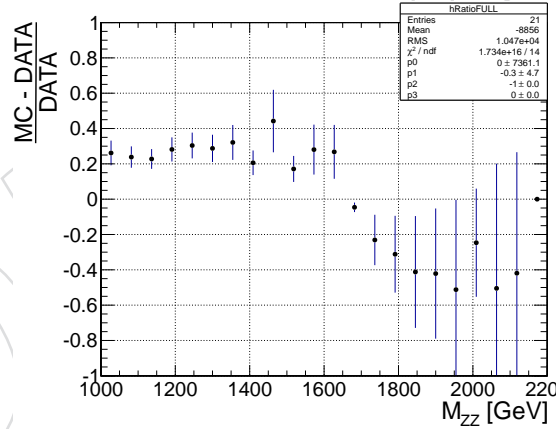


Figure 57: Scan as a function of m_{ZZ} of the difference in normalization between the data and the background MC.

1110 The fit with the additional MC events at high masses is shown in Fig.35. The values of the fitted param-
 1111 eters deviate only slightly from those that one would obtain stopping the fit at $m_{ZZ} = 2200 \text{ GeV}/c^2$ (i.e.
 1112 without including the high- m_{ZZ} MC events). the final limit obtained is the one shown in Fig.43. Addi-
 1113 tional cross-checks have been carried out in order to demonstrate that the final results are robust despite
 1114 the large uncertainties in the procedure adopted to extend the range of the fit above $m_{ZZ} = 2200 \text{ GeV}/c^2$.

1115 A different approach has been considered, not including the MC at high masses, but using a fit function
 1116 that for $m_{ZZ} \geq 2200 \text{ GeV}/c^2$ is flat. This function, although unphysical, is useful as it implements in
 1117 an analytical way our ignorance of the background behaviour at high masses due to the lack of events
 1118 in the data sidebands. The result of the fit is shown in Fig.58. In the final extraction of the limits, the
 1119 normalization uncertainty for masses above $2000 \text{ GeV}/c^2$ was inflated by 100% in order to stress our
 1120 uncertainties on the background in that region.

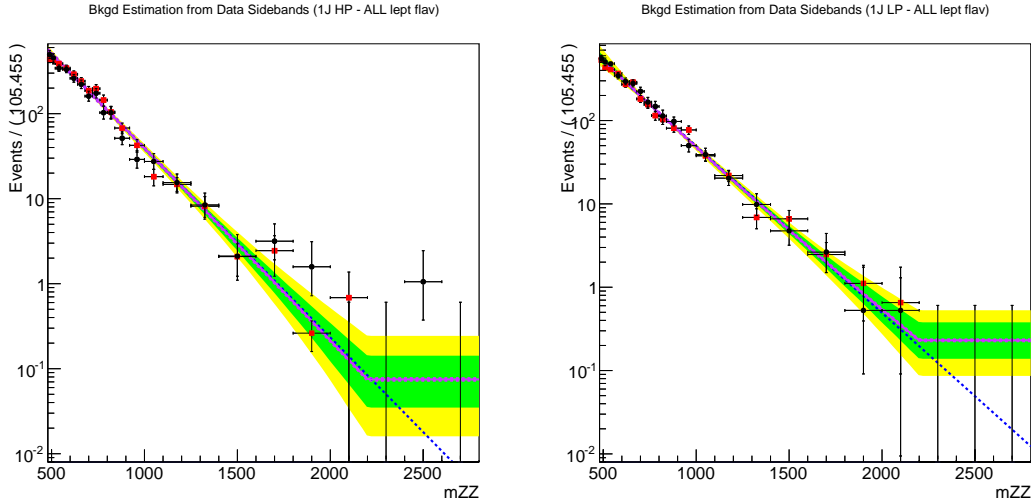


Figure 58: Result of the fit to the extrapolated sidebands (red markers) with a special fit function, equivalent to the one of the baseline analysis (Eq.12) but becoming constant at $m_{ZZ} = 2200 \text{ GeV}/c^2$. The fit for the 1JHP is shown in the left plot, the one for the 1JLP in the right plot. Electron and muon channels were summed together in the fits. The dashed blue line is the result of the fit with a simple exponential. The black circles show the distribution of the data observed in the signal region.

1121 A third cross-check comes from the dijet-like method for setting limits described in Appendix F. Since
 1122 this method performs a smoothness test to the observed data distribution, it does not rely neither on the
 1123 MC nor on the data in the sidebands, making it robust against problems related to lack of statistics in
 1124 the control regions.

1125 The final upper limits with the three approaches (baseline using MC for estimating the background
 1126 shape at high masses, flat tail at high masses and dijet-style method) are compared in Fig.59. Despite
 1127 the approaches are very different from each other (in one case the background model is even unphysical),
 1128 the final limit is very similar in all cases. This is related to the very limited statistics in the high-mass
 1129 region that heavily limits the effects of shape analyses and normalization uncertainties. Because of all
 1130 these reasons, we judged that the results obtained with the baseline analysis are safe up to $2500 \text{ GeV}/c^2$,
 1131 where we have the events with the highest m_{ZZ} passing our selections.

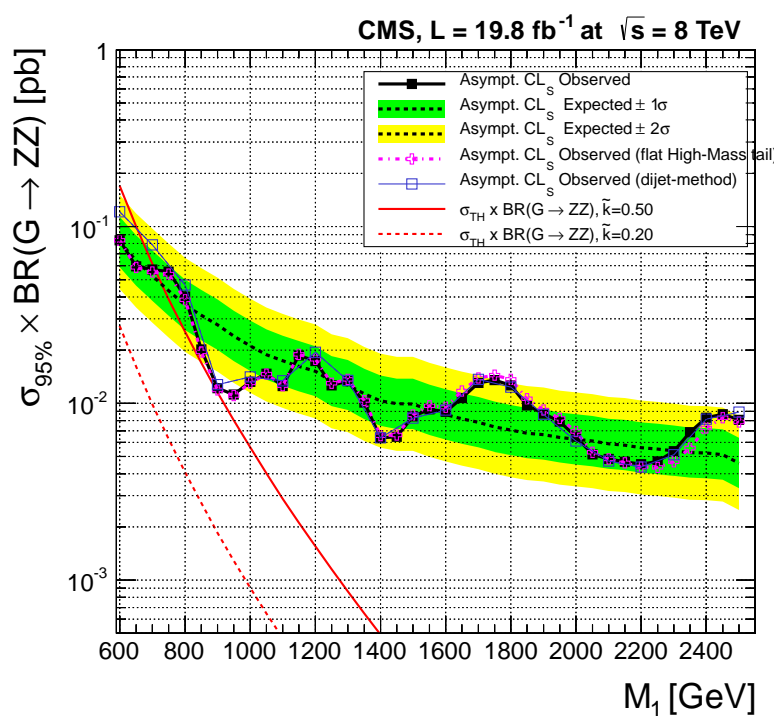


Figure 59: Comparison of the limits using three different approaches for the high-mass region.

F Event Displays

1132 Here we show some displays for interesting events collected by our analysis. The event displays are
1133 made directly at AOD level, with the 2013Jan22 re-reconstruction version. That means that many im-
1134 provements from our preselection stage, like the energy corrections for electrons, muons and jets, the
1135 charged hadron subtraction procedure and the pruning cannot be seen here. The basic features of the
1136 events are, however, preserved and can be seen in the displays.
1137

DRAFT

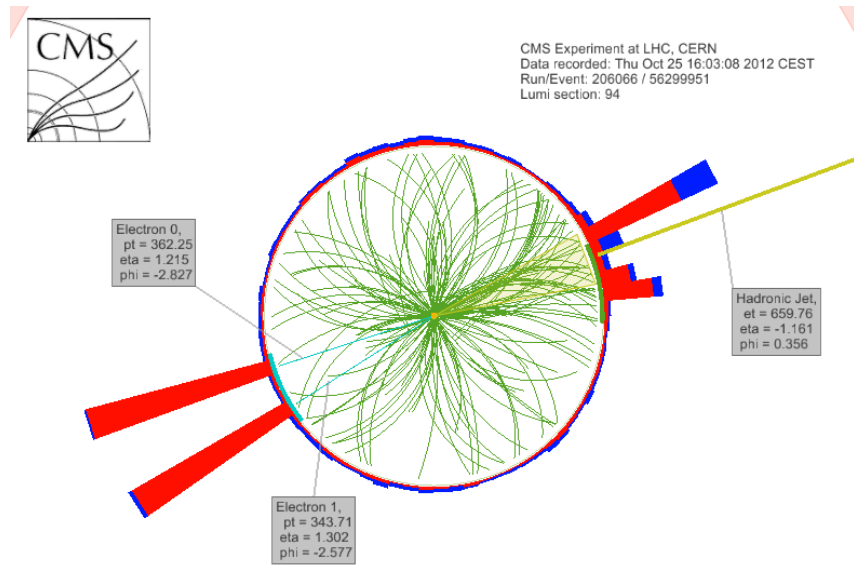


Figure 60: Dielectron + jet event with $m_{ZZ} \sim 2.5$ TeV, in $\rho - \phi$ view.

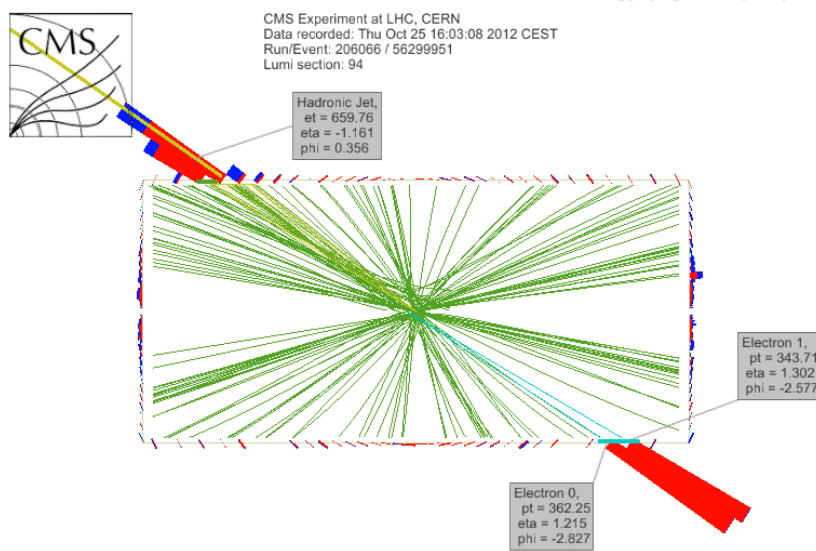


Figure 61: Dielectron + jet event with $m_{ZZ} \sim 2.5$ TeV, in $\rho - z$ view

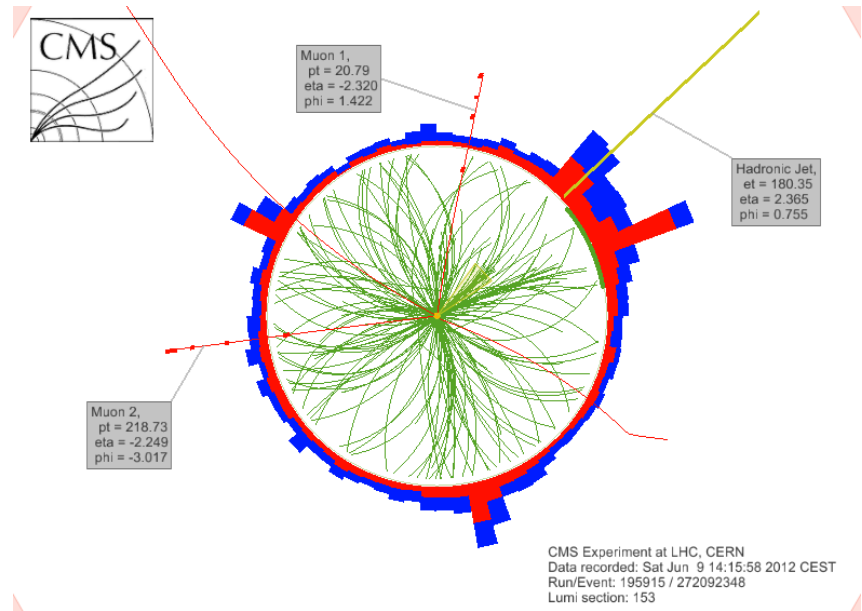


Figure 62: Dimuon + jet event with $m_{ZZ} \sim 2.5$ TeV, in $\rho - \phi$ view.

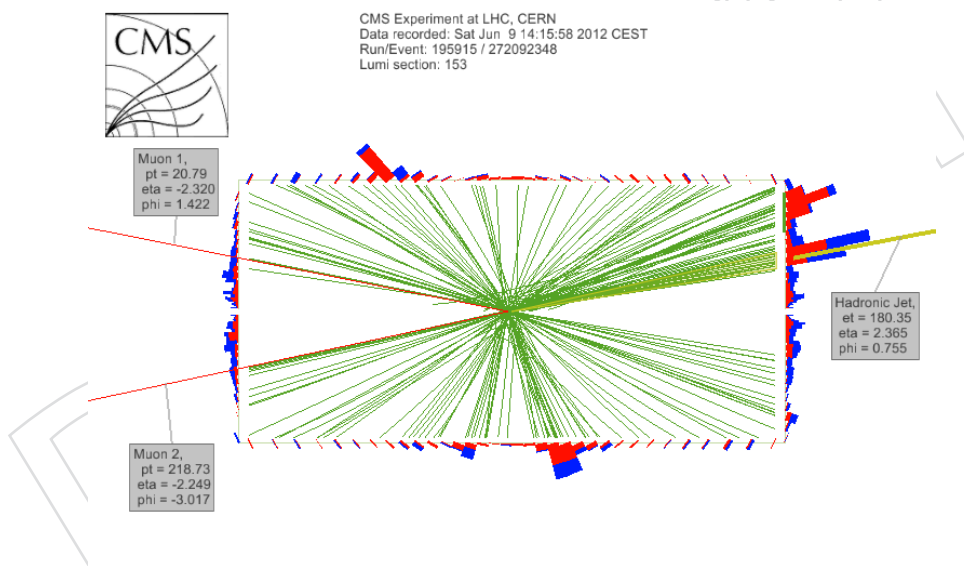


Figure 63: Dimuon + jet event with $m_{ZZ} \sim 2.5$ TeV, in $\rho - z$ view

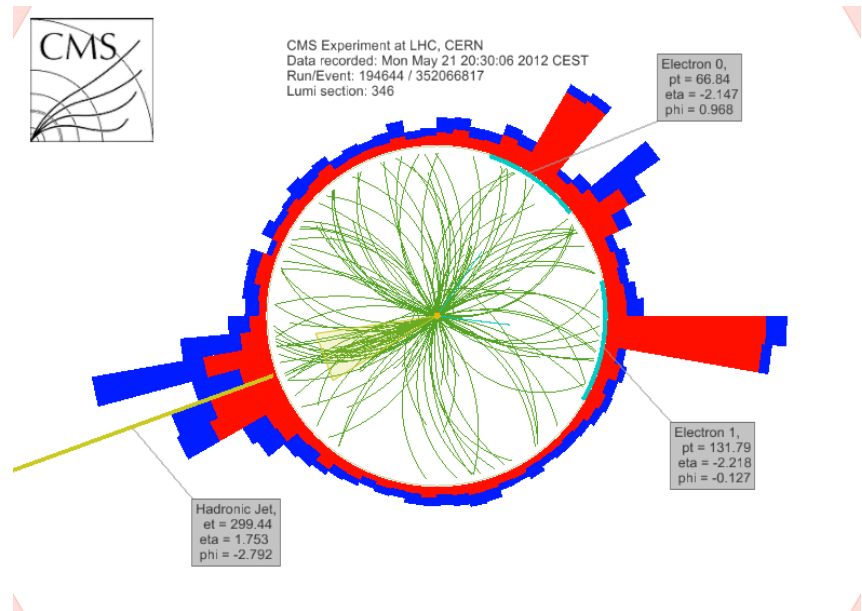


Figure 64: Dielectron + jet event with $m_{ZZ} \sim 1.7$ TeV, in $\rho - \phi$ view.

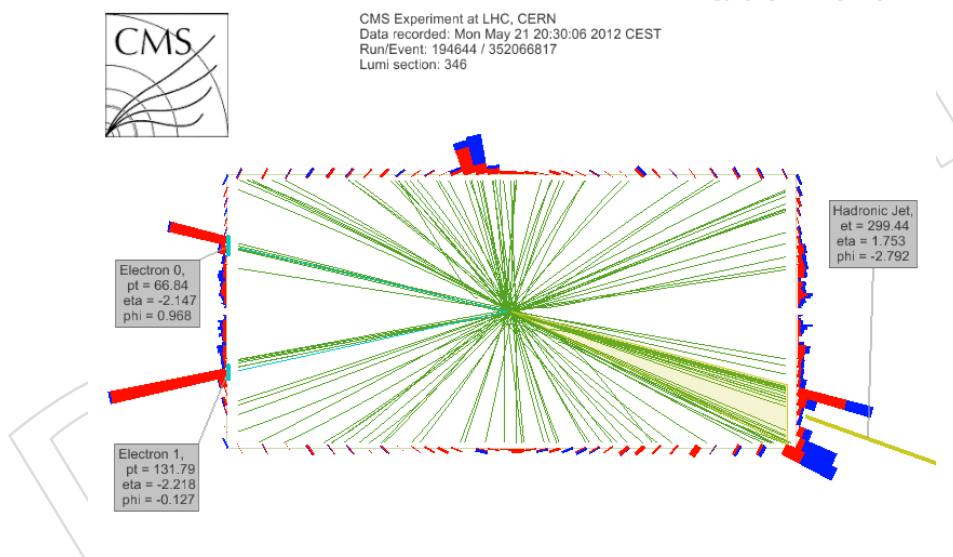


Figure 65: Dielectron + jet event with $m_{ZZ} \sim 1.7$ TeV, in $\rho - z$ view

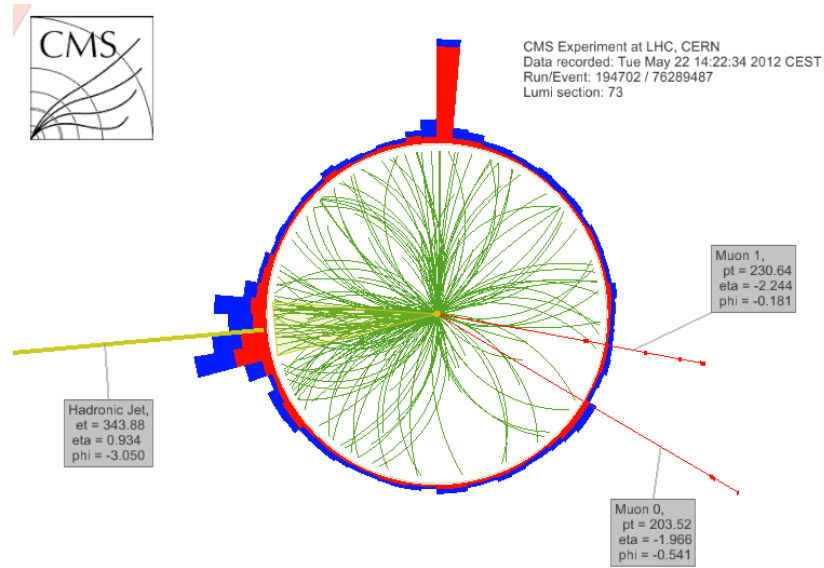


Figure 66: Dimuon + jet event with $m_{ZZ} \sim 1.8$ TeV, in $\rho - \phi$ view.

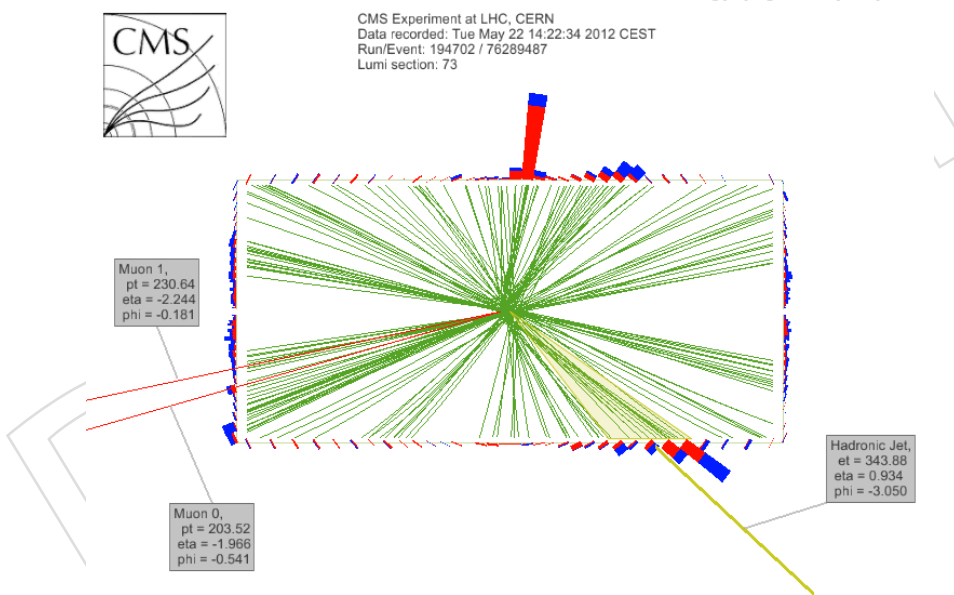


Figure 67: Dimuon + jet event with $m_{ZZ} \sim 1.8$ TeV, in $\rho - z$ view

1138 References

- [1] ALEPH, CDF, D0, DELPHI, L3, OPAL, SLD Collaborations, the LEP Electroweak Working Group, the Tevatron Electroweak Working Group, and the SLD Electroweak and Heavy Flavour Groups, "Precision electroweak measurements and constraints on the Standard Model", (2010).
arXiv:1012.2367.
- [2] ATLAS Collaboration, "Observation of a new particle in the search for the Standard Model Higgs boson with the ATLAS detector at the LHC", *Physics Letters B* **716** (2012), no. 1, 1, doi:10.1016/j.physletb.2012.08.020.
- [3] CMS Collaboration, "Observation of a new boson at a mass of 125 GeV with the CMS experiment at the {LHC}", *Physics Letters B* **716** (2012), no. 1, 30, doi:10.1016/j.physletb.2012.08.021.
- [4] G. D. N. Arkani-Hamed, S. Dimopoulos, "The hierarchy problem and new dimensions at a millimeter", *Phys. Lett.* **B429** (1998) 263–272, doi:doi:10.1016/S0370-2693(98)00466-3, arXiv:9803315.
- [5] S. D. e. I. Antoniadis, N. Arkani-Hamed, "New dimensions at a millimeter to a Fermi and superstrings at a TeV", *Phys. Lett.* **B436** (1998) 257–263, doi:doi:10.1016/S0370-2693(98)00860-0, arXiv:9804398.
- [6] L. Randall and R. Sundrum, "A large mass hierarchy from a small extra dimension", *Phys. Rev. Lett.* **83** (1999) 3370, doi:10.1103/PhysRevLett.83.3370, arXiv:hep-ph/9905221.
- [7] L. Randall and R. Sundrum, "An alternative to compactification", *Phys. Rev. Lett.* **83** (1999) 4690, doi:10.1103/PhysRevLett.83.4690, arXiv:hep-th/9906064.
- [8] CDF Collaboration, "Search for Randall-Sundrum gravitons in the diphoton channel at CDF", *Phys. Rev. D* **83** (2011) 011102, doi:10.1103/PhysRevD.83.011102, arXiv:1012.2795.
- [9] CDF Collaboration, "Search for New Dielectron Resonances and Randall-Sundrum Gravitons at the Collider Detector at Fermilab", *Phys. Rev. Lett.* **107** (2011) 051801, doi:10.1103/PhysRevLett.107.051801, arXiv:1103.4650v2.
- [10] D0 Collaboration, "Search for Randall-Sundrum Gravitons in the Dielectron and Diphoton Final States with 5.4 fb^{-1} of Data from $\bar{p}p$ Collisions at $\sqrt{s} = 1.96 \text{ TeV}$ ", *Phys. Rev. Lett.* **104** (2010) 241802, doi:10.1103/PhysRevLett.104.241802, arXiv:1004.1826.
- [11] CMS Collaboration, "Search for Signatures of Extra Dimensions in the Diphoton Mass Spectrum at the Large Hadron Collider", *Phys. Rev. Lett.* **108** (2012) 111801, doi:10.1103/PhysRevLett.108.111801, arXiv:1112.0688.
- [12] CMS Collaboration, "Search for narrow resonances in dilepton mass spectra in pp collisions at $\sqrt{s} = 7 \text{ TeV}$ ", *Phys. Lett. B* **714** (2012) 158, doi:10.1016/j.physletb.2012.06.051, arXiv:1206.1849.
- [13] CMS Collaboration, "Search for a narrow spin-2 resonance decaying to a pair of Z vector bosons in the semileptonic final state", *Phys.Lett.* **B718** (2013) 1208–1228, doi:10.1016/j.physletb.2012.11.063, arXiv:1209.3807.
- [14] ATLAS Collaboration, "Search for strong gravity signatures in same-sign dimuon final states using the ATLAS detector at the LHC", *Phys. Lett. B* **709** (2012) 322, doi:10.1016/j.physletb.2012.02.049, arXiv:1111.0080.
- [15] ATLAS Collaboration, "Search for Dilepton Resonances in pp Collisions at $\sqrt{s} = 7 \text{ TeV}$ with the ATLAS Detector", *Phys. Rev. Lett.* **107** (2011) 272002, doi:10.1103/PhysRevLett.107.272002, arXiv:1108.1582.
- [16] CMS Collaboration, "Search for a narrow, spin-2 resonance decaying to a pair of Z bosons in the final state", *Physics Letters B* **718** (2013), no. 4-5, 1208 – 1228, doi:10.1016/j.physletb.2012.11.063, arXiv:1209.3807. CMS-PAS-EXO-11-102.

- [1185] [17] CMS Collaboration, "Search for exotic resonances decaying into WZ/ZZ in pp collisions at $\sqrt{s} = 7$ TeV", *JHEP* (2012) doi:10.1007/JHEP02(2013)036, arXiv:1211.5779.
[1186] CMS-PAS-EXO-12-014 ; CMS-PAS-EXO-11-081; CMS-PAS-EXO-11-061.
- [1188] [18] CMS Collaboration, "Search for heavy resonances in the W/Z-tagged dijet mass spectrum in pp collisions at 7 TeV", *Phys. Lett. B* **723** (2013) 280,
[1189] doi:doi:10.1016/j.physletb.2013.05.040, arXiv:1212.1910.
- [1191] [19] K. Agashe et al., "Warped Gravitons at the LHC and Beyond", *Phys. Rev. D* **76** (2007) 036006,
[1192] doi:10.1103/PhysRevD.76.036006, arXiv:hep-ph/0701186.
- [1193] [20] A. L. Fitzpatrick et al., "Searching for the Kaluza-Klein Graviton in Bulk RS Models", *JHEP* **09**
[1194] (2007) 012, doi:10.1088/1126-6708/2007/09/013, arXiv:hep-ph/0701150.
- [1195] [21] O. Antipin, D. Atwood, and A. Soni, "Search for RS gravitons via $W_L W_L$ decays", *Phys. Lett. B*
[1196] **666** (2008) 155, doi:10.1016/j.physletb.2008.07.009, arXiv:0711.3175.
- [1197] [22] W.-Y. K. V. Barger, Y. Gao, "T-Anomaly Induced LHC Signals", *Phys. Lett. B* **655** (2007) 228,
[1198] doi:doi:10.1016/j.physletb.2007.08.090, arXiv:0707.3648.
- [1199] [23] J. E. Juknevich, D. Melnikov, and M. J. Strassler, "A Pure-Glue Hidden Valley. States and Decays",
[1200] *J. High Energy Phys.* **0907** (2009) 055, doi:doi:10.1088/1126-6708/2009/07/055,
[1201] arXiv:0903.0883.
- [1202] [24] Y. Gao et al., "Spin-Determination of Single-Produced Resonances at Hadron Colliders",
[1203] *Phys. Rev. D* **81** (2010) doi:10.1103/PhysRevD.81.075022, arXiv:1001.3396.
- [1204] [25] S. Bolognesi et al., "On the Spin and Parity of a Single-Produced Resonance at the LHC",
[1205] *Phys. Rev. D* **86** (2012) 095031, doi:10.1103/PhysRevD.86.095031, arXiv:1208.4018.
- [1206] [26] T. Sjöstrand, S. Mrennan and P. Z. Skands, "PYTHIA 6.4 Physics and Manual", *JHEP* **05** (2006)
[1207] 026, doi:10.1088/1126-6708/2006/05/026, arXiv:hep-ph/0603175.
- [1208] [27] A. A. Belyaev, N. Christensen, "CalcHEP 3.4 for collider physics within and beyond the Standard
[1209] Model", *Computer Physics Communications* **184** (2013) 1729–1769,
[1210] doi:10.1016/j.cpc.2013.01.014, arXiv:1207.6082.
- [1211] [28] CMS Collaboration, ""Trigger strategies for Higgs searches in 2011"", CMS Analysis Note
[1212] CMS-AN-2011/065, (2011).
- [1213] [29] CMS Collaboration, "Performance of CMS muon reconstruction in pp collision events at $\sqrt{s} = 7$ TeV", *JINST* **7** (2012) P10002, doi:10.1088/1748-0221/7/10/P10002,
[1214] arXiv:1206.4071.
- [1216] [30] CMS Collaboration, ""Electron reconstruction and identification at $\sqrt{s}=7$ TeV"", CMS Physics
[1217] Analysis Summary CMS-PAS-EGM-10-004, (2010).
- [1218] [31] CMS Collaboration, ""Modified isolation cuts for the selection of high pT electrons from the decay
[1219] of boosted Z bosons"", CMS Analysis Note CMS-AN-2012/168, (2012).
- [1220] [32] CMS Collaboration, ""Commissioning of the Particle-Flow Reconstruction in Minimum-Bias and
[1221] Jet Events from pp Collisions at 7 TeV"", CMS Physics Analysis Summary CMS-PAS-PFT-10-002,
[1222] (2010).
- [1223] [33] CMS Collaboration, ""Jet Energy Corrections determination at 7 TeV"", CMS Physics Analysis
[1224] Summary CMS-PAS-JME-10-010, (2010).
- [1225] [34] CMS Collaboration, "Search for anomalous $t\bar{t}$ production in the highly-boosted all-hadronic final
[1226] state", *JHEP* **09** (2012) 029, doi:10.1007/JHEP09(2012)029, arXiv:1204.2488.
[1227] CMS-PAS-EXO-11-006.
- [1228] [35] CMS Collaboration, ""Searches for new physics in the $WW \rightarrow l\nu j$ final state with hadronic W
[1229] bosons merged into a single jet"", CMS Analysis Note CMS-AN-2012/381, (2012).
- [1230] [36] CMS Collaboration, ""Identifying Hadronically Decaying W Bosons Merged into a Single Jet"",
[1231] CMS Physics Analysis Summary CMS-PAS-JME-13-006, (2013).

- [37] CMS Collaboration, ““Identifying Hadronically Decaying Vector Bosons Merged into a Single Jet””, CMS Analysis Note CMS-AN-2013/072, (2013).
- [38] CMS Collaboration, “Search for BSM $t\bar{t}$ production in the boosted all-hadronic final state using pp collisions at $\sqrt{s} = 8 \text{ TeV}$ ”, CMS Analysis Note CMS-AN-2012/179, (2013).
- [39] CMS Collaboration, “Studies of jet mass in dijet and $W/Z+\text{jet}$ events”, *JHEP* **05** (2013) 090, doi:10.1007/JHEP05(2013)090, arXiv:1303.4811.
- [40] CMS Collaboration, “Identifying Hadronically Decaying W Bosons Merged into a Single Jet”, CMS Physics Analysis Summary CMS-PAS-JME-13-006, (2013).
- [41] S. D. Ellis, C. K. Vermilion, and J. R. Walsh, “Recombination Algorithms and Jet Substructure: Pruning as a Tool for Heavy Particle Searches”, *Phys.Rev.* **D81** (2010) 094023, doi:10.1103/PhysRevD.81.094023, arXiv:0912.0033.
- [42] J. Thaler and K. Van Tilburg, “Identifying Boosted Objects with N-subjettiness”, *JHEP* **1103** (2011) 015, doi:10.1007/JHEP03(2011)015, arXiv:1011.2268.
- [43] J. Thaler and K. Van Tilburg, “Maximizing Boosted Top Identification by Minimizing N-subjettiness”, *JHEP* **1202** (2012) 093, doi:10.1007/JHEP02(2012)093, arXiv:1108.2701.
- [44] I. W. Stewart, F. J. Tackmann, and W. J. Waalewijn, “N-Jettiness: An Inclusive Event Shape to Veto Jets”, *Phys.Rev.Lett.* **105** (2010) 092002, doi:10.1103/PhysRevLett.105.092002, arXiv:1004.2489.
- [45] CMS Collaboration, “Search for a BSM resonance decaying to W vector bosons in the semileptonic final state”, CMS Analysis Note CMS-AN-2013/045, (2013).
- [46] CMS Collaboration, “Search for Exotic resonances decaying to WW in the semi-leptonic channel”, CMS Analysis Note CMS-AN-2013/139, (2013).
- [47] CMS Collaboration, “Search for a SM Higgs or BSM Boson $H \rightarrow ZZ^{(*)} \rightarrow (q\bar{q})(\ell^-\ell^+)$ ”, CMS Analysis Note CMS-AN-2011/388, (2011).
- [48] CMS Collaboration, “Search for a Higgs boson in the decay channel $H \rightarrow ZZ^{(*)}$ to $q\bar{q}$ l-l+ in pp collisions at $\sqrt{s} = 7 \text{ TeV}$ ”, *JHEP* **04** (2012) 036, doi:10.1007/JHEP04(2012)036, arXiv:1202.1416. CMS-PAS-HIG-11-027.
- [49] G. Punzi, “Sensitivity of searches for new signals and its optimization”, in *proceedings to PhyStat 2003 Conference, Stanford, Ca, USA, September 2003, PSN MODT002*. arXiv:physics/0308063v2.
- [50] CMS Collaboration, ““Search for heavy resonances in the W/Z -tagged dijet mass spectrum in pp collisions at 8 TeV””, CMS Physics Analysis Summary CMS-PAS-EXO-12-024, (2013).
- [51] T. Han, J. D. Lykken, and R.-J. Zhang, “On Kaluza-Klein states from large extra dimensions”, *Phys.Rev.* **D59** (1999) 105006, doi:10.1103/PhysRevD.59.105006, arXiv:hep-ph/9811350.
- [52] CMS Collaboration, ““Search for WW resonances in $\ell + \nu + \text{jet}$ final state””, CMS Physics Analysis Summary CMS-PAS-EXO-12-021, (2013).
- [53] CMS Collaboration, ““Measurement of the ZZ production cross section in $ZZ \rightarrow 2\ell 2\ell'$ decay channel at $\sqrt{s} = 8 \text{ TeV}$ ””, CMS Physics Analysis Summary CMS-PAS-SMP-12-014, (2013). “AN-2012/141”.
- [54] CMS Collaboration, ““Properties of the Higgs-like boson in the decay $H \rightarrow 4\ell$ in pp collisions at $\sqrt{s} = 7$ and 8 TeV””, CMS Physics Analysis Summary CMS-PAS-HIG-13-002, (2013). “AN-2013/003”.
- [55] CMS Collaboration, “Search for new physics in the single lepton + MET final states with the full 2012 dataset at $\sqrt{s} = 8 \text{ TeV}$ ”, CMS Analysis Note CMS-AN-2012/423, (2012).
- [56] M. P. O. Group, “Muon Reference Efficiencies”, (2013).

- 1279 [57] D. B. M.R. Whalley and R. Group, "The Les Houches accord PDFs (LHAPDF) and Lhaglue",
1280 (2005). arXiv:0508110.
- 1281 [58] M. Botje et al., "The PDF4LHC Working Group Interim Recommendations", (2011).
1282 arXiv:1101.0538.
- 1283 [59] CMS Collaboration, ""Combined results of searches for the standard model Higgs boson in pp
1284 collisions at $\sqrt{s} = 7 \text{ TeV}"$, *Phys. Lett. B* (2012), no. 710, arXiv:1202.1488.
- 1285 [60] G. Cowan, K. Cranmer, E. Gross, O. Vitells, "Asymptotic formulae for likelihood based tests of
1286 new physics", *Eur. Phys. J. C* **71** (2011) 1554, arXiv:physics/1007.1727v2.
- 1287 [61] A. L. Read, "Presentation of search results: The CL(s) technique", *J. Phys. G* **28** (2002) 2693–2704,
1288 doi:10.1088/0954-3899/28/10/313.
- 1289 [62] A. L. Read, "Modified frequentist analysis of search results (the CLs method)", technical report,
1290 (2000).
- 1291 [63] "Tag And Probe Tool".
1292 <http://cmssw.cvs.cern.ch/cgi-bin/cmssw.cgi/CMSSW/PhysicsTools/TagAndProbe/>.
- 1293 [64] "Muon reconstruction, identification and isolation efficiencies".
1294 <https://twiki.cern.ch/twiki/bin/view/CMS/MuonReferenceEffs>.
- 1295 [65] "Systematic uncertainties".
1296 <https://twiki.cern.ch/twiki/bin/view/CMS/MuonTagAndProbe>.
- 1297 [66] H. Brun, "Follow-Up on the di-muon trigger measurement with the reference trigger method",
1298 (2013).
- 1299 [67] CMS Collaboration, ""Search for Narrow Resonances using the Dijet Mass Spectrum with 19.6fb⁻¹
1300 of pp Collisions at $\text{sqrt}s=8 \text{ TeV}"$, CMS Physics Analysis Summary CMS-PAS-EXO-12-059, (2013).